UNIVERSITÀ DEGLI STUDI DI MILANO

DEPARTMENT OF PHYSICS

PH.D. SCHOOL IN
PHYSICS, ASTROPHYSICS AND APPLIED PHYSICS
CYCLE XXXVII

Time-domain investigation of acoustically and thermally driven magnons

Disciplinary Scientific Sector PHYS/03A

Ph.D. Thesis of:
Marta Brioschi

Director of the School: Prof. A. Mennella
Supervisor of the Thesis: Prof. G. Rossi
Co-supervisor of the Thesis: Dr. R. Cucini

A.Y. 2023-2024

Commission of the final examination:

External Referees:
Dr. C. Vozzi & Prof. C. Giannetti

External Members:
Dr. C. Vozzi & Prof. C. Giannetti

Internal Member:
Prof. G. Rossi

Final examination:

16th December 2024
Dipartimento di Fisica, Università degli Studi di Milano, Italy

The more I learn, the more I realize
how much I don't know

A. Einstein

Cover illustration:

"*Magnetic mountain*" by K. Seligmann

Internal illustrations:

M. Brioschi

Design:

A.D. Copia, Copiae

MUR subject:

PHYS/03A

Contents

Abstract vii

Introduction ix

Part I: Scientific and technical background 1

1 Magnetic excitations in solids 3
- 1.1 The Landau-Lifshitz-Gilbert Equation 4
- 1.2 Ferromagnetic resonance 6
- 1.3 Spin waves 7
- 1.4 Magnetoelastic coupling and elastically-driven excitations 8

2 Time-resolved all-optical methods 15
- 2.1 Magneto-optical effects 15
- 2.2 Transient Grating Spectroscopy 18

Part II: A TG approach to acoustics, magnetoacoustics and magnonics 27

3 TG Spectroscopy@ the NFFA-SPRINT lab 29
- 3.1 Operational mode 1 : TG spectroscopy with pulsed probe 30
- 3.2 Operational mode 2: TG spectroscopy with CW probe 34
- 3.3 Operational mode 3: TG pumping with tr-polarimetry 36
- 3.4 On the sample environment 37

4 Acoustics and magnetoacustics 39
- 4.1 Sample details 40
- 4.2 Experimental results: acoustics 41
- 4.3 Experimental results: magnetoacoustics 46
- 4.4 Conclusions 55

5 Magnonics **57**
5.1 Excitation and probing mechanism 58
5.2 Sample details 62
5.3 Experimental results 68
5.4 Conclusions 78

Part III: Magnetization dynamics in Fe_5GeTe_2 **81**

6 Magnetization dynamics in Fe_5GeTe_2 **83**
6.1 Sample details 84
6.2 Experimental results 86
6.3 Conclusions 95

Conclusions **97**

Appendices **99**

A Supplementary material on the Ni samples **101**

B Supplementary material on the $Co_{78}Gd_{22}$ sample **109**

C Supplementary material on the Fe_5GeTe_2 sample **113**

List of Abbreviations **128**

List of Publications **134**

Acknowledgments **138**

Abstract

This thesis is the result of the research programme carried out as Ph.D. student of the School in Physics, Astrophysics and Applied Physics at Università degli Studi di Milano, that was performed, since October 2021 at the Istituto Officina dei Materiali of Consiglio Nazionale delle Ricerche (CNR-IOM) within the Nanoscale Foundries and Fine Analysis (NFFA) facility.

My experimental activity led to the implementation of a novel experimental setup within the NFFA-SPRINT laboratory[1] in the premises of the FERMI@Elettra facility (Elettra - Sincrotrone Trieste), and to the establishment of new methodologies for the study of the dynamical properties of matter, including thin films and surfaces.

First, I developed and commissioned an experimental setup for optical Transient Grating (TG) spectroscopy; subsequently adding to it new time-resolved detection schemes enabling to perform time-resolved reflectivity and polarimetry, as these were needed to address the dynamics of magnetization in solids.

The setup exploits the 300-fs laser sources of SPRINT laboratory and the optical parametric amplifiers (OPAs) at a repetition rate of 100kHz. To address my Ph.D. programme, I used this setup to induce out-of-equilibrium transients in bulk or thin-film samples by shining on them the sub-picosecond laser pulses, then retrieving signals representative of acoustical and thermal magnons in metallic thin films.

In a first experiment, acoustically driven spin wave resonance in polycrystalline Ni thin films was investigated using the TG technique. The focus was on examining how the acoustic waves generated in the substrate influence and drive the magnetization dynamics of the Ni thin films via magnetoelastic coupling. Resonances in the magnetization dynamics were observed when the magnonic band dispersion was tuned to cross the phononic band at a fixed wavevector. I deepened the understanding of the results by quantitatively comparing with standard ferromagnetic resonance measurements carried out in collaboration with an external group. Here I present the TG-based technique highlighting its potential and limitations. In a second experiment, the TG approach has been exploited to drive coherent magnons at a selected wavevector non-relying on the magnetoelastic coupling but rather on the spatially modulated temperature profile generated by the TG excitation mechanism itself. The approach was successfully tested on ferrimagnetic $Co_{78}Gd_{22}$ alloy. The measured signal depends on laser fluence, suggesting the potential of heterogeneous excitation from the TG mechanism to induce locally different magnetic behaviours. This measurement campaign was conducted as part of an

[1] https://www.trieste.nffa.eu

international collaboration aimed at extending this methodology to the Extreme Ultra Violet (EUV) range, where magnons with wavelengths as short as a few tens of nanometers can be selectively triggered. Finally, I studied systematically the laser-driven ferromagnetic resonance in Fe_5GeTe_2 employing time-resolved Magneto-Optical Kerr Effect (tr-MOKE), implemented in the same setup, as a function of both the external magnetic field and the temperature. Overall my results brought evidences on the dynamical magnetic properties of the systems that I studied and also, importantly, demonstrated the possibility of filling the gap in the study of coherent magnetization dynamics, opening novel research opportunities in the time domain.

Introduction

The concept of spin waves, also known as magnons, was introduced in 1930 by the Dutch physicist Felix Bloch; since then, significant progress has been made in understanding spin waves and in exploring their potential technological applications. Spin waves remain nevertheless an active field of research, with many fundamental questions still unanswered. Spin waves are excitations of the magnetization that can propagate in the form of waves; their properties can vary depending on the hosting material and are encoded in the spin wave dispersion. Low-energy magnetic excitations do not propagate undisturbed in a magnetic solid-state sample but interact - in a simplified picture - with electrons and lattice degrees of freedom across a wide range of timescales, from femtoseconds to several nanoseconds. The development of reliable ultrashort laser pulses marked a significant breakthrough in time-resolved magnetization dynamics studies, pushing the time resolution into the sub-picosecond range. In recent decades, this has contributed to understanding how out-of-equilibrium states relax back to equilibrium, how the injected energy is distributed among the various degrees of freedom, and the conditions under which they may couple.

In addition to these fundamental open questions, there is increasing interest in addressing the potential of spin wave excitations for novel energy-efficient magnetic devices. Significant research efforts have focused on finding materials where spin waves can propagate over long distances, be easily manipulated, and be efficiently generated. Recently, it has been demonstrated that spin waves are generated at relatively low energy costs by exploiting the magnetoelastic coupling, opening up a whole new range of possibilities. Laser-based techniques that allow for the simultaneous excitation of different collective excitations - such as phonons and magnons - at a fixed wavevector are highly valuable for studying the coherent transfer of energy and momentum between these excitations and for identifying the critical experimental and sample parameters that influence this process. Furthermore, achieving selectivity over the wavevector of magnons, even without relying on the magnetoelastic coupling, is per-se interesting for example to reconstruct the spin wave dispersion, whose features can help to get insight into key magnetic parameters such as magnetic anisotropy, saturation magnetization, and exchange stiffness. These aspects investigated in a time-resolved fashion provide additional valuable information about the evolution of spin waves over time; for example, the damping, phase, and amplitude changes as a function of wavevector and other external parameters to achieve a consistent picture of the light-driven magnetization dynamics.

This is the general framework and motivation in which this thesis is developed. In particular, some of the aspects mentioned above are addressed using time-resolved MOKE and Transient Grating Spectroscopy, a time-resolved all-optical technique that has recently gained popularity in the magnetism community, partly due to novel design of experimental setups and magneto-sensitive probes spanning from the optical to the X-ray ranges.

Thesis Overview

The present thesis reports original experimental results on coherent magnetization dynamics in metallic thin films. My approach has been to exploit chiefly all-optical pump-probe spectroscopy and develop the instrumentation and methodology to this scope.
Part I aims at providing the technical and scientific background needed to understand the performed experiments.

Chapter 1 provides a brief overview of magnetic excitations in solids. After a brief introduction on the magnetic excitations and Larmor precession, we introduce spin waves, magnetoelastic coupling, and elastically driven excitations with a focus on the case of interest in the framework of this thesis.

In Chapter 2 introduces the experimental time-resolved techniques adopted for my research activity, in particular time-resolved polarimetry and Transient Grating Spectroscopy.

Part II is dedicated to introducing the TG technique as a method to study acoustics, magnetoacoustics, and magnonics.

Chapter 3 describes the NFFA-SPRINT TG experimental setup. It includes an overview of the operational modes as well as technical details of the setup.

Chapter 4 presents experimental results on polycrystalline Ni thin films, demonstrating how the operational modes of the experimental setup can address both acoustic and magnetoacoustic dynamics in magnetostrictive samples.

Chapter 5 demonstrates how the TG approach can drive coherent magnons at a fixed wavevector by directly exploiting the spatial temperature profile created by TG excitation, rather than relying on magnetoelastic coupling. Results on $Co_{78}Gd_{22}$ alloy thin films highlight the potential of nonhomogeneous excitation. Additionally, results from an international collaboration, including Fe/Gd multilayers measured at TIMER@FERMI, validate TG spectroscopy as an effective tool for high-wavevector magnonics.

Part III (Ch. 6) presents original results from a systematic investigation of laser-driven ferromagnetic resonance in Fe_5GeTe_2 using time-resolved MOKE, exploring its behavior as a function of temperature and external magnetic field.

Part I

Scientific and technical background

CHAPTER 1

Magnetic excitations in solids

Magnetic excitations in solids occur over a wide range of spatial and temporal scales, determined by the underlying magnetic interactions. Fig. 1.1 illustrates the typical spatial and temporal scales of the main interactions and excitations. This broad range encompasses various magnetic effects, from ultrafast angular momentum exchange to GHz-frequency precession in ferromagnetic materials influenced by magnetic fields and spin torques. Rapid processes, happening within hundreds of fs, are driven by exchange interactions, spin-orbit coupling (SOC), and band structure effects. At these ultrafast timescales, the fundamental nature of magnetism becomes apparent, with different degrees of freedom - charge, spin, orbital, and phonon - showing specific temporal behaviors while remaining intricately coupled. Describing these ultrafast dynamics requires the use of quantum mechanics.

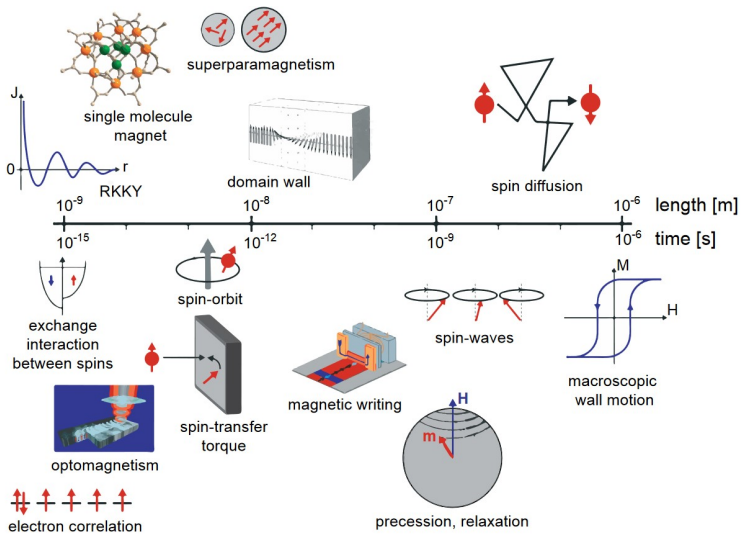

Figure 1.1: Spatial and temporal scales of magnetic interactions and phenomena. Adapted from [1].

1.1 The Landau-Lifshitz-Gilbert Equation

For timescales longer than a few ps, the collective motion of magnetic moments can be described using classical or semiclassical models. In this regime, the dynamics are influenced by effective magnetic fields, while magnetic moments over regions spanning a few nm exhibit collective behavior [2, 3]. This collective behavior allows the replacement of individual atomic spins with an average vector field, known as magnetization. The magnetization is represented as an axial vector field that varies smoothly in both spatial and temporal domains; it can be written as $\mathbf{M}(\mathbf{r},t) = \mathrm{M_s} \cdot \mathbf{m}(\mathbf{r},t)$, where M_s is the saturation magnetization, and $\mathbf{m}(\mathbf{r},t)$ is the unit magnetization vector. The magnitude of the magnetization M_s is finite only below the Curie temperature ($\mathrm{T_c}$). In this regime, the magnetization dynamics is well described by the Landau-Lifshitz-Gilbert (LLG) equation [2, 4]:

$$\frac{\mathrm{d}\mathbf{M}}{\mathrm{d}t} = -\gamma\left(\mathbf{M}\times\mathbf{H}_{\text{eff}}\right) + \frac{\alpha}{M_s}\mathbf{M}\times\frac{\mathrm{d}\mathbf{M}}{\mathrm{d}t} \tag{1.1}$$

where γ is the gyromagnetic ratio and $\alpha > 0$ the Gilbert damping parameter.
The first term is the torque exerted on the magnetic moment. The effective field $\mathbf{H}_{\text{eff}}$ is a time-dependent vector that takes into account interactions contributing to the energy of the magnetic system trough

$$\mathbf{H}_{\text{eff}}(\mathbf{r},t) = -\frac{1}{\mu_0}\frac{\delta F(\mathbf{r},t)}{\delta \mathbf{M}(\mathbf{r},t)} \tag{1.2}$$

where μ_0 the vacuum magnetic permeability and $F(\mathbf{r},t)$ is the total magnetic energy.

Neglecting the dependency on $\mathbf{r}$ and t for simplicity, the main contributions to F are given by [5]:

- The exchange energy describes the interaction between spins in a magnetically ordered material and is responsible for the formation of a spontaneous magnetic order below T_c in 3d metals. Its contribution to F can be written as:

$$F_{\text{exc}} = \frac{A}{M_s}\left[(\nabla M_x)^2 + (\nabla M_y)^2 + (\nabla M_z)^2\right] \tag{1.3}$$

  where M_s is the saturation magnetization, A the exchange stiffness and M_x, M_y, M_z the magnetization components.

- The Zeeman energy : This is the usual energy term arising from magnetostatic interaction with an external magnetic field. It is minimized when $\mathbf{M}$ is alinged with the external field $\mathbf{H_{ext}}$.

$$F_Z = -\mu_0 \mathbf{M}\cdot\mathbf{H}_{\text{ext}} \tag{1.4}$$

- Magneto-Crystalline Anisotropy: it establishes a preferred axis for $\mathbf{M}$ based on the crystal structure of the material. Fundamentally, it arises from the SOC, which imparts a preferred direction to the magnetic moments depending on the anisotropy of the orbitals. Typically, the free energy density is expressed as

$$F_{\text{MCA}} = -\frac{K_u}{M_s}(\mathbf{M}\cdot\hat{\mathbf{u}})^2 \tag{1.5}$$

  for a magnetization Easy Axis (EA) identified by the unit vector $\hat{\mathbf{u}}$; K_u is the uni-

axial MCA constant.

- Shape anisotropy: depending on the geometrical size and shape of the magnetic samples, it can be relevant to introduce demagnetizing fields $\mathbf{H}_\mathrm{d}$ [6] describing the preferred direction of $\mathbf{M}$. The contribution to the free energy can be written as

$$F_s = -\mu_0 \mathbf{M} \cdot \mathbf{H}_\mathrm{d} \tag{1.6}$$

- Dipolar interactions: if $\mathbf{M}$ is not spatially uniform ($\nabla \cdot \mathbf{M} \neq 0$), long-range dipole-dipole interactions become significant. These interactions decrease in strength at a rate proportional to the cube of the distance between the dipoles.

- Magnetoelastic coupling: the interaction between the elastic and magnetic degrees of freedom gives a free energy contribution that can be expressed as [7]

$$F_\mathrm{MEC} = \frac{B_1}{M_s^2} \sum_i M_{ii}^2 \epsilon_{ii} + \frac{B_2}{M_s^2} \sum_i \sum_{j \neq i} M_i M_j \epsilon_{ij} \tag{1.7}$$

  where B_1 and B_2 are the magnetoelastic constants, M_i is the i-th magnetization vector component, and ϵ_{ij} are the (time dependent) strain tensor components.

This is just a partial list of the primary interactions likely to be present in the samples discussed in the following chapters. Depending on the type and complexity of the sample, other interactions may also need to be considered to describe the magnetization dynamics accurately.

The second term of Eq. 1.1 is the damping torque and describes the magnetization damping. The phenomenological Gilbert damping α includes all the complex details of the irreversible processes that do not conserve the angular momentum - such as eddy currents, electron, magnon, and phonon scatterings, spin currents, thermal fluctuations, strains, and crystal defects - that causes the magnetization eventually to align along $\mathbf{H}_\mathrm{eff}$.

Strictly speaking, Eq. 1.1 applies to a single magnetic moment or to a group of moments that move together coherently, known as the macrospin limit. However, this equation can also be used for non-uniform magnetic systems, as long as the magnetic volume is divided into sufficiently small regions (domains) where the dynamics remain coherent. Moreover, Eq. 1.1 fails in describing the magnetization dynamics on the typical timescales of exchange interactions. However, on the ps timescale, each spin site has enough time to sense changes in its neighboring spins and adjust its direction accordingly. In this regime, the dynamics are effectively captured by the macrospin approximation.

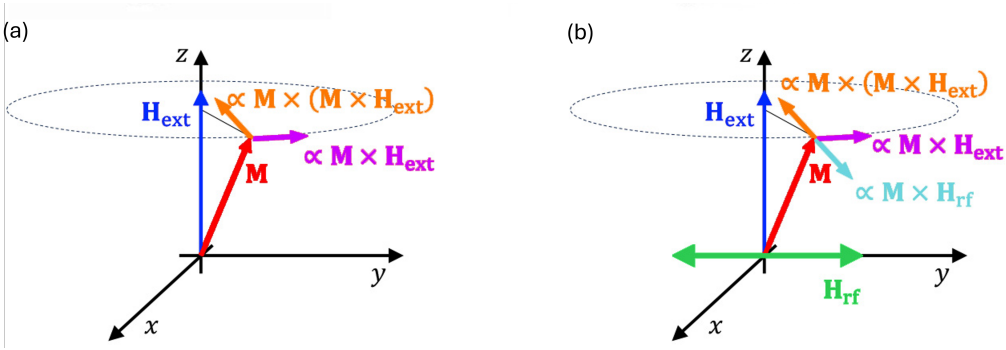

Figure 1.2: (a) The magnetization vector $\mathbf{M}$ (red arrow) rotates around the external magnetic field $\mathbf{H}_{\text{ext}}$ (blue arrow) due to the influence of the Larmor torque ($\propto \mathbf{M} \times \mathbf{H}_{\text{ext}}$, fuchsia arrow). As a result of dissipation, a frictional torque [$\propto \mathbf{M} \times (\mathbf{M} \times \mathbf{H}_{\text{ext}})$, orange arrow] causes $\mathbf{M}$ to follow a spiraling path until it eventually aligns with the external field. (b) The dynamics of magnetization change when a rf oscillating term $\mathbf{H}_{\text{rf}}$ (green arrow) is added perpendicular to the static field. The resulting additional torque ($\propto \mathbf{M} \times \mathbf{H}_{\text{rf}}$, light blue arrow) counteracts the frictional torque. After an initial adjustment period, $\mathbf{M}$ precesses along a stable orbit.

1.2 Ferromagnetic resonance

In the case of a static external field H_{ext}, the LLG equation describes well the damped precession of the magnetization around the H_{ext} that causes the magnetization collapse onto H_{ext} [6]. If the external field is strong enough so that the Zeeman interaction dominates among the other energy contributions to the effective field, the frequency of the precession - the so-called Larmor frequency - can be written as $\omega_L = \gamma H_{\text{ext}}$ [8–10]. Typically, for ferromagnetic systems the Larmor precession falls in the radio-frequency (rf) range.

Ferromagnetic resonance (FMR) can be observed when the external static field $\mathbf{H}_{\text{ext}}$ is superimposed to a time-dependent rf field $\mathbf{H}_{\text{rf}}$ oscillating at ω_L and orthogonally to $\mathbf{H}_{\text{ext}}$. The reason why can be easily understood in terms of torques exerted on the magnetization, as depicted in Fig 1.2: if the direction and frequency of $\mathbf{H}_{\text{rf}}$ meet the requirements above, the torque exerted by $\mathbf{H}_{\text{rf}}$ on $\mathbf{M}$ balances the damping torque - i.e. second term of the LLG equation - enabling the magnetization to precess along a stable orbit characterized by a fixed precession angle.

FMR is a powerful technique that allows to measure many important properties of magnetic media, from bulk to nanoscale magnetic thin films. For example, it has been used to measure the Curie temperature [11], total magnetic moment [12] and the magnetization damping mechanism [13]. Furthermore, FMR can also be used to investigate complex phenomena such as spin pumping, the spin hall effect, and the inverse spin hall effect [14–16]. Typically, FMR studies involve the use of a microwave cavity [9]; however, more recently, it has been demonstrated that FMR can also be triggered by fs laser pulses [17] or by rf fields generated by acoustic waves [18–20]. These excitation mechanisms will be discussed more in detail throughout this thesis.

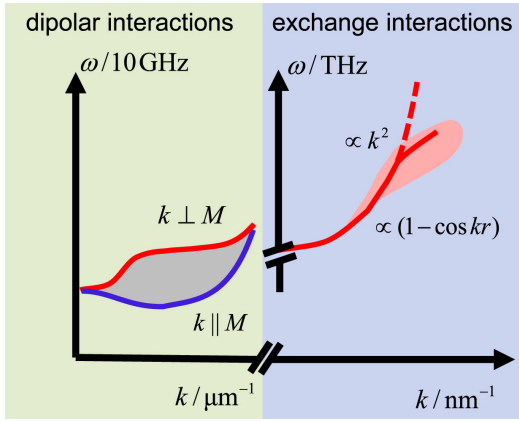

Figure 1.3: Typical spin wave dispersion diagram. In the micrometer wavelength range (left), dipolar interactions are predominant. The Damon–Eshbach (in red) and Backward Volume (in blue) mode dispersions are schematically depicted. Additional modes at intermediate orientation of **k** with respect to **H** are confined to the gray shaded area. In the nanometer wavelength range (right), the dispersion exhibits a cosine-like behavior. In this region, the exchange interaction dominates and can be approximated by a parabola at low energies. This intersects a broad region of high-energy SW excitation, where SWs experience significant damping (red shaded area). Adapted from [21].

1.3 Spin waves

Magnons, are the quanta of magnetic excitations, analogous to phonons being the quanta of lattice excitation. The single quantum of a spin wave (SW) is a magnon with energy $\varepsilon = \hbar\omega(k, \mathbf{H})$, where $\hbar$ is the reduced Plank constant and $\omega(k, \mathbf{H})$ is the SW dispersion, which can be derived by solving the LLG equation [21]. The spin-spin interaction mediating the SW determines its frequency (energy), wavelength, and the $\omega(k, \mathbf{H})$ functional relation. As schematically depicted in Fig. 1.3, SWs are typically mediated by two main spin-spin interactions:

- The magnetic dipole-dipole (dd) interaction mediates SWs with frequency in the GHz range whose wavelength falls in the μm range. Since the dipole interaction is intrinsically anisotropic, the frequency of dd-mediated SWs depends on the orientation of its wavevector to the orientation of the static magnetization. Note that the FMR can be considered as a dd-mediated SW of infinite wavelength - and so with $k = 0$ - since all spins precess in phase around the equilibrium magnetization axis. The modes whose frequency lies above the one of the uniform precession generally tend to localize at the sample - e.g. a thin film - surface and have a wave vector pointing perpendicular to the magnetization, namely $\mathbf{k}||\mathbf{M} \perp \mathbf{H}$; these are the so-called Damon–Eshbach (DE) modes. Conversely, the backward volume waves (BVW) are excited when $\mathbf{k}||\mathbf{M}||\mathbf{H}$, and they are characterized at small k by frequency lower than the FMR one (at $k = 0$), which leads to group and phase velocities of opposite sign. A schematic representation of the DE and BVW modes dispersion is depicted in Fig. 1.4. For intermediate configurations, there is a manifold of SWs corresponding to the continuous change of angle from parallel to perpendicular, represented as a gray-shaded region in Fig. 1.3. As the

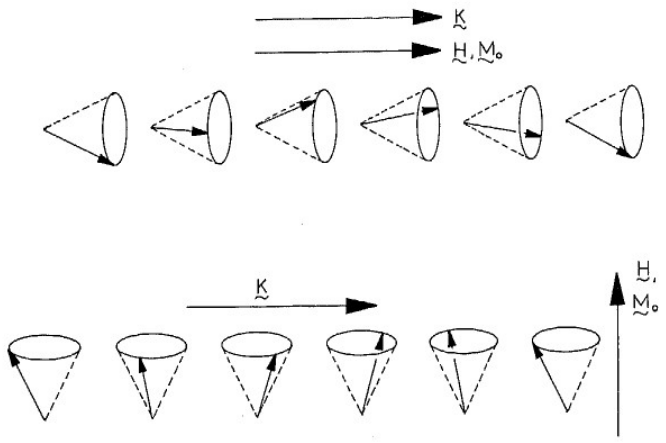

Figure 1.4: Schematic representation of the Damon–Eshbach (top) and Backward Volume Waves (bottom). From [22].

wavelength approaches the sub-micron range, the energy difference between DE and BVW modes decreases progressively until they eventually degenerate. At this point, the exchange interaction can no longer be considered negligible. In this range of wavevectors, the SWs are referred to as dipole-exchange SWs. The detailed description of this kind of modes can be found elsewhere [22].

- The exchange interaction mediates SWs with typical wavelengths of < 100 nm and frequency in the THz range. The dd-contribution to the energy of the wave can be neglected, meaning that the dispersion for exchange-mediated SWs does not depends on the orientation of $\mathbf{M}$, but rather on the next neighbor distance and the strength of the exchange interaction. The spin dispersion for a chain of precessing spins coupled to the next neighbors via the exchange interaction is derived in many physics textbooks (e.g. [23]), and results in a trend $\propto (1 - cos(kr))$. For small k, the dispersion can be approximated to a quadratic form, meaning that the energy increases quadratically $\propto k^2$ similar to the "free electron" behavior. In this region the SWs are heavily damped due to various scattering processes [21].

To conclude, it is worth mentioning that the overall effect of the applied magnetic field on the SW dispersion $\varepsilon = \hbar\omega(k, \mathbf{H})$ is to shift the SW manifold to higher frequencies, regardless of the type of interaction involved [22].

In this thesis, we will present results on both dipolar and exchange SWs, demonstrating how the TG technique can excite SWs at specific wavelengths - from the few-μm to the sub-100-nm range - exploiting different excitation mechanisms.

1.4 Magnetoelastic coupling and elastically-driven excitations

Magnetic excitations can be pumped by acoustic waves in materials exhibiting magnetoelastic coupling (MEC). This type of coupling originates from the anisotropy of the atomic structure in a material, which influences the electronic energy levels, and from the SOC, which facilitates interaction between the magnetic and lattice degrees of freedom. In this section, starting from the definition of magnetostriction, we will go through

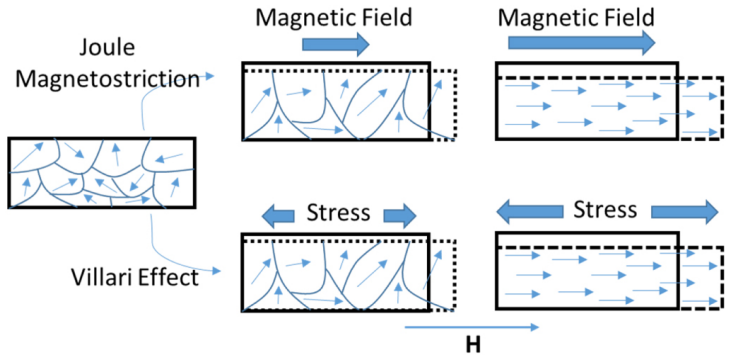

Figure 1.5: Joule magnetostriction refers to the strain generated when magnetic domains in a material reorient themselves in response to an applied magnetic field. Conversely, the Villari effect describes the phenomenon where the magnetization of a material changes when it is subjected to mechanical stress. From [24].

the main aspects of magnetoelastic coupling, focussing on how acoustic waves can drive magnetization dynamics.

Ferromagnetic materials change dimensions upon the application of a strong magnetic field, a phenomenon known as Joule Magnetostriction [25]; in the same way, via inverse magnetostriction - the so-called Villari effect - the magnetic state of a ferromagnetic can be influenced by strain. These two phenomena are depicted in Fig. 1.5. Magnetostriction is quantified by the saturation magnetostriction strain coefficient, which for isotropic materials is defined as $\lambda_s = \Delta l/l$, where l is the original length of the material before magnetization and Δl the length variation in the **M** direction when the material is magnetically saturated; therefore, λ_s quantifies the strain arising when the saturation field is applied and is an indicator of the strength of MEC. It is worth pointing out that λ_s depends on the crystallographic orientation [26]: in the case of a cubic lattice, $\lambda_{[100]}$ and $\lambda_{[111]}$ exhaustively describe the magnetostriction; however, in the case of a polycrystalline thin film with cubic lattice a single parameter $\lambda_s = 2/5 \cdot \lambda_{[100]} + 3/5 \cdot \lambda_{[111]}$ is enough. Typically, the λ parameters are of the order of 10^{-6}, but in certain materials can reach 10^{-3}, for example in Terfenol-D (an alloy of Tb, Dy and Fe) [27]. Among the 3d transition metals, Ni has one of the highest magnetostriction coefficients, with $\lambda_s = -38 \cdot 10^{-6}$ for a polycrystalline thin film [28]; for reference, Fe has $\lambda_s = -7 \cdot 10^{-6}$ [3].

As already mentioned in Sec. 1.1 MEC contributes to the magnetic energy landscape with

$$F_{\text{MEC}} = \frac{B_1}{M_s^2} \sum_i M_{ii}^2 \epsilon_{ii} + \frac{B_2}{M_s^2} \sum_i \sum_{j \neq i} M_i M_j \epsilon_{ij} \tag{1.8}$$

where B_i are the magnetoelastic coefficients and ϵ_{ij} the strain tensor components. Experimentally, the coefficients B_i are measured through related parameters. For example for a cubic lattice:

$$B_1 = \frac{3}{2} \lambda_{[100]} (c_{12} - c_{11}),$$
$$B_2 = -3 \lambda_{[111]} c_{44},$$

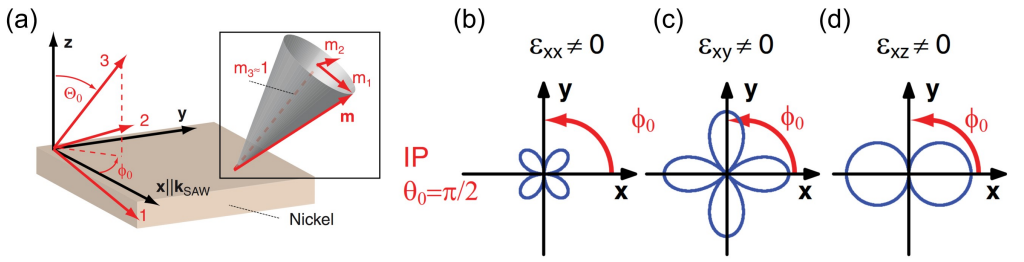

Figure 1.6: (a) Cartesian frame of reference (in black) and auxiliary frame of reference (in red). The precession of the magnetization is represented as a cone and m_1 and m_2 represent the dynamical components of the magnetization. (b-d) Polar plot of the MEC driving field's magnitude $|\mu_0 \mathbf{h}_{\text{eff, MEC}}|$ in case of the magnetization IP ($\theta_0 = \pi/2$). The distance from the origin indicates the magnitude of the driving field. Adapted from [18].

where c_{ij} are the components of the stiffness tensor. Details on how to experimentally determine B_i can be found in Ref. [26].

Before addressing the case of dynamic strain, let's introduce how at the $\mathbf{H}_{\text{eff, MEC}}$ looks like in the case of a thin film with cubic lattice. In Ref. [18] there is the full derivation of the expression for $\mathbf{H}_{\text{eff, MEC}}$ in the most general case, here we limit the discussion to the main results and to the case of interest in the framework of this thesis. To derive the components of the MEC effective field acting on the magnetization, it is useful to introduce a new reference frame - shown in red in Fig. 1.6.a - where the dynamic components of the magnetization are confined to a plane without losing generality; $m_1 = M_1/M_s$ and $m_2 = M_2/M_s$ in Fig. 1.6.a are therefore the dynamical components of the magnetization, subjected to the strain generated by Surface Acoustic Wave (SAW) with $k_{\text{SAW}}||x$. The MEC effective fields components $h_{\text{eff, MEC}_1}$ and $h_{\text{eff, MEC}_2}$ in the new reference system at a fixed time can be written as [18]:

$$\begin{aligned}\mu_0 h_{\text{eff, MEC}_1} = &-2b_1 \sin\theta_0 \cos\theta_0[\epsilon_{xx}\cos^2\phi_0 + \epsilon_{yy}\sin^2\phi_0 - \epsilon_{zz}] - 2b_2[(\epsilon_{xz}\cos\phi_0 + \\ &\epsilon_{yz}\sin\phi_0)\cos(2\theta_0) + 2\epsilon_{xy}\sin\theta_0\cos\theta_0\sin\phi_0\cos\phi_0]\end{aligned} \tag{1.9}$$

$$\begin{aligned}\mu_0 h_{\text{eff, MEC}_2} = &+2b_1 \sin\theta_0 \sin\phi_0 \cos\phi_0[\epsilon_{xx} - \epsilon_{yy}] \\ &- 2b_2[\cos\theta_0(\epsilon_{yz}\cos\phi_0 - \epsilon_{xz}\sin\phi_0) + \epsilon_{xy}\sin\theta_0\cos(2\phi_0)]\end{aligned} \tag{1.10}$$

where $b_i = B_i/M_s^2$ and θ_0 (ϕ_0) is the polar (azimuthal) equilibrium angle, as depicted in Fig. 1.6.a.

The polar plots in Fig.1.6.b-d report the modulus of $\mathbf{h}_{\text{eff, MEC}}$ in the case of in-plane (IP) magnetization ($\theta_0 = \pi/2$). It is immediately apparent that $\mathbf{h}_{\text{eff, MEC}}$ vanishes when is either collinear or orthogonal to $\mathbf{M}$, while it is maximum for $\phi_0 = 45°(n\pi/2)$ [18, 29, 30]. Furthermore, ϕ_0 (and also θ_0 when $\neq 0$) is defined by the equilibrium magnetization, meaning that $\mathbf{h}_{\text{eff, MEC}}$ is defined by $\mathbf{M}$ in both direction and strength. Here we derived the effective field for a static generic strain but in the more general case of $\epsilon_{ij} = \epsilon_{ij}(\mathbf{r}, t)$ means that the MEC contribution to the magnetization dynamics dependent on the $\mathbf{M}(\mathbf{r}, t)$ itself, and MEC coupling can be considered as a self-interaction of the magnetic system. It follows that a back-action of the magnetization on the strain should also be taken into account when calculating $\mathbf{h}_{\text{eff, MEC}}$; however, this aspect is particularly relevant whenever the amplitude of the resulting magnetization dynamics is greater or

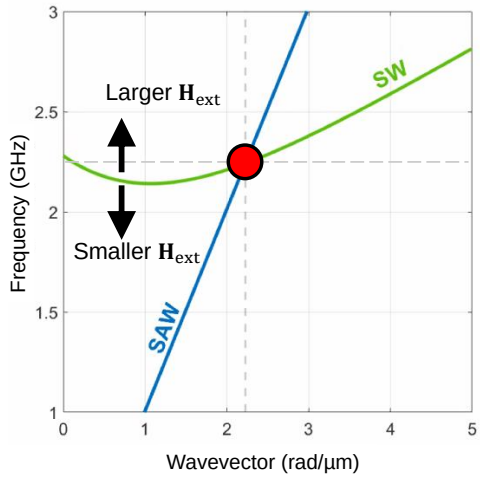

Figure 1.7: Scheme of a generic SAW (in blue) and SW dispersion (in green). At fixed wavevector, the intensity of the external field $\mathbf{H}_{\text{eff}}$ can be tuned to shift vertically the SW dispersion and make it degenerate with the SAW one.

comparable to that of the lattice. The above derivation does not include this aspect, which is not relevant in the context of this thesis; the interested reader can find more details in [18, 31]. It is intuitive that if the strain $\epsilon_{ij}(\mathbf{r}, t)$ is harmonic in space and time, as the one generated by a SAW, the resulting $\mathbf{h}_{\text{eff, MEC}}$ can drive SWs with the same k_{SAW}, as it has also been observed experimentally [32]. In general, as in the case of any kind of excitations, to enhance MEC it is convenient - but not necessary [33] - that the SAW and SW dispersion are degenerate. Typically, this naturally occurs for SAW and SW in the GHz range. However, in experiments, the SAW is usually generated with a specific wavevector k_{SAW} which is generally not degenerate with the normal SW modes present in the system. Nonetheless, since the effect of an external magnetic field on SW dispersion is to shift it vertically along the frequency axis, it is possible to adjust H_{ext} to achieve degeneracy. Fig. 1.7 schematically illustrates this process, which is also utilized in Ch. 4. Note that, in principle, the same effect can also be achieved by varying the direction of $\mathbf{H}_{\text{ext}}$; however, it can be more challenging from the point of view of experiments. When degeneracy is reached, the SW *resonate* with the RSAW, and large precessional magnetic dynamics is observed [34]. This phenomenon is the so-called SW resonance. However, if the SW dispersion is relatively flat at low wavevectors - meaning that the frequency of SW in that range of k does not significantly differ from that of FMR - the SW resonance can be effectively considered as acoustically driven FMR (from now on SAW-FMR), even if the SAW imposes a finite wavevector via inverse magnetostriction. Fig. 1.8 schematically depicts the concept of SAW-FMR, where the rf field that allows precession of $\mathbf{M}$ at a constant θ_{res} is not provided by an electromagnetic (EM) field but rather by the rf acoustic field generated by the SAW.

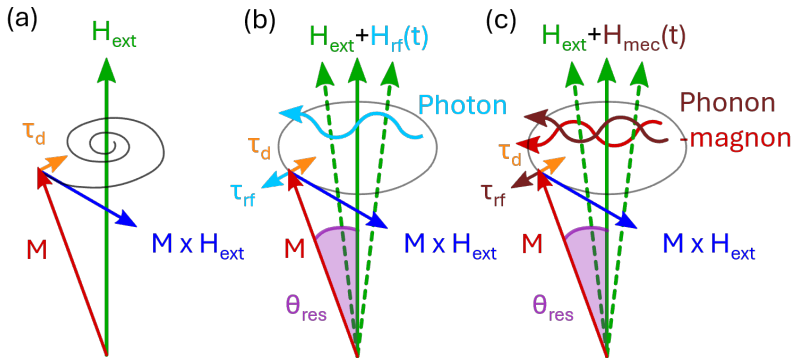

Figure 1.8: (a) Larmor precession. When no time-dependent field is applied the magnetization **M** tends to align along the static external field $\mathbf{H}_{\text{ext}}$ due to damping. (b) Photon-mediated FMR. **M** precesses at a constant angle θ_{res} when an appropriate rf EM field is applied (c) Phonon-mediated FMR. The rf field is the acoustic field generated by the SAW. Adapted from [35].

1.4.1 Elastically-driven magnetization dynamics in the case of dominant longitudinal strain

With reference to the previous section, we examine here the specific case of mainly longitudinal SAW. In practice, this means $\epsilon_{xx} \gg \epsilon_{ij}$; therefore, Eq. 1.9 and 1.10 can be rewritten as

$$\mu_0 h_{\text{eff, MEC}_1} = -2b_1\epsilon_{xx} \sin\theta_0 \cos\theta_0 \cos^2\phi_0 \tag{1.11}$$

$$\mu_0 h_{\text{eff, MEC}_1} = 2b_1\epsilon_{xx} \sin\theta_0 \sin\phi_0 \cos\phi_0 \tag{1.12}$$

Furthermore, if **M** lies IP the only non-vanishing effective field is

$$\mu_0 h_{\text{eff, MEC}_1} = 2b_1\epsilon_{xx} \sin\phi_0 \cos\phi_0 \tag{1.13}$$

The torque acting on **M** is calculated by transforming back to the original Cartesian coordinate system [18, 36], where in the (x, y) plane we have:

$$\mathbf{m} = \begin{pmatrix} \cos\phi_0 \\ \sin\phi_0 \end{pmatrix} \tag{1.14}$$

$$\mu_0 h_{\text{eff, MEC}_1} = 2b_1\epsilon_{xx} \sin(2\phi_0) \begin{pmatrix} -\sin\phi_0 \\ \cos\phi_0 \end{pmatrix}, \tag{1.15}$$

Therefore, the resulting MEC torque is:

$$\boldsymbol{\tau}_{\text{MEC}} = \mathbf{m} \times \mu_0 \mathbf{h}_{\text{eff, MEC}} = \hat{\mathbf{z}} b_1 \epsilon_{xx} \sin(2\phi_0), \tag{1.16}$$

which points out-of-plane (OOP) and is in phase to the strain.

This experimental setup is quite common in the literature, as most studies on MEC coupling involve generating SAWs using interdigitated transducers (IDTs) [18, 29, 37] on piezoelectric substrates. These transducers are designed to produce primarily longitudinal waves, such as Rayleigh Surface Acoustic Waves (RSAWs) and Skimming Surface Longitudinal Waves (SSLWs). While the SSLW is purely longitudinal, the RSAW also

has other non-zero components; however, the ϵ_{xx} component is dominant. The same acoustic dynamics can be optically induced via TG spectroscopy [20, 38], as it will be extensively discussed below.

CHAPTER 2

Time-resolved all-optical methods

This chapter introduces the all-optical pump-probe techniques employed in this thesis focusing on their application to investigate acoustic and magnetic excitations.

The pump-probe approach is illustrated schematically in Fig. 2.1. In a pump-probe experiment, an optical pump pulse excites the sample into a non-equilibrium state. The initial excitation process is typically much faster than the phenomena under study and can be considered to occur suddenly at an instant referred to as *time zero* whose time duration corresponds to the excitation pulse duration, generally in the 10-300 fs range. The effective pumping configuration can be more complex than a single pulse, as in the case of TG spectroscopy. The non-equilibrium state created by the pump pulse involves a non-thermal distribution of particles and quasi-particles, which typically depends on the pulse duration and wavelength of the pump beam. The sample then relaxes towards the free energy minimum, through a series of out-of-equilibrium states along the de-excitation path that ultimately convert the incident pump energy into thermal energy. The probe beam samples, via increasingly delayed snapshots, the relaxation process, delivering a sequence of signals that provides insight into the sample's transient states crossed on the way to thermalization.
To observe slow dynamics (e.g acoustic or thermal), a continuous wave (CW) laser can be used as the probe beam, with changes in its interaction with the sample (such as intensity and polarization) being continuously monitored using fast detection methods, that set the time resolution (typically $>$ ns). For faster dynamics (down to the tens of fs), a stroboscopic approach with pulsed probe beams must be employed. In this case, the time resolution is set by the pump pulse duration. The probe pulse is mechanically delayed with respect to the pump pulse, typically using retroreflector mirrors on a mechanically adjusted delay line. The signal at each fixed delay is acquired by averaging hundreds of thousands of pump-probe events to improve statistical accuracy. Therefore, the repetition rate of the pulsed laser source plays a critical role in this kind of measurement.

2.1 Magneto-optical effects

It is well known that light in a vacuum is unaffected by a static magnetic field. However, when light passes through or reflects off materials, because of light-matter interaction, its polarization is influenced by the presence of an external magnetic field or by the material's magnetization state. These interactions are called magneto-optical (MO) effects. MO effects have found applications not only in optoelectronic devices [40] but also as

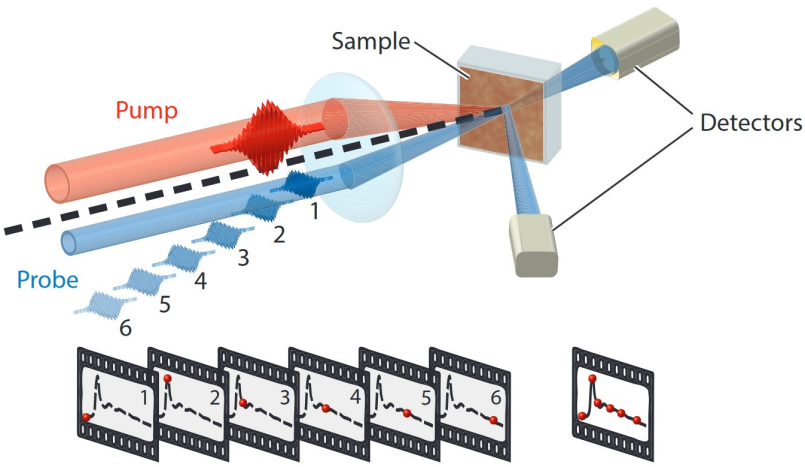

Figure 2.1: Scheme of an optical pump-probe experiment. The pump pulse excites the sample; the probe pulse, at variable time-delay, probes the instantaneous excited state of the system. The transient signal, acquired in transmission or reflection geometry, gives information about the relaxation path towards equilibrium. Adapted from [39].

methods for probing the physical properties and electronic structures of materials, particularly through MO spectroscopy, which is widely used for the investigation of static and dynamic magnetic properties.

A general derivation of the physical origin of MO effects is provided in Ref. [41]. The main result is that the MO are due to the off-diagonal components of the dielectric tensor [41, 42]

$$\bar{\bar{\epsilon}} = \epsilon \begin{pmatrix} 1 & iQ_z & -iQ_y \\ -iQ_z & 1 & iQ_x \\ iQ_y & -iQ_x & 1 \end{pmatrix} \tag{2.1}$$

where ϵ is the isotropic part of the dielectric constant and Q_x, Q_y, Q_z are the components of the Voigt vector $\mathbf{Q}$. In particular, off-diagonal components are assumed to preserve time-reversal symmetry when the magnetization is reversed, specifically $\epsilon_{ij}(\mathbf{M}) = \epsilon_{ji}(-\mathbf{M})$. Furthermore, when expanded to linear terms in $\mathbf{M}$, the components for $i \neq j$ are found to be proportional to the corresponding components of $\mathbf{M}$.

Faraday Effect and Magneto Optical Kerr Effect (MOKE)

In this section, following Refs.[41–43], we provide a phenomenological description of the Faraday and MOKE effects.

The fundamental microscopic mechanism is rooted in the magnetization of the sample, which breaks the symmetry of its interaction with light. This occurs through a combination of several factors. The Zeeman splitting causes the energy levels of electrons with different spin states to be renormalized in the presence of a magnetic field or internal magnetization. The SOC links the spin of electrons to their orbital motion, which alters the optical properties of the material based on the spin state and the polarization of light. The circular birefringence arises from the difference in refractive indices for left- (LCP) and right-circularly polarized light (RCP), leading to rotation or ellipticity in the

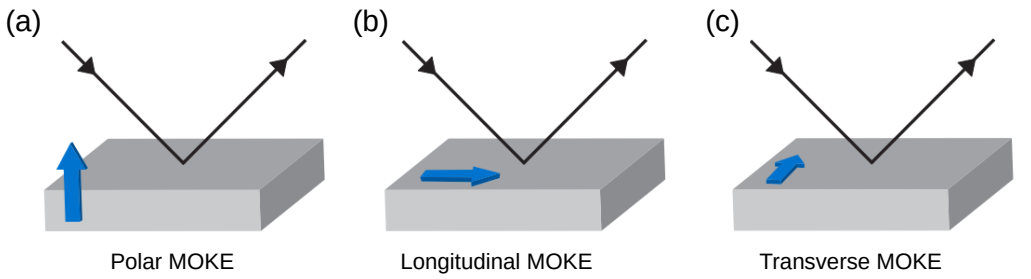

Figure 2.2: Scheme of the possible geometries for MOKE, defined by the orientation of the magnetization (in blue) to the sample surface and to the reflection plane. Adapted from [3].

polarization of the transmitted or reflected light. Furthermore, the different absorption coefficients for LCP and RCP light lead to a mismatch of the amplitudes of the emergent electric fields, resulting in a certain degree of ellipticity of the transmitted or reflected light. It can be demonstrated [43] that the complex refractive index experienced by the LCP and RCP light components can be expressed as

$$\tilde{n}_{\text{LCP, RCP}} \approx \tilde{n}\left(1 \pm \frac{1}{2}\mathbf{Q}\cdot\mathbf{u}_k\right) \tag{2.2}$$

where $\mathbf{k}$ is the wavevector of the incident light. $\hat{\mathbf{u}}_k = \mathbf{k}/k$ its versor and $\mathbf{Q}$ is the Voigt vector, proportional to the magnetization.

The polarization state is thus affected by

$$\tilde{\theta} = \frac{\pi LN}{\lambda}(\tilde{n}_{\text{LCP}} - \tilde{n}_{\text{RCP}}) = \frac{\pi LN}{\lambda}\mathbf{Q}\cdot\mathbf{u}_k = \theta_k + i\epsilon_k \tag{2.3}$$

where L represents the thickness of the magnetic material, N is the number of dipoles induced by the incident beam, and λ denotes the wavelength of the radiation. In particular, θ_k is the rotation angle of the polarization ϵ_k the ellipticity of the transmitted/reflected beam. Eq.2.3 clearly shows that the product $\mathbf{Q}\cdot\hat{\mathbf{u}}_k$ determines both the rotation and the ellipticity of the reflected - or transmitted - light beam, and the maximum polarization variation is observed when $\mathbf{k}||\mathbf{M}$. This is the reason why Faraday polarimetry[1], being in transmission, is mostly sensible to the OOP magnetization. On the other hand, MOKE polarimetry can be used to probe both OOP and IP magnetization, combining the three experimental schemes depicted in Fig. 2.2.

2.1.1 Time-resolved light polarimetry

From the above discussion, light polarimetry can also be used to probe magnetic excitations. Typically, the transient magnetic dynamics is investigated by measuring the variations in the polarization state of the transmitted or reflected probe beam as a function of the time delay Δt with respect to the pump pulse. The experimental setup usually includes an electromagnet to both magnetically saturate the sample and to investigate the magnetic-field dependence. Short (pump) laser pulses can trigger magnetic dynamics via thermal [17] and nonthermal effects [44, 45]. Thermal effects arise as the pump

[1]Polarimetry is the measurement and interpretation of the polarization of electromagnetic waves.

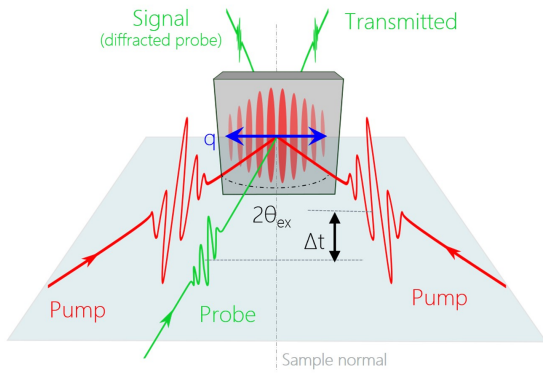

Figure 2.3: Sketch of the TG working principle. Two degenerate pump beams impinge on the sample at an angle θ_{ex} relative to the sample surface normal. Upon interference, they create an optical grating with a spatial period Λ. The spatially periodic modulation of the optical constants results in the probe being diffracted at the phase-matching angle, whose properties (e.g. intensity and polarization state) are measured as a function of the time delay Δt.

light is absorbed, leading to local heating. The thermal energy impulsively released by the pump, leads to a quenching of the magnetization and softening of the magnetic anisotropy, impulsively altering the energy landscape. The consequent non-equilibrium transient states can lead for example to excitation of SWs [17] or switching of the magnetization [46]. This excitation mechanism will be extensively discussed in Ch. 5. Non-thermal effects are triggered by the pump electric field, rather than by its intensity. For example, in [45] it is shown that ultrafast magnetization can be driven exploiting the magnetic field associated to the pump pulse itself via Inverse Faraday Effect (IFE). This is a non-thermal mechanism in the sense that occurs on timescales before the input energy has degraded.

The pump-induced magnetization dynamics can then be probed by tr-Faraday or tr-MOKE polarimetry, depending on the experimental setup and sample opacity.

2.2 Transient Grating Spectroscopy

TG is a Four-Wave-Mixing (FWM) spectroscopy involving three laser beams with non-collinear $\mathbf{k}$ that is specifically designed for the time-resolved investigation of finite wave vector excitations. In a typical TG experiment, two spatially and temporally overlapped coherent pulsed laser beams impinge on the sample at angles $\pm\theta_{ex}$ from the sample surface normal, as shown in Fig. 2.3. The interference of the two beams on the sample generates a periodic modulation of the optical field perturbing the sample, with the corresponding wavevector depending on both the experimental geometry and the wavelength of the pump beams. Upon light-matter interaction, the optical pattern populates some excited states with the same spatial periodicity at the corresponding wavevector. The consequent time-dependent spatial modulation of the dielectric tensor (the so-called *transient grating*) causes the probe beam to be diffracted, just as it happens from a physical grating. The diffraction efficiency is directly related to the extent of deviation of the optical properties from equilibrium; therefore, the time-dependent properties of the diffracted beam (e.g. intensity, polarization) directly related to the TG-induced excita-

tions. Diffraction ends once the sample reaches its equilibrium state. The time scales of these induced transients vary significantly, ranging from tens of femtoseconds (for electronic [47] and magnetic [48, 49] transients) to picoseconds (involving optical phonons [50], spin diffusion [51], exciton dynamics [52] and high-energy (exchange) magnons [53]), to nanoseconds (associated with acoustic phonons [54] and low-energy (dd- or MEC-mediated) magnons [19, 20]), and extending further in times (encompassing thermal diffusion [55]). Overall, the entire process can be viewed as a single-step convolution of the three input beams with an appropriate sample response function, leading to dielectric polarization that generates the emitted beam.

This section is organized as follows: after a brief introduction to the TG as a FWM process, I will proceed with a more practical description, treating the TG as a three-step process. Finally, we will discuss two examples of TG-induced dynamics that are relevant to the focus of this thesis.

2.2.1 Transient grating as a FWM process

In the field of non-linear optics, frequency mixing is a well-known phenomenon [56, 57]. In these processes, a beam of monochromatic light interacting with atoms can be partially converted into light, whose frequencies are harmonics of the fundamental frequency. Similarly, beams of two or more different frequencies can combine to produce light beams at one or more number of various frequencies. In a more rigorous picture this effect can be explained taking into account the different components of the nonlinear polarization, which generate electromagnetic waves having frequencies different from those of the incident waves [57, 58]. In such processes, energy and momentum must be conserved, imposing certain conditions on the energies and wavevectors of the emitted photons. These conditions are governed by what is known as the phase-matching condition [59, 60]. FWM is a particular case of nonlinear frequency mixing, which arises from the interaction of three coherent optical fields that the third-order nonlinear susceptibility tensor $\boldsymbol{\chi^{(3)}}$ generate a fourth beam [61, 62]. In the specific case of a TG experiment, the three incoming beams interact with the medium, generating a nonlinear polarization $P_i^{(3)}(\mathbf{r}, t)$, which acts as the source of the diffracted field. The TG signal is produced in a well-defined direction, determined by the phase-matching condition; specifically, the wavevector of the TG signal $\mathbf{k}_\mathrm{s}$ can be written as

$$\mathbf{k}_\mathrm{s} = \mathbf{k}_\mathrm{p1} + \mathbf{k}_\mathrm{p2} - \mathbf{k}_\mathrm{pr} \tag{2.4}$$

where $\mathbf{k}_\mathrm{pr}$ is the wave vector of the probe beam, $\mathbf{k}_\mathrm{p1}$ and $\mathbf{k}_\mathrm{p2}$ are the wavevectors of the two pump beams. As shown in Fig. 2.4, the phase matching condition can be satisfied in both transmission and reflection.

In this FWM picture, the whole process can be described as the convolution of the incoming electric field and an appropriate response function. The component of the third order polarization can be then written as [62]:

$$\begin{aligned} P_i^{(3)}(\mathbf{r}, t) = \int d\mathbf{r}_1 d\mathbf{r}_2 d\mathbf{r}_3 \int dt_1 dt_2 dt_3 \, E_j(\mathbf{r}_1, t_1) E_k(\mathbf{r}_2, t_2) E_l(\mathbf{r}_3, t_3) \\ \cdot \mathcal{R}_{ijkl}^{(3)}(\mathbf{r} - \mathbf{r}_1, \mathbf{r} - \mathbf{r}_2, \mathbf{r} - \mathbf{r}_3, t - t_1, t - t_2, t - t_3), \end{aligned} \tag{2.5}$$

where $E_i \, (i = x, y, z)$ is the i-th component of an input electric field, the space and time indexes 1 to 3 refer to the three input beams, and $\mathcal{R}_{ijkl}^{(3)}$ is the third-order response

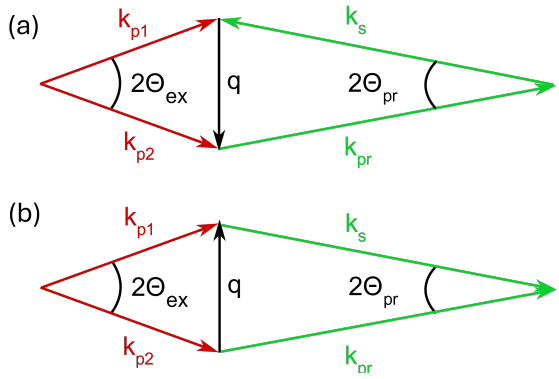

Figure 2.4: The phase-matching condition in a TG experiment is shown for both (a) transmission and (b) reflection geometries. The TG-induced wavevector is given by: $\mathbf{q} = \mathbf{k}_{\mathrm{p1}} - \mathbf{k}_{\mathrm{p2}} = \mathbf{k}_{\mathrm{pr}} - \mathbf{k}_{\mathrm{s}}$ where $2\theta_{\mathrm{ex}}$ is the angle between the two pump pulses, and θ_{p} is both the incidence angle of the probe relative to the sample normal and the scattering angle of the diffracted beam.

function; repeated indices are summed. Eq. 2.5 is very general and accounts for space and time non-locality, and sets the definition for the response function $\mathcal{R}^{(3)}_{ijkl}$ [55, 62]. It can be demonstrated [63], that the dielectric constant modulation variation induced by the pumps in the sample is

$$\delta\varepsilon(\mathbf{q},t) \propto \chi^{(3)}(\mathbf{q},t)\Big[E_{p,1+2}(\mathbf{q},t)\Big]^2 \tag{2.6}$$

where $E_{p,1+2}(\mathbf{q},t)$ is the sum of the fields of the two excitation pulses. The measured signal can be expressed in terms of $\chi^{(3)}(\mathbf{q},t)$

$$I(\mathbf{q},t) \propto |E^2_{\mathrm{p1}} E_{\mathrm{pr}} \chi^{(3)}(\mathbf{q},t)|^2 \tag{2.7}$$

where $E_{\mathrm{p1}} = E_{\mathrm{p2}}$ and E_{pr} are respectively the magnitude of the pump and probe fields. Since $\chi^{(3)}$ contains information on how the pump fields interact with the sample, the measured TG signal gives a direct insight into the excited modes and their evolution over time. This description is very effective from a formal point of view, but it is not really of practical intuition. In the following, we will discuss a TG experiment in a three-step process, which holds in the case where the pumping and probing mechanisms can be considered separately.

2.2.2 Transient grating as a three-step model

Following Ref.[64] the whole TG-FWM process can be described as a three-step model - as schematically depicted in Fig. 2.5 - involving i) formation of the optical grating ii) transient spatial modulation of the optical constants upon light-matter interaction iii) diffraction of the probe beam. Each step is described below.

Formation of the optical grating

The initial step of the model involves the two pump beams, which are identified with the subscripts $i = 1, 2$. Let's consider a reference frame where the sample lies in the (x,y)

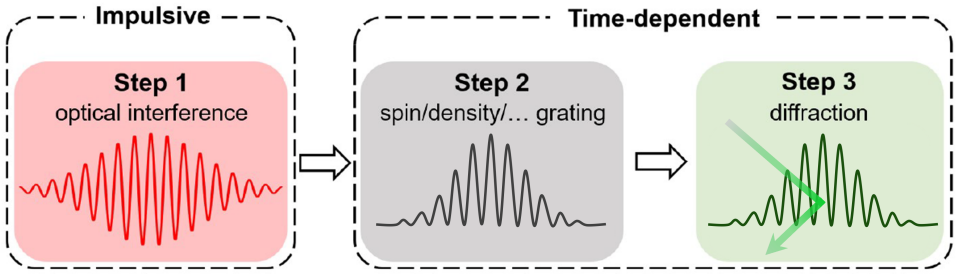

Figure 2.5: Diagram describing the three main steps of TG Spectroscopy. The process begins with the creation of an impulsive optical grating (Step 1), which initiates an excitation within the sample via light-matter interaction (Step 2). This excitation interacts with the optical properties, leading to a spatial-and-time-dependent modulation of the optical constants that causes the probe beam to be diffracted (Step 3).

plane and the optical axis is along the z-direction. The two pumps are considered as coherent pump pulses generated by the same source, of equal complex amplitude $\mathbf{E}_{\mathrm{p,i}}$, having wavelength λ_{ex}, optical frequency ω_{p}, time duration τ_{p}, and s-polarization. In the chosen reference frame, they impinge on the sample at an angle $\pm\theta_{\mathrm{ex}}$ with the sample normal; by geometry $k_x = \pm|\mathbf{k}|\sin\theta_{\mathrm{ex}}$ and $k_z = |\mathbf{k}|\cos\theta_{\mathrm{ex}}$. Their interference on the sample produces an intensity profile [64]

$$I \propto \frac{|\mathbf{E_p}|^2}{2}\left[1+\cos(2k_x x-\phi)\right], \tag{2.8}$$

where ϕ is the general phase between the optical fields. Therefore, the effect of the phase difference between the two optical fields is just to laterally translate the grating along x and the intensity is spatially modulated with a periodicity

$$q = \frac{2\pi}{\Lambda} = 2k_x = \frac{4\pi\sin\theta_{\mathrm{ex}}}{\lambda_{\mathrm{ex}}}. \tag{2.9}$$

Note that the $\mathbf{q}$ is IP due to geometry and depends on the experimental geometry trough θ_{ex} and λ_{ex}. Typically in the optical range the TG pitch Λ is of the order of µms, but can be reduced down to the few-tens-of nm by pumping in EUV/x-ray range [65].

Here, we have derived the main feature of two s-polarized pump pulses interfering on the sample. However, different types of gratings can be obtained by playing with the polarization of the pump beams, as depicted in Fig. 2.6. This thesis will focus on the results obtained using intensity gratings only. However, the possibility of generating pure polarization gratings represents an alternative approach to investigate spin diffusion [51], excitonic dynamics [66] or magnetization dynamics [48] via nonthermal effects.

2.2.3 Interaction with the sample

The optical grating is transferred to the sample via a light-matter interaction - such as, for example, absorption - which results in a spatial modulation of the optical properties, depending on the material. This can be understood in terms of the population of cer-

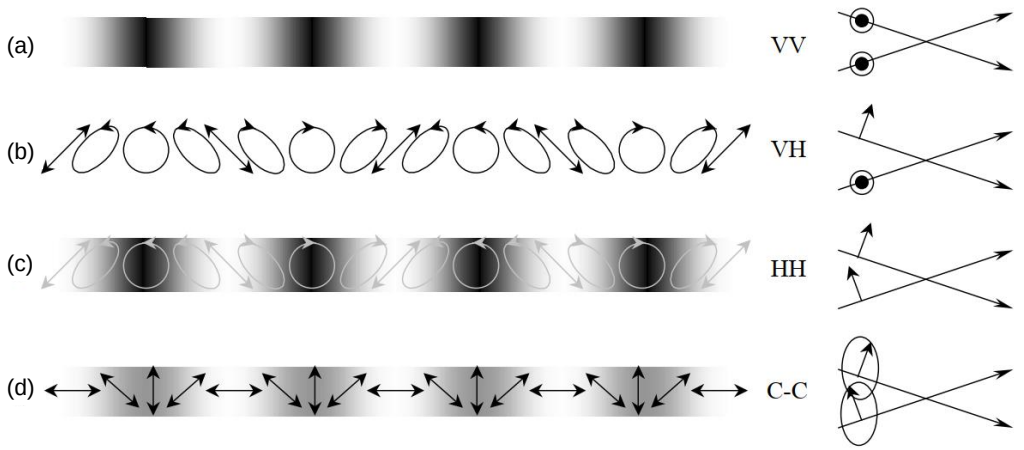

Figure 2.6: Different kinds of interference gratings depending on the polarization of the impinging pump beams. V, H, and C indicate s-polarized, p-polarized, and circularly polarized beams, respectively. Field intensity is represented as a grayscale, while the arrows represent the polarization. (a) Pure intensity grating resulting from interference of two s-polarized beams (VV). (b) Pure polarization grating generated by an s-polarized beam and p-polarized beam (VH). (c) Mixed intensity and polarization grating originating from two p-polarized beams (HH). (d) Mixed intensity and polarization grating produced by two circularly polarized beams (CC). Adapted from Ref.[67].

tain states, e.g. electronic, phononic or magnonic; in this sense, the optical grating upon light-matter interaction translates into a population grating. The description in terms of excited-state populations is necessary if locally the population density is out of equilibrium, namely if the energies of the excited states are $\gg$ than the thermal energy k_BT. However, in most cases, this condition is verified on the sub-ps timescale, due to the short hot-phonons lifetime. Once thermalization is locally reached, thermodynamical properties such as temperature, concentration etc., describe well the resulting grating, even if the sample in its entirety is not at equilibrium due to the spatial modulation imposed by the excitation. A wide class of light-induced gratings is quasi-stationary (e.g. temperature gratings), meaning that the grating amplitude undergoes an exponential decay over time (e.g. thermal diffusion). However, other mechanisms can cause grating amplitude oscillations related to wave propagation. For example, a temperature grating can induce local density (magnetization) gradients leading to standing acoustic waves (spin waves). As a result, in such cases, the TG signal reflects contributions from both phenomena: damped oscillations related to coherent dynamics, superimposed on a slowly decaying exponential background associated with incoherent dynamics. Throughout all phases - i) excitation, (ii) thermalization, and (iii) diffusion/coherent dynamics - the optical constants are spatially and temporally modulated. The interested reader can consult Ref. [64] for the formalism that allows for the link between the amplitude of the pump fields and the variation of the susceptibility tensor.

2.2.4 Diffraction from transient gratings

Upon interaction with the sample, the probe beam is diffracted (as in the case of static grating) by the time and spatially dependent optical variation of the susceptibility tensor; the modulation entity, the so-called grating depth, determines the amplitude of the diffracted beam intensity. When the grating depth d is bigger than the TG pitch Λ, diffraction angle of the scattered beam is completely determined by the Bragg condition [64]:

$$\mathbf{k}_{\mathrm{s}} = \mathbf{k}_{\mathrm{pr}} + m\mathbf{q}, \quad m = \pm 1, \pm 2 \dots \tag{2.10}$$

meaning that the TG-induced dynamics can be probe efficiently only when the phase matching condition is met (see. Fig. 2.4). Considering $m = 1$, it follows that $|\mathbf{k}_{\mathrm{s}}| = |\mathbf{k}_{\mathrm{pr}}|$, or equivalentl,y that $\theta_{\mathrm{pr}} = \theta_{\mathrm{s}}$. Therefore, the probe is scattered at a well-defined - and predictable - angle.

General details on the efficiency of the scattered probe depending on the grating thickness can be found in Ref. [64]. Here, we focus on the phenomenology discussed in the following chapters, which is the case of a quasi-static grating coexisting with another grating leading to coherent dynamics. This is, for example, the case of a temperature grating superimposed on a density grating, which gives rise to standing SAWs. In this picture, the vertical surface displacement amplitude due to the thermal grating and counter-propagating SAWs is given by [68]

$$u(t) = S_{\mathrm{th}}(t) + Ae^{-t/\tau}\cos\omega t, \tag{2.11}$$

where $S_{\mathrm{th}}(t)$ describes the (exponential) decaying amplitude of the thermal grating, $A/2$ is the amplitude of each of the counter-propagating SAWs, τ is the SAW decay time, and ω is the SAWfirst angular frequency. The efficiency for the first order of diffraction can be expressed as [64]

$$\frac{I_D}{I_C} = \eta = \left|\frac{\pi\Delta\tilde{n}d}{\lambda_p}\right|^2 \tag{2.12}$$

where $\Delta\tilde{n}(t)$ is the TG-induced variation of the complex refractive index. By assuming $\Delta\tilde{n}(t) \propto u(t)$ the η in this case can be written as

$$\begin{aligned}\eta(t) \propto & |S_{\mathrm{th}}(t) + Ae^{-t/\tau}\cos\omega t|^2 = \\ & = S_{\mathrm{th}}^2(t) + 2AS_{\mathrm{th}}(t)e^{-t/\tau}\cos\omega t + \frac{1}{2}A^2e^{-2t/\tau}(1+\cos 2\omega t)\end{aligned} \tag{2.13}$$

Eq. 2.13 shows that depending on the relaxation time of the incoherent thermal grating, the time-dependent signal can assume different features. If the acoustic attenuation decays faster compared to the thermal background, the signal is dominated by an exponential decay with oscillations at the frequency ω; on the contrary, if the thermal contribution decays faster signal at 2ω appears, as also observed experimentally in Ref. [68, 69]. The same approach can also be generalized in the case of multiple coexisting gratings (see Ch. 5).

2.2.5 TG detection

The TG technique is background-free, a feature that arises from the phase matching condition, which causes the probe beam to be diffracted in a direction where no other beams

are present. This can be considered a practical advantage to some other techniques such as time-resolved reflectivity, Faraday, or MOKE, where the signal is a small modulation over a strong background, that needs to be properly isolated. The diffracted intensity is typically 10^{-6} that of the incident probe beam, and does not require complex instrumentation to be detected. For phenomena evolving on timescales shorter than the ns, a stroboscopic approach is usually necessary. On the contrary, for longer timescales the probe beam can also be a CW beam. The two detection methods will be better described in the next chapter, along with the setup description.

2.2.6 TG-induced thermal and acoustic dynamics

In this section, we will discuss the thermal and acoustic dynamics that can be triggered by an intensity grating, specifically in the TG configuration with both pump beams s-polarized.

If the primary electronic grating undergoes rapid de-excitation, the consequent temperature grating can lead to variations in optical constants through thermo-optical coupling. Additionally, the spatially-periodic high-temperature areas cause the material to expand, creating an equally-periodic density grating and a surface displacement grating [54, 70–72]. These effects are quasi-stationary and dissipate over time due to heat diffusion, occurring on timescales longer than nanoseconds. In this context, they represent the incoherent contribution to the signal. Associated with the thermal grating, the impulsive thermo-elastic expansion generates counterpropagating acoustic fronts; the thermal trigger's periodicity filters the broadband acoustic fronts, allowing only modes matching the TG wavevector q to interfere constructively and form standing acoustic waves at the very same wavevector q. Generally, depending on the sample, different waves at the same TG wavevector can be excited; however, they typically have different frequencies depending on their dispersion relation within the material [19, 54, 73]. Therefore, time-dependent variations in stress, density, and temperature generate time-dependent changes in the dielectric tensor, that are directly monitored trough the diffracted probe beam.

TG-induced magnetic textures and coherent magnons

The application of TG spectroscopy to the investigation of magnetization dynamics is rapidly gaining interest [20, 49, 74, 75], also thanks to the recent development of setups and methodologies for optical [76], extreme ultraviolet (EUV) [77–79] and hard x-rays [80] TG spectroscopy dedicated to magnetization-sensitive TGs. Up to now, the main results are obtained on 3d ferromagnetic materials where the magnetic dynamics is triggered by absorption of the intensity grating, namely two s-polarized beams impinging on the sample. Since the magnetization affects the off-diagonal components of the dielectric tensor, this dynamics is observable in polarization-analyzed TG. Within the tens of ps after the pump pulse, the magnetization partially recovers, and correspondingly the diffracted intensity fades away. This dynamics has been explored in thin films of ferrimagnetic alloys with perpendicular magnetic anisotropy employing EUV light gratings [49]. The quenching of magnetization and the thermal softening of magnetic anisotropy enables the excitation of coherent magnon precession on a sub-nanosecond timescale [17]. To observe this process a specific arrangement of the external field to the magnetic anisotropy axis is required, as it will be discussed in detail in Ch. 5. This, together with the periodic nature of the TG excitation, has been proven to be a valid method to trig-

ger magnons at the very same TG wavevector. The pioneering experiment showcasing this method has been implemented in a transmission electron microscope (TEM), exploiting the self-interference of a single pump to obtain the TG excitation scheme and Lorentz microscopy for detection[74]. This approach is thoroughly described in Ch. 5, where original experimental results are presented demonstrating the applicability of this method in both optical and EUV TG.

In the case of magnetic materials, polarization gratings represent another exciting option to manipulate the magnetization coherently. Although this excitation mechanism is well consolidated for the investigation of spin-length diffusion in magnetic semiconductor quantum wells [51], there is still no clear evidence that this approach can drive coherent magnons through nonthermal excitation; however, there have been first attempts reported with TG pumping in the EUV range [48]. A possible further direction is to employ this approach on magnetic oxides exhibiting IFE, such as $DyFeO_3$ [45] or NiO [81], where the spatial modulation of the polarization should be able to locally induce an impulsive nonthermal modification of the spin state that at later times could result in a coherent magnon, similarly to what happens in the thermally mediated case.

Part II

A TG approach to acoustics, magnetoacoustics and magnonics

CHAPTER 3

TG Spectroscopy@ the NFFA-SPRINT lab

TG spectroscopy has been extensively used to investigate thermal and acoustic dynamics on various timescales. In magnetostrictive materials, the triggered acoustic dynamics can also induce magnetization dynamics through magnetoelastic coupling. Here, we present the experimental setup developed at the NFFA-SPRINT (Nanoscale Foundries and Fine Analysis - Spin Polarization Resolved Instruments in the Nanoscale and Time domain) lab in Trieste during the first part of my Ph.D. project, in collaboration with Dr. P. Carrara, (Ph.D. student at the time) and Dr. R. Cucini (CNR-IOM). Currently, the setup is also open to external users upon successful proposal evaluation by the NFFA research infrastructure (www.trieste.nffa.eu). Our goal was to create an all-optical setup capable of performing TG spectroscopy to study acoustic dynamics on the relevant time scales for magnetodynamic studies using either a pulsed or a CW probe, also in combination with tr-polarimetry. In particular, the ability to investigate short timescales ($<$ ns) has proven to be necessary for studying TG-induced magnetic dynamics. This will be further discussed in Ch. 5, where we will examine the excitation of coherent magnons directly initiated by the spatially periodic temperature profile generated by TG, eliminating the need to rely on magnetoelastic coupling to excite magnons.

The experimental setup offers great versatility, enabling the easy additional implementation of time-resolved polarimetry, both in transmission and reflection geometry. This can be used in combination with the TG pumping mechanism [20] or within the standard single-pump scheme (see e.g. Ch. 6 or Ref. [82]).

Furthermore, the combination of different techniques in the same setup allows the characterization of various low-energy excitations (such as phonons and magnons) in the very same sample environment, minimizing the need to transfer samples to other experimental stations. Integrating multiple techniques provides unique opportunities to acquire data for consistent analysis, reducing uncertainties about the actual sample conditions in different setups. Although this approach has already been implemented in large-scale facilities, such as the NFFA suite connected with synchrotron radiation beamlines at Elettra [83], it is not yet common in tabletop experiments.

3.1 Operational mode 1 : TG spectroscopy with pulsed probe

The light source is a mode-locked amplified pulsed laser based on Yb:KGW gain medium (PHAROS, by Light Conversion); details on the PHAROS source and on the other available sources (High Harmonics Generation source and Optical Parametric Amplifiers) are reported elsewhere [84, 85]. One advantage of the PHAROS source is its adjustable repetition rate, which can be set anywhere from a single burst up to 1 MHz. This flexibility aids in optical alignment and allows precise tuning of experimental conditions to achieve the optimal compromise between signal quality (statistics) and unwanted pump-induced sample heating. Fig. 3.1 shows the setup to perform TG spectroscopy with pulsed probe. The setup is designed to work with the fundamental emission line of the PHAROS (1030 nm, 300 fs). The pump pulse duration sets the time resolution for this operational mode. Given the average power of 20 W, only 10% of its output is typically sufficient to run our experiments. This allows for parasitic operation when the PHAROS is simultaneously used as a laser source in other setups [84] of the NFFA-SPRINT suite. The fundamental beam is split by a 30/70 beamsplitter: 70% is used for the pump, 30% for the probe. The time delay between the two beam portions is managed using a corner cube retroreflector placed on a 50-cm-long mechanical delay stage, providing a maximum time delay of ~ 3.3 ns. Following the delay stage, the second harmonic of the fundamental frequency is produced in a 2-mm-thick BBO crystal and is used as the probe beam (515 nm, 250 fs). On both pump and probe branches, a half-wave waveplate followed by a polarizer (W1, P1, W2, P2) is inserted in the beam path. The polarizers are set to transmit only s-polarized light. By rotating half-wave plate, the polarization of the light beam changes accordingly, and a tunable portion of the beam passes through the polarizer. This configuration defines the polarization state of the beams incident on the sample, and ensures fine control of the fluence.

The pump and probe beams are combined using a dichroic mirror and focused with lenses (L1 and L2, focal length $f = 20$ cm) onto a diffractive phase mask (details provided below). The phase mask generates several diffraction orders: the ± 1 orders at 1030 nm are used as the pump, while the 515 nm orders are used as the probe beams, depending on the desired operational mode. To perform TG spectroscopy, either the $m = 1$ or $m = -1$ orders of the 515 nm beam can be used as the probe beam; in the sketch, the $m = 1$ order is considered as the probe beam. Note that the $m = \pm 2$ orders of the probe are collinear with the $m = \pm 1$ orders of the pump. This does not represent a problem as long as the probe intensity remains significantly lower, typically by a factor of 10-100 with respect to the pump. Furthermore, the TG generated by the $m = \pm 2$ orders of the 515 nm would cause the probe beam to scatter in a different direction than that determined by the phase matching condition for the TG generated by the $m = \pm 1$ diffraction orders of the fundamental. We can therefore conclude that they do not affect the measured TG signal.

The beams are then collimated and focused on the sample by a pair of custom-made achromatic doublets (D1 and D2, $f = 10$ cm, 3 inches in diameter) in a $4f$ confocal configuration; the advantages of this configuration are reported below. Typically, the pump and probe spot size on the sample is 50 μm (FWHM[1]) and 30 μm (FWHM), respectively; however, the footprint on sample can sligtly vary depending on the overall alignment.

To ensure the correct overall alignment, a Third Harmonic Generation (THG) crystal can be placed at the sample position, namely the focal point where the second dou-

[1] With FWHM is meant the Full Width at Half Maximum of the spatial gaussian profile of the beam.

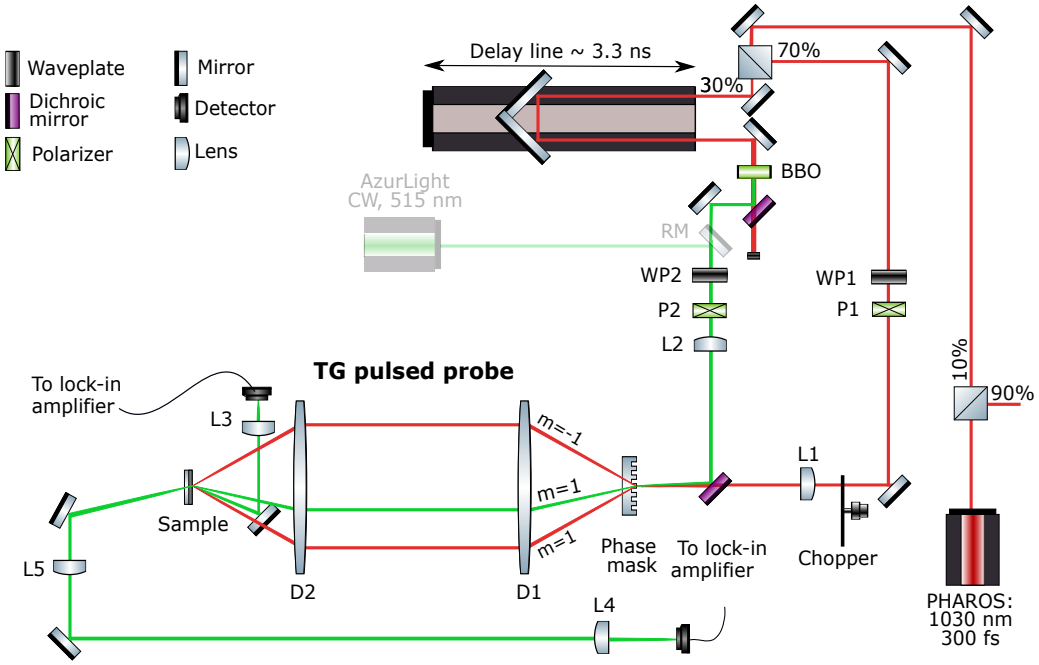

Figure 3.1: Sketch of the optical table for TG spectroscopy with pulsed probe at the NFFA-SPRINT lab. Components of the setup associated with other operational modes are displayed transparently in the background.

blet recombines the three beams of interest in its focal plane. THG occurs only if the pump and probe pulses are both spatially and temporally overlapped and if the crystal is properly oriented to meet the phase-matching condition. Therefore, generating the third harmonic from a THG crystal placed at the sample position ensures good overall alignment, which is crucial for observing the TG signal.

The diffracted beams, in both reflection and transmission geometry, are then collected by the detection branch and focused in a femtowatt photoreceiver (2151 Newport), whose output is fed into a lock-in amplifier (SR860 from Stanford Research Systems); the data are acquired through a homemade LabVIEW software. In reflection geometry, the sample is tilted downwards, to separate the probe and the TG signal: due to the phase matching condition, the two beams have the same propagation axis- The diffracted beam in reflection geometry is drawn in Fig. 3.1 at a different angle only for illustrative purposes. When working in transmission geometry, the two beams do not overlap and the sample surface plane can be set orthogonal to the scattering plane, thus ensuring more efficient spatial overlap and a smaller spot size on the sample. When dealing with acoustic dynamics, no polarization analysis is required, because the diffracted beam preserves the polarization of the incoming probe beam; the information about the TG-induced dynamics is encoded in the time-dependent fluctuation in intensity of the diffracted beam. However, for the TG-driven magnetic excitation reported in Ch. 5, a polarizer must be inserted in the detection branch to isolate the time-and-magnetization-dependent change of the diffracted probe beam, in the same way as in standard tr-Faraday or tr-MOKE.

On the advantages of using phase masks

A phase mask is a diffraction grating typically made of a transparent material with a negligible extinction coefficient. The grooves are mechanically etched into its surface: the optical phase accumulation is due to the varying amounts of material the light rays pass through. With proper design, a phase mask can maximize the intensity diffracted into specific orders, which is useful when only certain diffraction orders are of interest, as in our case the $m = \pm 1$ orders of diffraction of the pump and probe.

Phase masks have been used in TG setups for the past couple of decades [86], quickly becoming a popular and practical method to achieve overlap of short pulses [75, 87, 88]. Figure 3.2a-b illustrates the advantages of using a phase mask in combination with a pair of doublets. When the two pump beams are obtained from a $50/50$ beamsplitter, they do not exhibit any pulse-front tilt resulting in a spatially limited interference area Fig. 3.2a. Conversely, the pulse-front tilt introduced to a Gaussian beam when diffracted by the phase mask results in the propagation direction being at an angle relative to the pulse wavefront. While this can reduce time resolution by stretching the pulse duration, it also increases the overlapping area, thereby enhancing the signal-to-noise ratio. The experimental arrangement of the combination of phase mask and doublets is depicted in Fig. 3.2.b; the two doublets are set in confocal geometry, which means that if the two doublets have equal focal length f, the total distance from the front focus of D1 to the back focus of D2 is $4f$, with the doublets spaced $2f$ apart. This configuration eliminates the need for an additional delay stage to optimize the time overlap between the two pump beams, as they follow the same optical path. It also minimizes aberrations during the propagation of the Gaussian beams and reproduces a 1:1 image of the optical field present on the phase mask on the sample. Separate control over the polarization state of each pump beam can be easily achieved thanks to the space in between the doublets. Furthermore, if the probe beam is also one of the diffraction orders generated by the phase mask, e.g. $m = 1$, the scattered beam propagates exactly superimposed to the $m = -1$ order after the sample position. This is extremely useful to both finely align the detection branch - the scattered probe beam is typically not visible by eye - and in the case of heterodyne detection.

The phase masks employed in our setup are fabricated in the CNR-IOM lithography facility [89]. The groove depth h, duty cycle D and phase mask material, affect the efficiency of the diffraction orders for both pump and probe beams and have been taken into account for a successful fabrication process. Fig 3.2.d-e show the calculated efficiency for the 0th and 1st diffraction orders for the two relevant wavelengths and as a function of the groove depth. We choose a grooving depth of 750 nm to favour the diffraction of the $m \pm 1$ orders of the pump. Calculations were performed according to Ref. [90]. Given that the TG pitch on sample is related to the incident angles, to vary this quantity, we fabricated a set of phase masks with a nominal periodicity of 5.05, 6.01, ad 8.00 μm. Table 3.1 reports for each mask periodicity d, the corresponding pump angle of incidence θ_p, TG pitch Λ on sample and TG-wavevector q. Fig.3.2.d shows the Atomic Force Microscopy (AFM) characterization of the phase mask with a 5.05 μm periodicity. AFM scans are obtained in standard air conditions with a Solver Pro (NT-MDT) instrument, in semicontact mode using commercial cantilevers (NT-MDT, NSG30, nominal spring constant $k = 40$ Nm^{-1}, nominal radius of curvature 10 nm).

It should be highlighted that the confocal configuration of the doublets reproduces the optical field at the back focal plane of D2 exactly as it is at the front focal plane. When the pump beams are both s-polarized, the resulting TG intensity grating from

their interference has a spatial frequency that is doubled. Consequently, the pitch of the optical grating on the sample is half the pitch of the phase mask used.

Table 3.1: Experimental quantities depending on the phase mask periodicity d: incident angle of the pump with respect to the sample surface normal θ_{ex}, TG pitch Λ and TG wavevector q on sample.

d	θ_{ex} (°)	Λ (µm)	q (rad/µm)
5.05	11.6	2.54	2.47
6.01	10.0	3.07	2.05
8.00	7.5	4.00	1.57

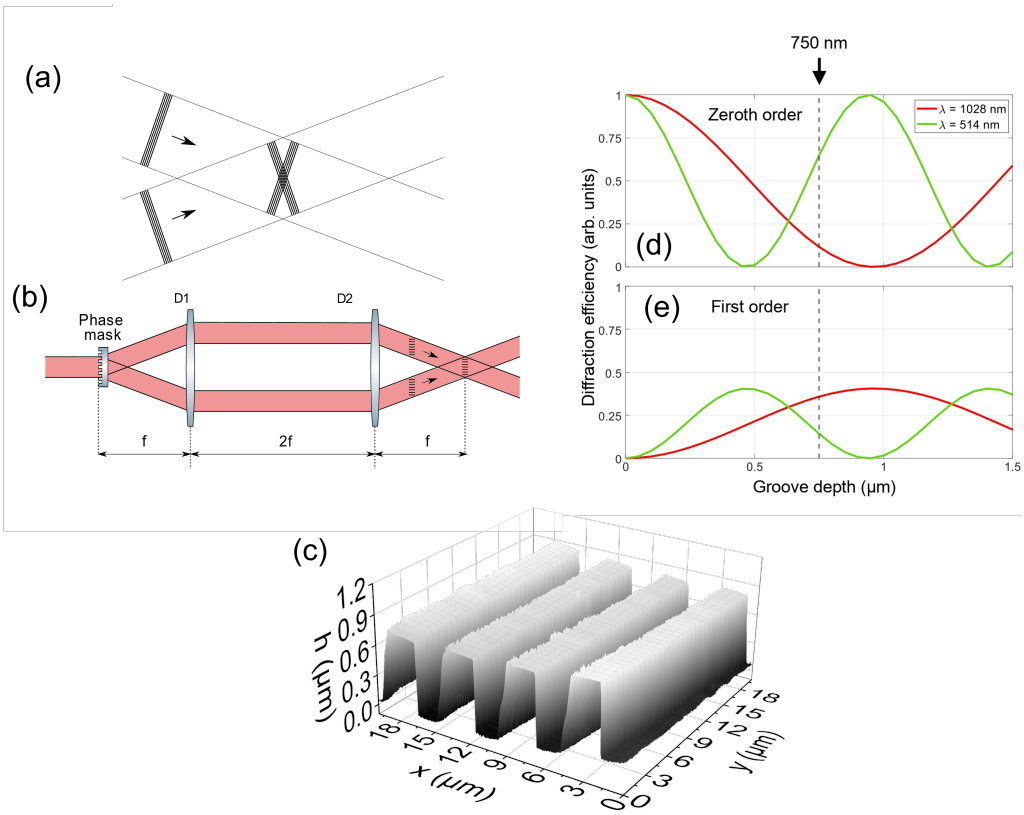

Figure 3.2: (a-b) If the pump pulses are obtained via a beamsplitter, no pulse-front tilt is introduced, resulting in reduced interference area. A diffractive phase mask in combination with a pair of doublets in confocal configuration introduces a pulse-front tilt in the propagating pulses, resulting in a larger overlap area. Adapted from [86]. (c) AFM measurement performed on the phase mask with a periodicity of 2.54 µm. (d-e) Computed diffraction efficiency for the zeroth and first orders as a function of the groove depth; the calculation, based on Ref. [90], considers α-quartz masks and rectangular cross-section of the grooves. The vertical dashed lines indicate the depth chosen for the fabrication.

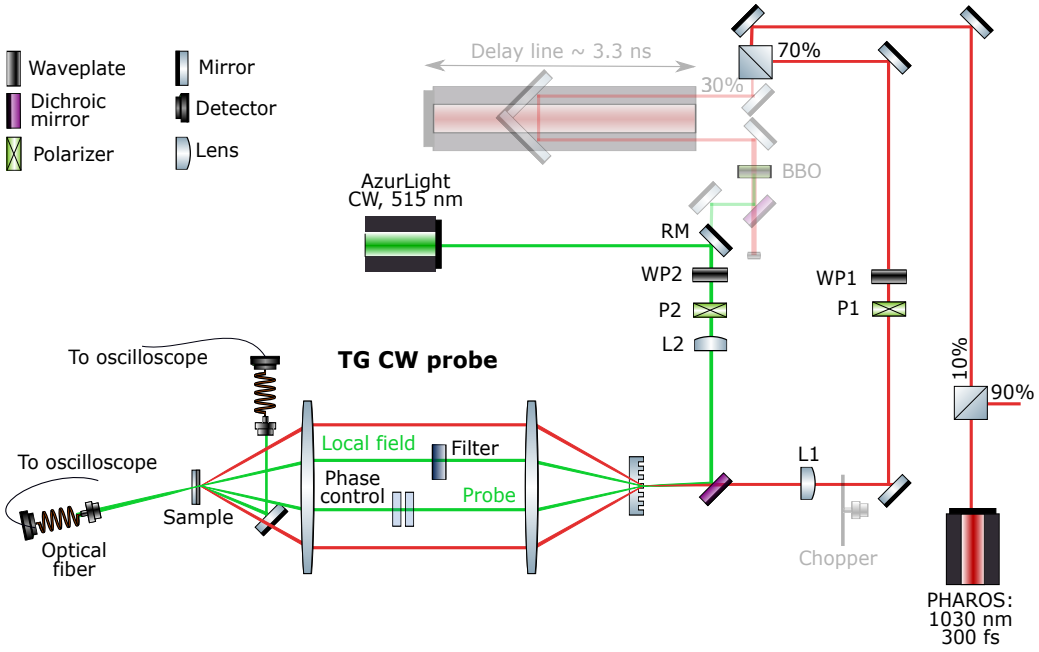

Figure 3.3: Sketch of the optical table for TG spectroscopy with CW at the NFFA-SPRINT lab. Components of the setup associated with other operational modes are displayed transparently.

3.2 Operational mode 2: TG spectroscopy with CW probe

Fig. 3.3 shows the setup used for TG spectroscopy with a CW probe and phase-stabilized heterodyne detection. This type of detection, commonly used in TG experiments, offers several advantages, such as signal amplification and the ability to detect the electric field of the TG signal rather than just its intensity[54, 55]. The upstream part of the setup is the same as the one described for operational Mode 1; the removable mirror (RM) allows to switch easily from Mode 1 to Mode 2. The source of the probe beam is an LS Azulight CW laser that emits at 515 nm, right at the same wavelength of the PHAROS second harmonic; this matching wavelength ensures reliable performance of the transmission optics, which is crucial especially to guarantee the correct spatial pump-probe overlap on the sample. In heterodyne detection, a *local field* (LF) is overlapped to the diffracted probe beam; the total measured intensity after sample can be therefore written as:

$$I_{\text{tot}} = |E_{\text{s}} + E_{\text{LF}} e^{i\phi}|^2 = I_{\text{s}} + I_{\text{L}} + 2E_{\text{s}}E_{\text{LF}} \cos\phi \tag{3.1}$$

where ϕ is the phase difference between the scattered and local field and E_{s} (I_{s}) and E_{LF} (I_{LF}) are the amplitude (intensity) of the scattered and local field, respectively. Typically $I_{\text{LF}} \gg I_{\text{s}}$. The third term in Eq. 3.1 is the signal of interest: the second term is constant and the first term is negligibly small. Furthermore, the information carried by E_{s} is proportional to E_{LF}, which in principle can be arbitrarily increased, within the practical limits imposed by the operational constraints of the CW laser. Eq. 3.1 shows that heterodyne detection preserves information about the phase of the diffracted probe beam and provides a linear response to the signal amplitude, which are normally lost in the con-

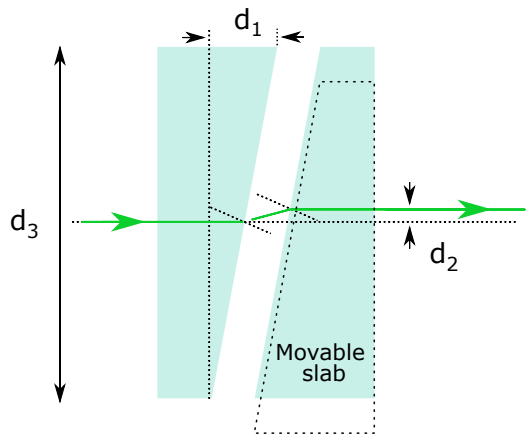

Figure 3.4: Phase control system of the reference field. By fabrication $d_1 = 28\,\mu m$ and $d_3 = 4$ cm. The slabs are placed at a distance of approximately 5 mm; in these conditions, we estimate a value of $d_2 \simeq 2\,\mu m$, which can be considered negligible compared to the laser footprint of 40 µm. The optical path of the reference beam, and consequently its phase, is controlled by vertically translating one of the two slabs.

ventional acquisition scheme. In addition to this, this procedure can help to overcome noise due to the detection electronics and, more importantly, to parasitically scattered light. The use of a phase mask in combination with a pair of doublets in confocal configuration is a convenient experimental arrangement that simplifies many practical issues [91]: i) the diffracted probe beam is automatically collinear with the LF assuring the coincidence of their phase fronts; this is implemented by design by using the $m = 1$ and $m = -1$ diffraction order of the second harmonic (515 nm) as probe beam and LF, respectively (see Fig. 3.3) ii) the relative phase stability between the diffracted and reference beams is automatically guaranteed by their generation from the same phase mask pattern. Furthermore, the phase difference can be controlled by adjusting the optical path length of the reference beam. Fine control of the phase is also necessary to isolate the last term of Eq. 3.1: by recording two signals with a relative phase difference of π the second term can be removed and further amplification of term containing the information about the diffracted field is finally achieved:

$$I^{HD} = I_{\text{tot}}^{\phi_0} - I_{\text{tot}}^{\phi_0+\pi} = 4E_{\text{s}}E_{\text{LF}} \tag{3.2}$$

To be noted that signal is still proportional to E_{s} rather than to its intensity.

In our setup we do not have control over the absolute phase values, but we can finely tune the relative phase difference ϕ by introducing tiny variations in the optical path of the local field through a pair of movable glass slabs placed in between the doublets. Fig. 3.4 shows a sketch of the custom-made glass slabs, specifically fabricated to minimize the vertical displacement of the local field. The filter is used to attenuate the local field to prevent detector saturation.

The signal superimposed to the local field is then focused into an optical fiber and it is measured by a high-speed detector (1544-B from Newport, 12 GHz bandwidth) connected to a digital oscilloscope (Lecroy, 4 GHz bandwidth). The acquisition chain limits

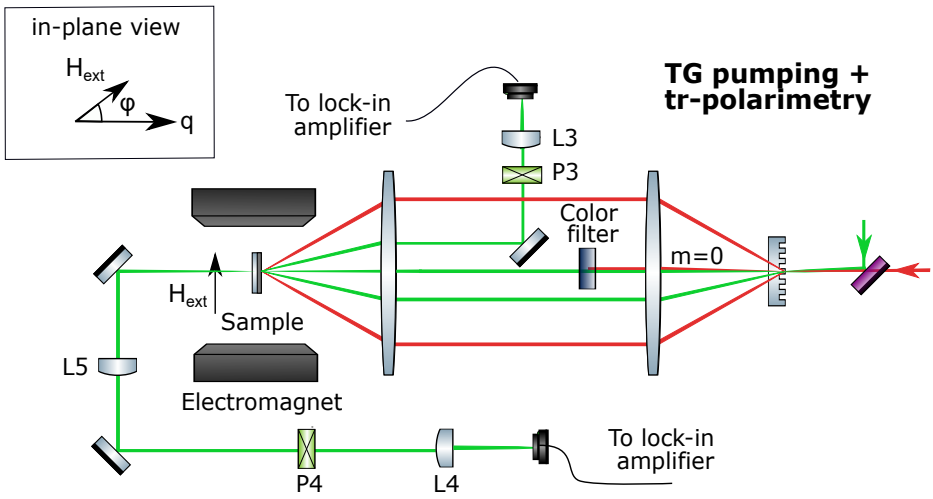

Figure 3.5: tr-MOKE and tr-Faraday endstation. The two first orders of the $1030\ \mathrm{nm}$ interfere on the sample generating the TG. The probe consists in the zero order of the $515\ \mathrm{nm}$ beam and a filter is needed to separate the two colors. The polarizers P3 is set close to extinction. The inset shows the in-plane orientation of the magnetic field with respect to the TG wavevector.

the fastest accessible dynamics to a fraction of ns. However, this detection scheme is suitable for investigating longer dynamics (up to microseconds), given that the time-delay window is set by the oscilloscope.

3.3 Operational mode 3: TG pumping with tr-polarimetry

This operational mode is a variant of Mode 1: the TG pumping is combined with tr-polarimetry, as sketched in Fig. 3.5. This is a suitable detection solution to study e.g. TG-mediated magnetoelastic coupling in the time domain. Here, we use the $m = 0$ and the $m = 1$ diffraction order of the 515-nm beam as probes for the tr-Faraday and tr-MOKE polarimetry, respectively. A color filter on $m = 0$ removes the fundamental at 1030 nm, which might induce additional dynamics on the sample and/or unwanted heating. Upon interaction with the sample magnetization, the probe changes its polarization state as a consequence of magneto-optical interaction, which is detected setting a polarizer - P3 and P4 in Fig. 3.5 for MOKE and Faraday effect, respectively - close to extinction. The signal acquisition chain (photoreceiver and lock-in amplifier) is the same as described in Sec. 3.1. When dealing with magnetoelastic coupling, a magnetic field is applied in the plane of the sample surface at an angle φ with respect to the TG-wavevector. Our home-built electromagnet can generate a maximum magnetic field of $100\ \mathrm{mT}$ at the sample position. The mounting of the electromagnet allows full in-plane azimuthal rotation and out-of-plane tilting and up to 20° off-normal.

It is worth mentioning that the setup can be employed for pump-probe experiments with a single pump by simply blocking one of the pump beams between the doublets. In this way, tr-transmittivity, tr-reflectivity, and tr-polarimetry can be performed at the same experimental TG endstation. The tr-MOKE experiments discussed in Ch. 6 have been performed in this configuration.

3.4 On the sample environment

Temperature and magnetic field are the two primary parameters that should be varied when studying the static and dynamic properties of magnetic samples. This applies to simple samples, such as ferromagnetic thin films, but especially to complex compounds that exhibit multiple magnetic phase transitions.

Fig. 3.6 shows a CAD drawing of the recently commissioned sample cooling setup, which consists of an ultra-high vacuum (UHV) vacuum chamber with a cryostat. The relative position of the chamber with respect to the laser beams can be adjusted by mechanical stages. The closed-cycle cryostat allows the sample to reach temperatures nominally down to 40 K. Higher temperature plateaus are achievable using a heater placed close to the sample. The sample is mounted on a cold finger in thermal contact with the cryostat, and its position within the chamber can be controlled by a hexapod located on top of the chamber. The sample temperature is monitored by a thermocouple placed on the sample holder near the sample.

The sample holder is specifically designed to fit in the air gap of a magnet that can produce magnetic fields up to 100 mT. However, the usual operating condition is limited to approximately 50 mT due to the lack of a cooling system for the magnet. The magnetic field can be applied both in the plane of the sample and with an out-of-plane angle of approximately 35° within the scattering plane.

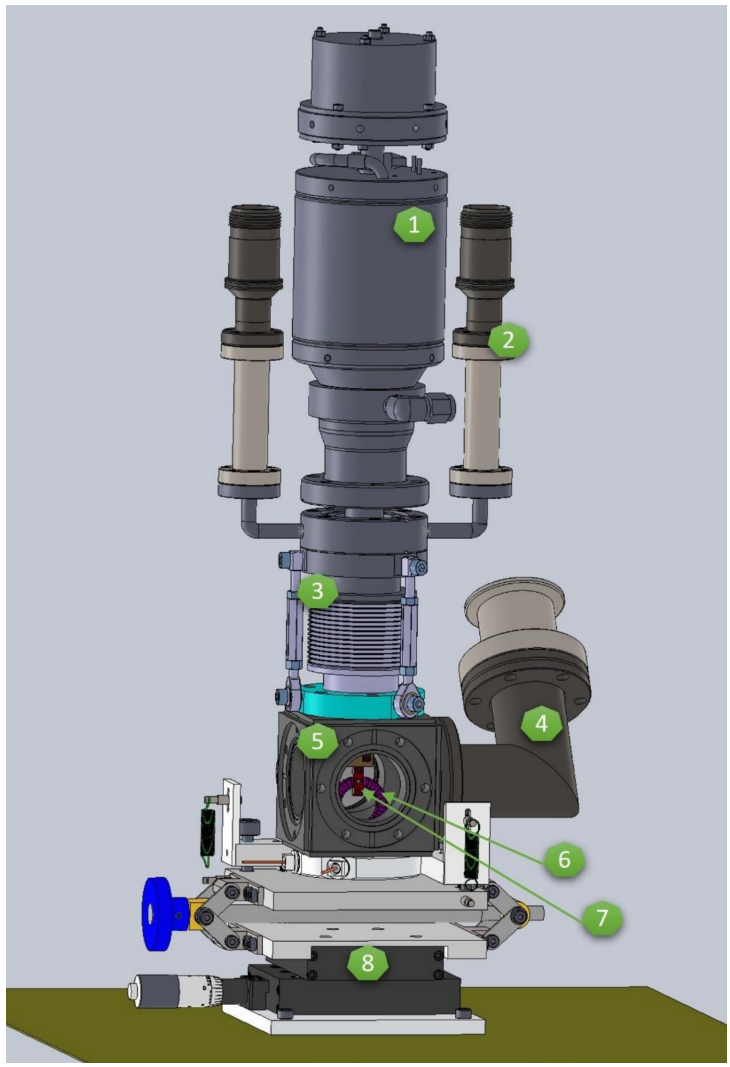

Figure 3.6: Image of the cooling system with numbered pins to highlight the key components: (1) the closed-circuit cryostat for cooling the sample, (2) the electrical feedthrough with 6 pins mounted on a DN16CF flange for heater power supply and temperature reading (3) a bellows on a DN40CF flange with 6 manually controllable degrees of freedom for sample manipulation (4) a flange for pumping (5) a vacuum chamber for housing the sample and the electromagnet (6) the electromagnet, (7) a sample holder, and (8) a mechanical base with five axes of movement (X, Y, Z, chi, and theta) for positioning the entire setup relative to the laser beam. Image courtesy of A. Fondacaro.

CHAPTER 4

Acoustics and magnetoacustics

Achieving full control over the spin degree of freedom for memory storage and logic computation is a key objective in the fields of spintronics and magnonics [92, 93]. Theoretical and experimental investigation of the potential of SWs for their integration into next-generation devices operating at higher frequencies is a very active research field, particularly in the THz range [94]. SWs are attractive because of their potential for energy-efficient devices, as they avoid Joule dissipation. However, efficiently generating magnons in magnetic materials and controlling their properties remain a significant challenge. One promising strategy involves relying on MEC. SAWs in the gigahertz frequency range and micron-scale wavelengths are particularly suitable because the dispersion of SWs can easily be tuned to be degenerate with that of SAWs, allowing for enhanced magnetoelastic coupling. Experimentally, SAW-driven SW have been observed to be more efficiently generated and have longer lifetimes, offering a viable pathway to energy-efficient magnonic devices [7]. Furthermore, starting from simple systems, an infinite number of possibilities arise considering the huge progress made in the last few decades in engineering materials with promising properties and functionalities.

IDTs on piezoelectric substrates have proven to provide an efficient approach to acoustically generate SWs via inverse magnetostriction in magnetic thin films [18]: the elastic deformation caused by the rf SAWs effectively replaces the traditionally employed rf EM field, allowing for the realization of SAW-FMR. However, this method has certain limitations, such as restricted flexibility in the range of accessible frequencies due to the fixed design of the transducers and the requirement for contact-based operation, which necessitates advanced lithography facilities. About a decade ago, a novel all-optical approach based on the TG technique was proposed and tested [19]. Those groundbreaking experiments paved the way for a wide range of new applications and opportunities in the use of TG spectroscopy for studying magnetic excitations without the limitations implied by nanofabrication.

In this chapter, we discuss our experimental results obtained on polycrystalline Ni films. We report a complete set of measurements using all the operational modes of the experimental setup discussed in Ch. 3 to investigate both acoustic and magnetic dynamics. In particular, TG pumping in combination with tr-polarimetry is used to investigate acoustically driven magnetic dynamics, following the approach of Ref. [19] and confirming their observations. Furthermore, we provide additional insights into the acoustically driven dynamics by comparing results obtained from SAW-driven SW resonance with standard broadband FMR, which allowed us to quantify fundamental magnetic properties of our samples, such as effective magnetization and Gilbert damping.

4.1 Sample details

We investigate polycrystalline Ni thin films grown on amorphous and crystalline substrates. Firstly, we will discuss the measurements carried out on a SiO_2(10nm)/Ni(40nm) /SiO_2 sample for each of the operational modes described in Ch. 3, providing an acoustic characterization and analyzing the observed acoustically driven magnetic dynamics phenomena. Secondly, we will discuss the comparison between SAW-driven SW resonance and Broadband FMR (B-FMR) on a similar sample grown on a (001)-oriented crystalline CaF_2 substrate, namely SiO_2(10nm)/Ni(14nm)/CaF_2(001). In both cases, the 10-nm-thick capping overlayer of SiO_2 is to prevent oxidation and still guarantee a good optical transmission of the laser beams.

The samples were fabricated by e-beam evaporation at the CNR-IOM clean room facility in Trieste, Italy. Details on the growth are omitted here for brevity and presented in App. A. The decision to fabricate Ni, rather than another ferromagnetic material, is based on two considerations: i) Ni is frequently the material of choice for studying magnetoelastic dynamics due to its high saturation magnetostriction coefficient ($\lambda_s = -38 \cdot 10^{-6}$ for a polycrystalline thin film [28]); ii) the Curie temperature of Ni ($T_c = 628$ K [3]) is low enough to provide good magneto-optical contrast (see Sec. 4.3). As for the substrates, we choose the amorphous SiO_2 for direct comparison with Ref. [19]; however, the low structural quality induced by the growth process prevented us from comparing the results obtained on this sample with the B-FMR measurements. Therefore, for the second sample, we choose crystalline CaF_2(001) for two main reasons: (i) to improve the structural quality of the film, thereby enhancing the B-FMR signal - which can be affected by the substrate [95] - and (ii) to ensure good thermo-elastic efficiency combined with low thermal conductivity, allowing for a long-lasting TG-induced spatial temperature profile $T(x)$ and providing improved magneto-optical contrast with respect to the Ni film grown on amorphous SiO_2, as it will be discussed in Sec. 4.3. The simple model developed to evaluate this second aspect is described in App. A. The influence of the substrates on the growth process is evaluated by comparing structural data obtained by Grazing Incidence X-Ray Diffraction (GIXRD) and X-Ray Reflectivity (XRR) in collaboration with CNR-IMM and Università degli Studi di Milano-Bicocca. These measurements were performed on both a SiO_2(10nm)/Ni(14nm)/CaF_2(001) sample and a SiO_2(10nm)/Ni(14nm)/SiO_2 sample. The results, presented in App. A, indicate an overall lower structural quality for the film grown on amorphous SiO_2. The absence of a clear B-FMR signal in samples grown on amorphous SiO_2 suggests that this result is related to the crystallinity of the substrate rather than to the film thickness, which suggests that we can extend the results obtained on SiO_2(10nm)/Ni(14nm)/SiO_2 to the SiO_2(10nm)/Ni(40nm)/SiO_2 case.

We characterized magnetically all samples by longitudinal MOKE measurements performed at the NFFA-APE beamline at the Elettra Synchrotron facility [83]. The hysteresis loops are reported in App. A. Both samples show low coercive (< 2 mT) and saturation fields (< 3 mT); since all the magnetic measurements presented in this chapter were performed at much higher fields, the samples can be considered magnetically saturated. This point will be further discussed in Sec. 4.3.

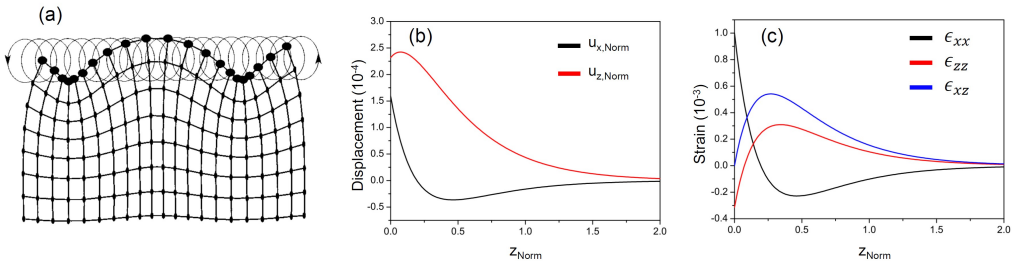

Figure 4.1: (a) Schematic representation of strain and particle displacement for a RSAW, adapted from [97]. (b) Displacement and (c) strain in soda-lime glass as functions of the depth into the bulk. All quantities are normalized by dividing by the RSAW wavelength Λ. Adapted from [38].

4.2 Experimental results: acoustics

As already mentioned in Sec. 2.2.6, standing acoustic waves are excited upon the interference of the two pump beams via impulsive thermoelastic expansion. Before presenting the experimental results, we provide an overview of the expected active modes for the case of interest, based on phenomenological considerations and existing literature [18, 19, 54, 96, 97].

4.2.1 What is expected?

The first expected mode is the RSAW. It is a surface acoustic mode that arises as a mathematical solution for the normal modes propagating in a semi-infinite medium, and originates from the boundary conditions imposed on the free surface. If we consider the plane (x, y) as the free surface of our sample, it follows that the (x, z) is the so-called *sagittal plane*. The elastic energy is confined to the surface, implying that the displacement u is restricted to the surface: its amplitude decreases exponentially along z, namely $u_x(z) \propto e^{-\gamma_u |z|}$. The decay length is approximately equal to the wavelength: $1/\gamma_u \approx \Lambda$. Furthermore, u_x and u_z oscillate simultaneously, leading to a mixed polarization state, partially longitudinal and partially transverse along z. The two components are $\pi/2$ out of phase: the resulting motion is elliptical and limited to the sagittal plane, as shown in Fig. 4.1.a-b. In terms of strain, the only non-zero components are ϵ_{xx}, ϵ_{zz}, and ϵ_{zx}. The main component is ϵ_{xx}, at least close to the surface (see Fig. 4.1.c); this is of relevance for the modeling of magneto-elastic coupling involving RSAW, as discussed in Sec. 1.4.1. Finally, it can be demonstrated that the velocity of RSAW is lower than that of any other bulk waves [97, 98].

When considering thin films on a substrate, the active acoustic modes become more numerous and complex, influenced by the film thickness, the wavelength of the acoustic wave, and the degree to which the film is "bound" to the substrate [54]. Typically, the film acts as a waveguide being able to support a new zoo of surface acoustic waves - e.g. such as Sezawa modes, Love modes, Lamb modes - whose properties depend mainly on the product hk, where h is the film thickness and k the wavevector of the acoustic waves. It follows that in our experimental case of $\Lambda = 2\pi/k \gg h$, the elastic energy is mainly concentrated in the substrate, which dominates the dynamics: the thin film on top acts as a negligible perturbation on the overall dynamics. Therefore, the expected RSAW is that of the substrate. More detailed calculations bring to the same conclusion, showing

that for $hk \to 0$ the lowest-energy mode supported by the film is indeed the RSAW of the substrate [54].

The second expected mode is the SSLW. This type of surface wave is also widely observed in devices where acoustic waves are excited using IDTs on a piezoelectric substrate[37, 99–101] and references therein. Intuitively, the SSLW can be understood as a (longitudinal) bulk wave generated by a longitudinal perturbation of the surface, which then quickly propagates deeper into the substrate (i.e., *leaking*) at a small angle relative to the substrate surface. More rigorously, it has been shown [54] that as $hk \to 0$ the other normal modes of the film become *leaky*, rapidly radiating away from the surface by coupling with bulk modes that share similar characteristics (polarization, frequency, dispersion, etc.), making them practically indistinguishable.

Therefore, the role of the film in the acoustic dynamics is merely to ensure better absorption of the incident pump beams, as also verified by power measurements of the transmitted and reflected probe which confirmed a $\simeq 34\%$ (few percentages) absorption with (without) the film on top. To sum up, the Ni thin film strongly absorbs the pump energy building up a surface temperature grating that over time diffuses into the substrate, heating a considerable portion of the substrate. The resulting acoustic dynamics are then completely determined by the properties of the substrate: the same acoustic modes could have been observed by replacing the Ni with any other thin film strongly absorbing at 1030 nm (see also Ch. 5). However, Ni is a good option to investigate magnetoelastic dynamics.

4.2.2 What is observed?

The acoustic characterization of the sample is performed via TG spectroscopy with pulsed and CW probes, in both transmission and reflection geometries. This approach is used mainly to demonstrate the functionality and potential of operational modes 1 and 2, as the observed phenomenology is consistent across both. All the measurements presented in this section are performed in air and at room temperature on the SiO_2(10nm)/Ni(40nm) /SiO_2 sample.

The TG signals in both reflection and transmission geometries is shown in Fig. 4.2.a-b (Fig. 4.3.a-b) for the pulsed (CW) probe configuration. Regardless of the type of probe, the reflection channel shows low-frequency oscillations with minimal attenuation. In contrast, the transmission channel shows high-frequency, low-amplitude oscillations with significant attenuation at time delays $>$ ns. These differences are understood to arise from the differing sensitivities of the two detection channels. In the reflection diffraction case, light is diffracted due to periodic variations imposed by surface deformation, making it less sensitive to the photoelastic effect.[1]

Furthermore, RSAW typically have large surface displacements, resulting in large diffraction efficiency. Conversely, the transmission geometry is more sensitive to variations arising from photoelastic effects generated in the substrate, which is why we observe the *bulky* SSLW in this configuration. Furthermore, the probe beam travels through the Ni/SiO_2 heterostructure significantly longer than the probe wavelength, and it gets attenuated significantly more than in reflection geometry. This is also theoretically predicted by scattering efficiency calculations [102, 103]. The different sensitivity to the acoustic dynamics of the reflection and transmission channels is also visible in the Fast

[1] The photoelastic effect is defined as the change of refractive index caused by SAW-induced stress.

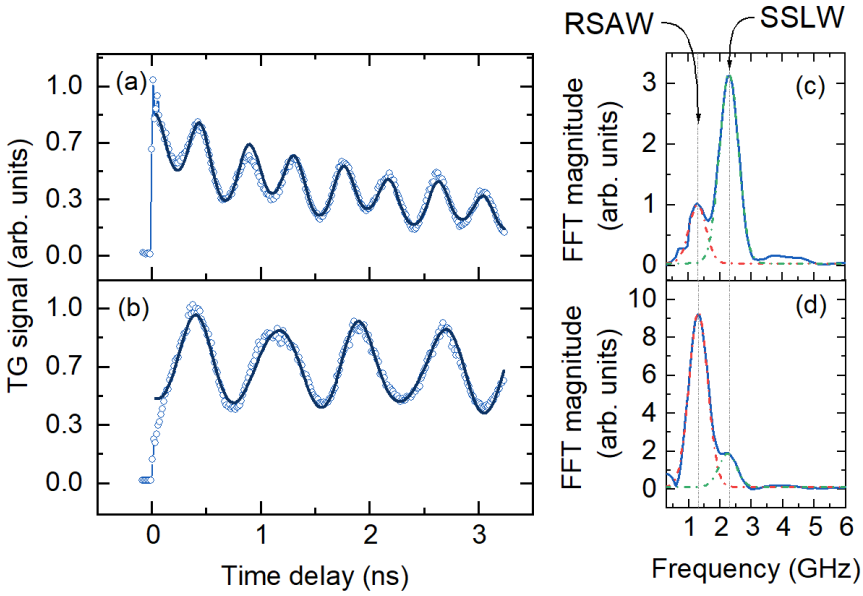

Figure 4.2: TG signal with the pulsed probe (a) in transmission geometry and (b) in reflection geometry, with the corresponding FFT magnitudes shown in (c) and (d), respectively. FFT is computed with zero-filling and apodization with a Hamming window. Solid lines in panels (a)-(b) are the best fit using Eq. 4.1. For all measurements: i) the pitch of the TG is $\Lambda = 2.54$ µm ii) the incident pump and probe fluence are set at 10 and 0.2 mJ/cm^2, respectively. In panels (c)-(d) The gray reference lines at 1.3 and 2.3 GHz indicate the positions of the FFT peaks, corresponding to the RSAW and SSLW, respectively. The dash-dot lines are the best fit using a Gaussian lineshape to the RSAW (in red) and SSLW peaks (in green).

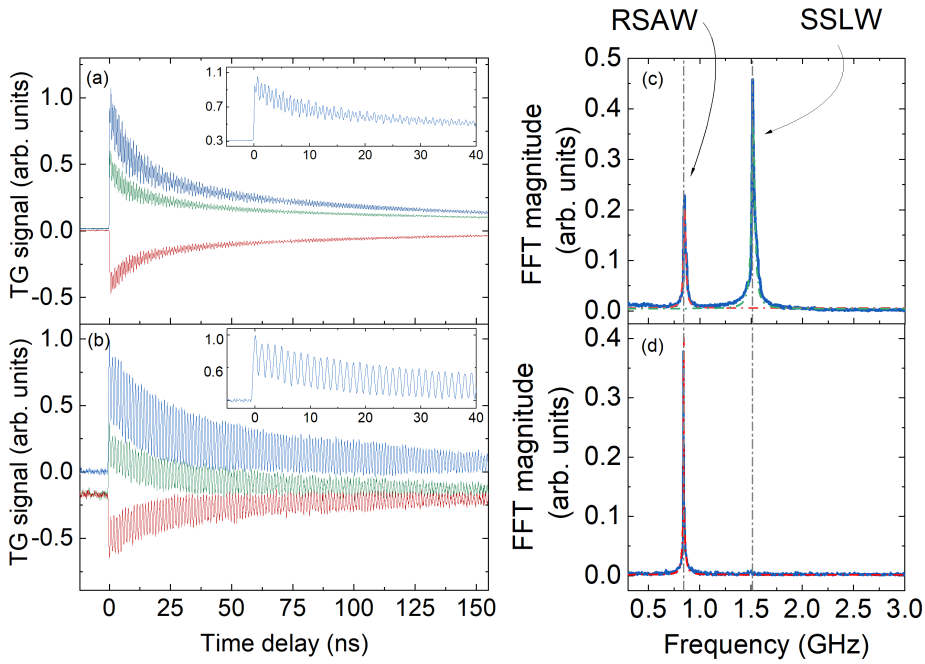

Figure 4.3: TG signal acquired with hetereodyne detection (a) in transmission and (b) in reflection geometry. The signals in green and red are acquired with a relative phase difference of π, as it can also be seen by the opposite phase of the signal, which is proportional to the scattered field. The blue trace represents the difference between the two, which is amplified in amplitude. The insets show the heterodyne signals in the first 40 ns. (c)-(d) FFT magnitude of the tr-traces in transmission and reflection, respectively, fitted by Lorentzian lineshapes. The SSLW is not visible in reflection. For all measurements: i) the TG pitch is Λ =4.00 µm ii) the pump fluence is set at 10 mJ/cm^2 and the incident probe power at 190 mW.

Fourier Transform (FFT) magnitude of the signals reported in Fig. 4.2.c-d and Fig. 4.3.c-d, which give the spectral density of the time-resolved traces.

The frequency values can be determined from the FFT peaks, and the corresponding errors can be estimated from their Half Width Half Maximum (HWHM) obtained by fitting the peaks with either a Gaussian or Lorentzian lineshape, depending on the sampled time-delay window. For a damped oscillating signal, if sampled properly over a time interval that captures its entire evolution, the FFT mathematically produces a Lorentzian lineshape. The HWHM of this Lorentzian is directly related to the damping of the oscillations. This Lorentzian profile is typically observed in heterodyne detection, where the acquisition window spans hundreds of ns. However, when the sampling window is reduced to just a few ns, as in the case of a pulsed probe, the FFT peaks of the observed frequencies exhibit broadening, necessitating the use of a Gaussian lineshape fitting rather than a Lorentzian one. In such cases, the broadening of the lineshape is no longer a reliable measure of damping, and using the HWHM as an error estimate for the frequencies can lead to overestimation. The HWHM of the peaks reported in Fig. 4.2.c-d is $\simeq 0.3$ GHz, meaning an error of $\simeq 20\%$ for the observed frequencies. To get a better estimation of the errorbar for the pulsed probe configuration, it is possible to fit the TG signal at positive time delays with [50]

$$\mathcal{S}(t>0) = \left[a_0 e^{-\frac{t}{\tau}} + \sum_i a_i e^{-\frac{t}{\tau_i}} \sin(2\pi f_i + \phi_i)\right]^2 + C \tag{4.1}$$

which describes well the intensity of the diffracted probe beam in the case of cohexistence of a quasi-stationary temperature grating with a TG-induced coherent acoustic dynamics, as discussed in Sec. 2.2. Here, the first exponential term describes the thermal relaxation, the second one the excited SAWs modes and the C constant accounts for the background signal due to parasitically scattered light.

Since the time-domain data in Fig. 4.2.a-b do not show significant damping, attenuation of the acoustic modes is omitted in the fitting function. The best fit to the data are reported as solid lines; the obtained errors on mode frequencies are reduced to a few $\%$. Conversely, for the CW probe case, we get from the Lorentzian fit an HWHM of $\simeq 0.01$, corresponding already to an error of the order of 1%; for this reason, fitting in the time domain is omitted for this operational mode. Tab. 4.1 lists the frequencies of each mode/geometry and operational mode, along with their corresponding errors. The corresponding sound velocities are also reported, with the errors obtained by propagating the frequency errors while assuming zero error in the TG pitch Λ, or equivalently, the wavelength of the acoustic wave. The obtained values are reasonably compatible with the calculated errors. It is worth mentioning that the frequencies for the data acquired with CW are significantly lower because performed at a larger TG pitch on the sample.

In summary, the pulsed and CW operational modes are complementary, and when combined, they allow for a comprehensive study of acoustic dynamics over a broad time window. In this specific case, the TG-induced acoustic dynamics can be effectively measured on both timescales. However, in some instances, the acoustic dynamics evolve on a sub-nanosecond timescale necessitating a stroboscopic approach, as can for example happen for multilayered samples [104]. When using the pulsed probe configuration to investigate other TG-induced phenomena - such as magnetic excitations - acoustic characterization on short timescales can be valuable in confirming the absence of magnetoelastic coupling with the magnetization dynamics - as it will be discussed in Ch. 5 - or spurious effect coming from a non-perfect polarization analysis. In contrast, the

Table 4.1: Frequency and sound velocity of the RSAW and SSLW. The error reported on the frequencies are extracted from the time-domain fit in the pulsed case, and from the FFT HWHM fit for the CW configuration. Sound velocities are calculated as $c = \Lambda f$, and the corresponding errors are obtained via error propagation.

	f_{RSAW} (GHz)	f_{SSLW} (GHz)	c_{RSAW} (km/s)	c_{SSLW} (km/s)
Pulsed, Trans.	1.29 ± 0.1	2.30 ± 0.04	3.2 ± 0.3	5.7 ± 0.1
Pulsed, Refl.	1.31 ± 0.05	2.25 ± 0.08	3.20 ± 0.1	5.6 ± 0.2
Continuous, Trans.	0.85 ± 0.01	1.52 ± 0.02	3.40 ± 0.04	6.1 ± 0.1
Continuous, Refl.	0.84 ± 0.01	—	3.36 ± 0.04	—

CW probe, with its extended time windows, is particularly well suited to investigate phenomena such as thermal diffusion [105]. Here, the discussion is limited to the frequency of the acoustic modes, which is the key parameter for the discussion concerning magnetoelastic coupling in our samples.

4.3 Experimental results: magnetoacoustics

In a magnetostrictive medium, SAWs can drive, via inverse magnetostriction, SWs with matching wavelength and frequency [32, 106]. The measurements presented in this section are acquired by exploiting TG-pumping to excite SAWs and tr-Faraday polarimetry to probe the SWs (see Sec. Fig.3.5). Firstly we will examine the main magnetoelastic features on the SiO_2(10nm)/Ni(40nm)/SiO_2 sample, while we will refer to the SiO_2(10nm)/Ni(14nm)/CaF_2 one for the comparison with B-FMR.

4.3.1 Experimental considerations on magneto-optical sensitivity

As mentioned above, the laser footprint (FWHM) on sample is approximately 40 μm for the pump and about 25 μm for the probe. Therefore the probe footprint is much larger than the TG pitch Λ. This is desirable in the case of acoustic measurements, where diffraction efficiently takes place if a considerable number of fringes fit in the probe footprint. However, this is not the case for magnetic measurements. For magneto-optical measurements, this is in general a problem. At any given time t at positive delays, the dynamic component of the spin wave can be written as $M_z(x,t) = A\cos(qx+\phi)e^{-i\omega t}$, where A is the wave amplitude, ϕ is the appropriate spatial phase, and ω is the angular frequency. The spatial average of this expression is expected to be exactly zero, resulting in no Faraday rotation being observed at any time. However, when the TG pumping scheme is applied, the amplitude distribution of the SWs becomes linked to the periodic TG temperature profile $T(x)$. Consequently, the local saturation magnetization $M_{\mathrm{s}}(x)$ is not uniform along the wavevector q and decreases at the $T(x)$ peaks. To a first approximation, this relationship can be described by $M_{\mathrm{s}}(T(x))$, meaning that locally M_{s} follows the $M(T)$ equilibrium curve, as schematically shown in 4.4.a. It follows that amplitude of the SW is affected by the local temperature at position x, so $M_z(x) = \tilde{A}\cos(qx+\phi)$ is a good approximation, where $\tilde{A} = A\frac{M_{\mathrm{s}}(T(x))}{M_{\mathrm{s}}(0)}$. Considering this thermal modulation, the

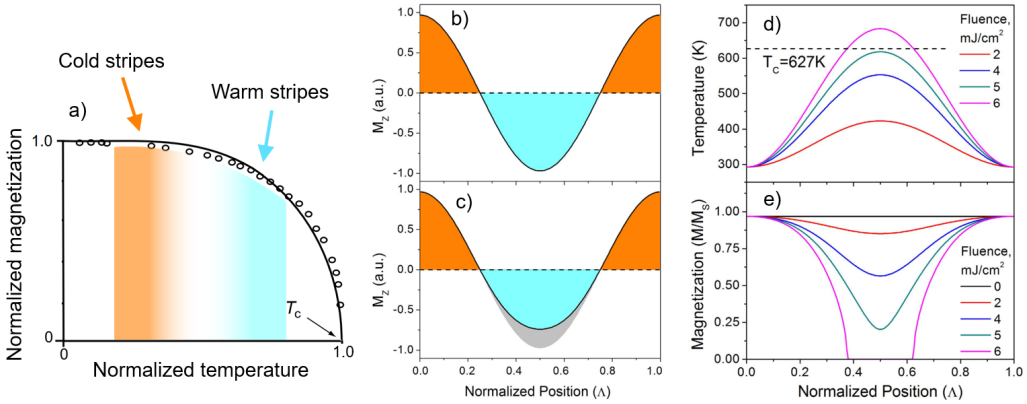

Figure 4.4: (a) Trend of the M_s for Ni as a function of normalized temperature T/T_c ($T_c = 628$ K). Regions where the pumps interfere destructively are at lower temperature (shaded in orange), while where they interfere constructively are warmer (shaded in light blue); therefore, they exhibit a difference in M_s values. Adapted from Ref. [107]. (b-c) Spatial distribution of dynamic magnetization M_z across an entire SW wavelength at a specific time is shown. The color shading indicates regions contributing positively (orange) or negatively (light blue) to Eq. 4.2. In the absence of temperature modulation [panel (b)], the positive and negative contributions balance each other; with finite temperature modulation [panel (c)], the contribution from the warmer regions (which give a negative contribution to Eq.4.2) is partially reduced. Adapted from Ref. [19]. (d-e) Spatial distribution of the local temperature $T(x)$ [panel (d)] and magnetization [panel (e)] along a full SW wavelength, derived from finite-element COMSOL simulations under varying pump fluence conditions. Adapted from Ref. [19].

spatial integral along one TG period can be written as

$$\langle M_z(t)\rangle_\Lambda = e^{-i\omega t}\int_0^\Lambda dx\, A\frac{M_s(T(x))}{M_s(0)}\cos(qx+\phi) \neq 0, \tag{4.2}$$

which is not zero-averaged. Therefore, the Faraday rotation of the transmitted beam is proportional to this integral. Detailed investigations and modeling of this phenomenon are discussed in Ref. [19]. With the use of finite-element calculations (COMSOL Multiphysics), the authors simulated different pump fluences, taking into account the local temperature $T(x)$ and the local magnetization $\frac{M_s(T(x))}{M_s(0)}$; the main results are depicted in Fig.4.4.d-e. It becomes evident why the T_c of the magnetic thin film is a crucial parameter for magneto-optical sensitivity. A low T_c leads to complete demagnetization of the film, reducing the magneto-optical contrast, whereas a high T_c results in insufficient modulation of $M_s(T)$, also lowering the magneto-optical contrast. It's important to note that the spatial modulation of M_s depends on the time elapsed after the pump trigger, due to the thermal relaxation in the film: as time progresses, Eq. 4.2 approaches zero, making the magnetic dynamics undetectable.

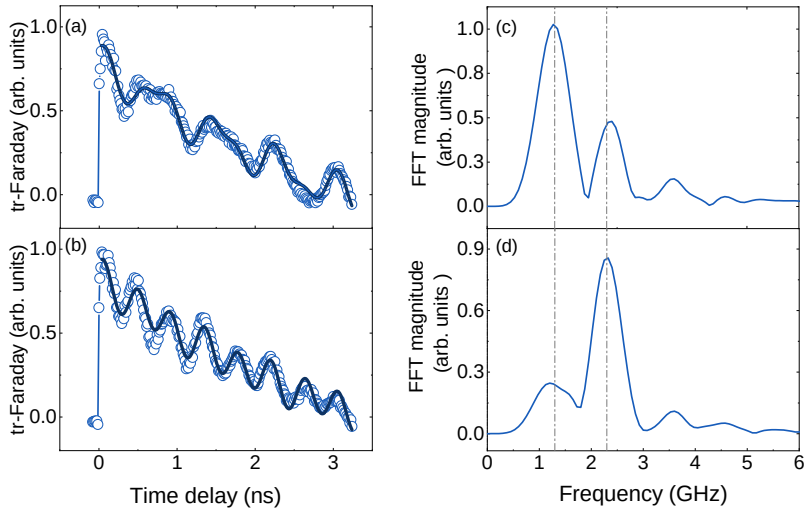

Figure 4.5: (a-b) Raw tr-Faraday signals at (a) 12.3 mT and (b) 25.8 mT. The solid lines are best fit to the data using Eq. 4.3. (c-d) FFT of the time domain traces after exponential background subtraction.

4.3.2 SAW-pumped dynamics

In Sec. 1.4.1 we have derived the expression for the MEC torque in the case of dominant longitudinal strain ϵ_{xx} as $\tau_{MEC} \propto \sin(2\phi_0)$, where ϕ_0 is the angle at equilibrium of the magnetization with respect to the TG wavevector $\mathbf{q}$. Therefore, to maximize MEC and consequently the SAW-driven dynamics, an IP magnetic field is needed to align $\mathbf{M}$ at an angle ϕ_0 with respect to $\mathbf{q}$ [18]. However, it has been shown [36] that in a sample with modulated magnetostatic properties - such as the thin film heated by the stripe - the MEC reaches a peak around $20°$ and is suppressed at $45°$. For the following measurements, we set the external magnet at an angle of approximately $\phi_0 \simeq 15°$. All measurements discussed in this chapter were conducted in air at room temperature, with the incident pump and probe fluences set at 10 mJ/cm^2 and 0.4 mJ/cm^2, respectively.

The TG-pumped tr-Faraday traces are presented in Fig. 4.5, with the TG pitch on the sample fixed at $\Lambda = 2.54\,\mu\mathrm{m}$. The raw data are shown for two values of the external applied magnetic field $B_{\mathrm{ext}} = \mu_0 H_{\mathrm{ext}}$, specifically $B_{\mathrm{ext}} = 12.3$ mT and $B_{\mathrm{ext}} = 25.8$ mT. As it will be further discussed below, at these values of B_{ext}, the magnetic dynamics resonate with RSAW and SSLW, respectively, resulting in the observation of large precessional dynamics.

The solid line represents the best fit to data obtained by fitting with an exponential combined with two sine functions, namely

$$\mathcal{S}(t>0) = a_0 e^{-t/\tau} + \sum_i a_i e^{-\frac{t}{\tau_i}} \sin(2\pi f_i + \phi_i) + C \tag{4.3}$$

to account for both coherent - SAW-puped magnons - and incoherent contribution - slow remagnetization caused by thermal diffusion of the deposited energy into the non-magnetic layers and the substrate.

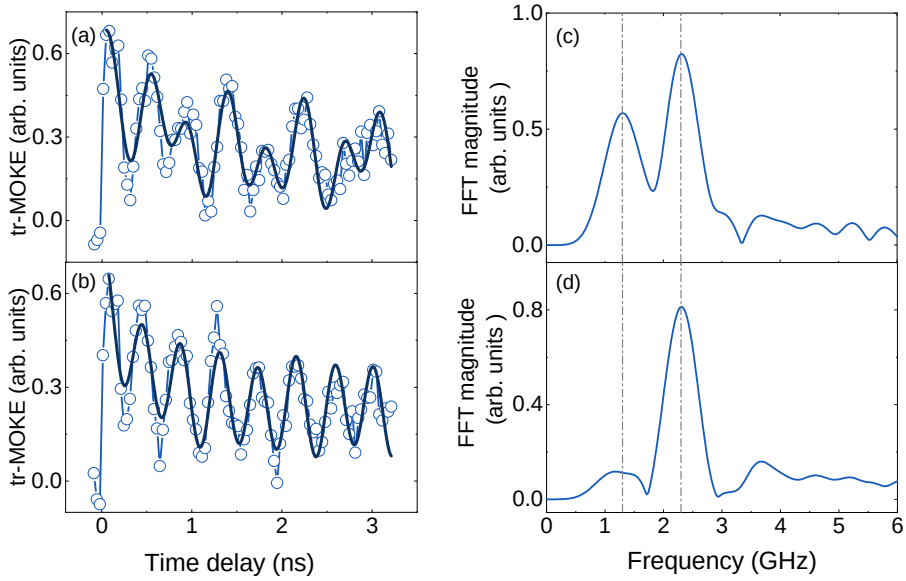

Figure 4.6: (a-b) Raw tr-MOKE signals at (a) 16.2 mT and (b) 25.8 mT. The solid lines are best fit to the data using Eq. 4.3. (c-d) FFT of the time domain traces after exponential background subtraction.

Table 4.2: Frequency of the two magnetic modes observed via tr-Faraday and tr-MOKE polarimetry at different magnetic fields.

	B_{ext} (mT)	f_1 (GHz)	f_2 (GHz)
tr-Faraday	12.3	1.31 ± 0.06	2.36 ± 0.01
tr-Faraday	25.8	1.39 ± 0.04	2.33 ± 0.02
tr-MOKE	16.25	1.31 ± 0.02	2.32 ± 0.01
tr-MOKE	25.8	1.35 ± 0.04	2.33 ± 0.02

Fig. 4.6 shows the same type of measurements but in reflection geometry for $B_{\text{ext}} = 16.2$ mT and $B_{\text{ext}} = 25.8$ mT. The lower signal level with respect to tr-Faraday can be attributed to off-normal incidence of the probe beam ($\simeq 6°$). The frequencies of the tr-Faraday and tr-MOKE signals are summarized in Tab. 4.2, and their values provide evidence of the acoustic pumping: in all configurations of geometry or magnetic field, the frequencies of the modes match either the RSAW or SSLW frequency found in the acoustic characterization. Fig.4.5.c-d and Fig.4.6.c-d present the FFT of the data after exponential background removal. Once again, they offer a great graphical insight into the contribution of each surface acoustic wave to the overall magnetic dynamics. At low magnetic fields - e.g. 12.3 mT - the magnetic dynamics is primarily driven by the RSAW, while at higher fields - e.g. 25.8 mT - the dynamics is predominantly influenced by the SSLW.

The frequency dependence of the tr-Faraday traces on B_{ext} is systematically examined to have a more complete picture of this phenomenology. Fig. 4.7.a, shows a two-dimensional map of the tr-Faraday signal after exponential background subtraction, plotted against the pump-probe time delay Δt and the external magnetic field B_{ext}. The

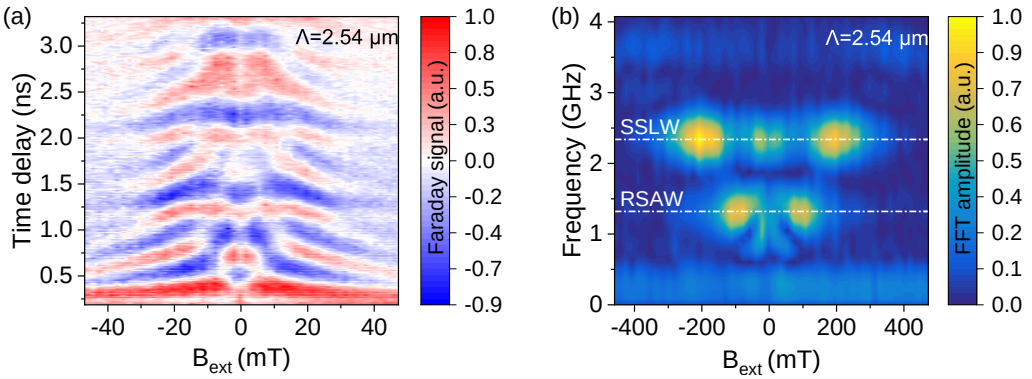

Figure 4.7: (a) Time-domain and (b) frequency-domain maps of tr-Faraday obtained on SiO_2(10nm)/Ni(40nm)/SiO_2 for a TG pitch of $\Lambda = 2.54$ µm. The magnetic field is swept from positive to negative values. In panel (b) the horizontal dashed lines highlight the frequency of the TG-pumped RSAW and SSLW.

magnetic field is swept from positive to negative values in $\simeq 2$ mT steps. It is noteworthy that these field steps are similar to the coercivity of the sample; therefore, due to coarse sampling, magnetization reversal phenomena are not visible in our measurements. An FFT is performed for each trace after exponential background subtraction, to emphasize the presence of resonance behavior; the resulting two-dimensional map is shown in Fig. 4.7.b. The spectral weight is concentrated in specific regions of frequency and magnetic field. By overlaying the frequencies of the TG-pumped SAWs onto the map, a clear correlation is observed. According to previous studies [19, 33], the interpretation is that the enhancement of spectral weight indicates large SAW-driven precessional dynamics, which occur when the spin wave dispersion matches either f_{RSAW} or f_{SSLW}. It is important to note that for any given value of B_{ext}, both SAWs are involved in the acoustically-driven magnetization dynamics via inverse magnetostriction; however, outside resonance the signal is too low to be detected. Fig. 4.8 shows similar maps are obtained using TG pitches of $\Lambda = 3.07$ µm and $\Lambda = 4.00$ µm; the one obtained with the TG pitch of $\Lambda = 2.54$ µm is reported again for easier comparison. Changing Λ leads to a corresponding shift in the RSAW and SSLW frequencies, following the linear dispersion relation of acoustic modes. It follows that, by choosing an appropriate TG pitch, the SAW-FMR resonances can to be tuned to the desired frequency and/or magnetic field. In Fig. 4.8.b-c some additional peaks are observed at frequencies RSAW+SSLW; these effects are due to excitation of higher-order resonances due to parametric pumping. The appearance of parametric resonances testifies that large-amplitude magnetization precession is excited by the proposed TG-pumping scheme. The interested reader can find additional information about parametric resonance in TG-pumped magnetization dynamics in Ref. [20, 108].

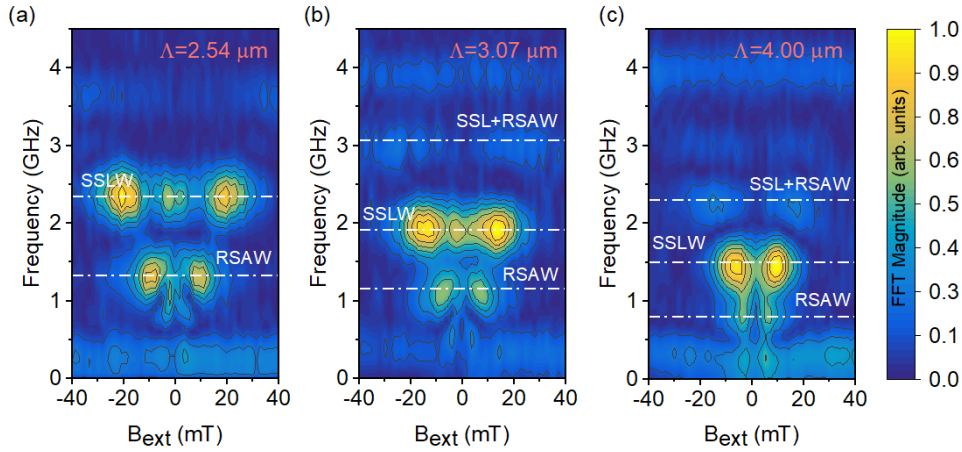

Figure 4.8: Frequency-domain maps of tr-Faraday obtained on SiO_2(10nm)/Ni(40nm)/SiO_2 for TG pitches of (a) $\Lambda = 2.54$ µm (b) $\Lambda = 3.07$ µm and c) $\Lambda = 4.00$ µm. Reference lines mark the frequencies of RSAW and SSLW found in the acoustic characterization; reference lines at SSLW+RSAW are guide to eye for parametric resonances.

4.3.3 Comparison with broadband FMR

By using optical pumping in the TG excitation mechanism, it is possible to access wavevectors in the μm^{-1} range. If the SW dispersion of the sample being studied is relatively flat within this wavevector range, the acoustically-driven SW resonance - though theoretically distinct - can effectively be treated as acoustically-driven FMR (SAW-FMR). Since this holds true for Ni, we quantitatively compare TG-driven SAW-FMR with "standard" broadband FMR (B-FMR). The sketches in Fig. 4.9 provides insights into the technical similarities and distinctions between B-FMR and TG-pumped SAW-FMR. In both methods, the static magnetic field B_{ext} is assumed to be uniform and, in combination with the magnetic shape anisotropy, defines the equilibrium direction of the magnetization. In B-FMR, the oscillating magnetic field is generated by an rf current within a metallic waveguide. This setup ensures that the oscillating field B_{rf} is perpendicular to B_{ext}, thereby maximizing the torque on the magnetic dipoles. The magnetic moments precess in-phase throughout the entire sample. In contrast, in SAW-FMR, the rf field is generated by the effective MEC field, which arises from the SAW strain. A significant torque requires a non-zero angle between B_{ext} and the wavevector q (see Sec. 1.4.1). The finite wavelength of the rf field results in magnetization precession with a spatially modulated phase, namely a SW, and large precessional dynamics is observed when the intensity of B_{ext} causes the SW dispersion to be generate with that of the SAWs.

The B-FMR measurements were performed using a custom-built setup available at the Università degli Studi di Milano-Bicocca. The sample is placed between the poles of a Bruker ER-200 electromagnet, with its surface oriented parallel to the external magnetic field B_{ext} in what is known as a flip-chip configuration for IP measurements. To induce precession of the magnetization **M**, the samples were mounted on a grounded coplanar waveguide, which is connected to an rf source (Anritsu). The FMR signal at a fixed frequency is obtained by measuring the derivative of the absorbed power downstream of the electrical transmission line as a function of B_{ext}, using a lock-in amplifier. For

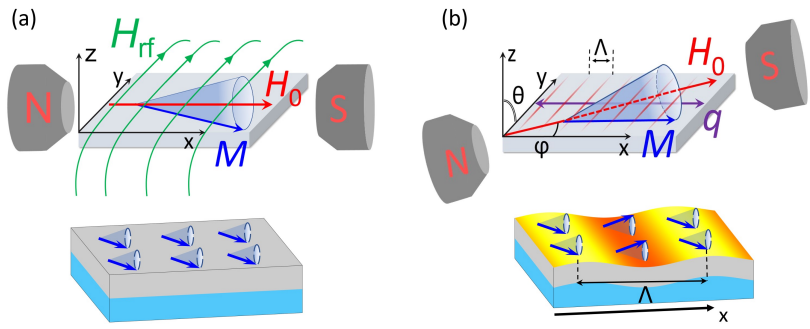

Figure 4.9: Illustration of the working principles behind B-FMR and SAW-FMR. (a) The IP static magnetic field H_{ext} determines the direction of the equilibrium axis for the magnetization $\mathbf{M}$; the RF excitation field H_{rf} is perpendicular to H_{ext} and induces precession in $\mathbf{M}$. Consequently, the magnetization precession is uniform throughout the entire sample. (b) In SAW-FMR, an acoustic wave (represented by the red stripes as wavefronts) with wavelength Λ drives magnetization precession via the effective MEC field. The magnitude of the magnetoelastic torque is influenced by the angle φ between H_{ext} (H_0) and the wavevector q. In this case, the magnetization precession is not uniform: it follows the spatial modulation of the acoustic driving wave, resulting in a spin wave SW. Adapted from Ref. [20].

additional details on the FMR setup, refer to Ref. [109].

The relationship between the FMR frequency f and the resonance field $H_{\text{eff}}^{\text{res}}$ is heavily influenced by the magnetic anisotropies present in the sample. For a thin, isotropic ferromagnetic film with an IP external field H_{eff}, Kittel's equation applies [8, 110]:

$$f = \frac{\mu_0 \gamma}{2\pi} \sqrt{H_{\text{eff}}^{\text{res}} \left(H_{\text{eff}}^{\text{res}} + \mu_0 M_{\text{eff}} \right)}. \tag{4.4}$$

The quantity M_{eff} is called effective magnetization [111, 112], and for a ferromagnet in saturation holds:

$$M_{\text{eff}} = M_{\text{s}} - \frac{2K_{\text{s}}}{\mu_0 M_{\text{s}} t}, \tag{4.5}$$

where K_{s} is the surface anisotropy constant and t is the thickness of the film.

The idea here was originally to compare results obtained on the very same sample from B-FMR and SAW-FMR. However, the sample SiO_2(10nm)/Ni(40nm)/SiO_2 did not show an acceptable B-FMR signal. The reason why can be explained in terms of growth-induced structural disorder induced by the amorphous substrate, which can hugely affect the B-FMR signal [95]. On the contrary, the SAW-FMR signal is very clear, a likely consequence of the locality of the measurements: in the B-FMR the signal is collected from the whole sample volume, while in SAW-FMR the probe footprint on the sample determines the portion of volume contributing to the signal.

The SiO_2(10nm)/Ni(14nm)/CaF_2(100) sample was specifically fabricated to facilitate a comparison between SAW-FMR and B-FMR, exhibiting improved structural properties due to the crystalline substrate. We apply to the investigation of SiO_2(10nm)/Ni(14)/CaF_2(100) the same approach used for SiO_2(10nm)/Ni(40)/SiO_2; in particular, we obtain maps at the three different TG pitches of $\Lambda = 2.54, 3.07$ and $4.00\ \mu\text{m}$, similarly to the ones

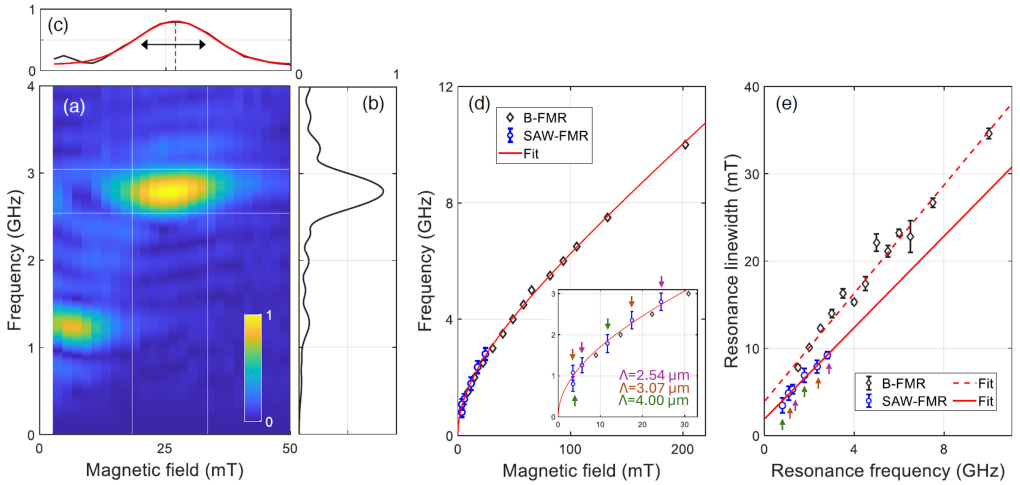

Figure 4.10: (a) To determine the field strength, frequency, and linewidth of the SAW-FMR resonances, the FFT magnitude maps have been symmetrically folded around the $B_{\text{ext}} = 0$ axis. (b) The resonance frequency is obtained by performing a Gaussian fit on the spectrum, which is integrated over a 10-mT range around the resonance. (c) Similarly, the resonance field strength and linewidth are extracted through Gaussian fitting of the lineshape, integrated over a 500-MHz range across the resonance. The white lines (a) mark the selected regions used for frequency and field integration. The presented map corresponds to the case of $\Lambda = 2.54$ µm; the same procedure has been applied for the other resonance at 1.26 GHz, and for the other pitch values. (d) The resonance frequencies observed from SAW-FMR at different TG pitches are plotted as a function of the resonance field strength (blue circles), alongside the results from B-FMR (black diamonds). The error bars represent the 95% confidence interval of the Gaussian fit and are not visible in the B-FMR data. Only a single fit of the Kittel model is shown (red solid line), as the best-fit curves for both datasets are indistinguishable at this scale. The inset zooms in on the low-frequency region; the arrows in pink, orange, and green indicate at which TG pitch the resonances have been observed, respectively $\Lambda = 2.54, 3.07$ and 4.00 µm. (e) The resonance linewidth is plotted against the resonance field for SAW-FMR data (blue circles) and B-FMR data (black diamonds). The colored arrows indicate the corresponding TG pitch as in the inset of panel (d). The linear fit of Eq. 4.6 is shown as a red line, solid for SAW-FMR, and dashed for B-FMR. Adapted from Ref.[20].

shown in Fig. 4.8 for the SiO_2(10nm)/Ni(40)/SiO_2 sample. For the sake of brevity, we show here only the one acquired with $\Lambda = 2.54$ µm. Fig. 4.10.a shows the 2D-FFT map obtained for the SiO_2(10nm)/Ni(14) CaF_2(100) sample with a TG pitch of $\Lambda = 2.54$ µm. As in the previous case, resonances are observed at the RSAW and SSLW frequencies, which for this sample are found to be $f_{\text{RSAW}} = 1.26 \pm 0.06$ GHz and $f_{\text{SSLW}} = 2.79 \pm 0.02$ GHz [20]. The first step in comparing SAW-FMR to B-FMR results involves extracting the resonance frequency and the corresponding field strength for each peak in the FFT magnitude maps. Additionally, the FWHM of each peak along the field axis is determined, as it provides valuable information about the damping. This procedure has been applied for the three available TG pitches. Fig. 4.10.a illustrates the process for $\Lambda = 2.54$ µm. To enhance contrast, the symmetry $B_{\text{ext}} \rightarrow -B_{\text{ext}}$ is utilized by folding the FFT map around the $B_{\text{ext}} = 0$ axis. From the folded map, the SAW-FMR resonance frequency is obtained by integrating over a suitable range of magnetic field values (around 10 mT, but checked to be not strictly relevant) across the center of the FFT peak; the obtained

curve shown in Fig. 4.10.b is then fit by using a Gaussian lineshape. Following the same approach, and integrating over a reasonable range of frequencies (approximately 500 MHz), the resonance magnetic field and its FWHM linewidth were determined in the same way by fitting with a Gaussian. Varying the TG pitch Λ allows to obtain six points for SAW-FMR to compare with B-FMR.

Fig. 4.10.d-e present a comparison between these results and those obtained using B-FMR. The resonance frequencies acquired through both techniques as a function of B_{ext} are shown in Fig. 4.10.d. Visually, the two datasets align well. To provide a quantitative analysis, the Kittel model (Eq. 4.4) is applied with both γ and M_{eff} as free parameters in the B-FMR data fitting. The best fit yields $\gamma = (2.10 \pm 0.06) \times 10^{11}$ rad/s·T and $M_{\text{eff}} = (199 \pm 18)$ kA/m; in more conventional units, this corresponds to $\gamma/2\pi = (32.0 \pm 0.9)$ GHz/T and $\mu_0 M_{\text{eff}} = (0.25 \pm 0.02)$ T. For the SAW-FMR data, γ is fixed at $\gamma = 2.10 \times 10^{11}$ rad/s·T, given the limited dataset. The model provided a fit for $M_{\text{eff}} = (195 \pm 16)$ kA/m, equivalent to $\mu_0 M_{\text{eff}} = (0.25 \pm 0.02)$ T, with excellent agreement observed between the two methods. It is worth noting the relatively low M_{eff} values, particularly when compared to the saturation magnetization of Ni at room temperature ($M_{\text{s}} = 490$ kA/m [3]). Generally, a reduction in M_{s} is anticipated, particularly in thin films and systems with significant surface anisotropy (see Ref. [109] and the Supplemental Material therein). According to Eq.4.5, the surface anisotropy can be calculated as:

$$K_{\text{s}} = (M_{\text{s}} - M_{\text{eff}})\mu_0 M_{\text{s}} t/2,$$

resulting in $K_{\text{s}} = (1.26 \pm 0.07)$ mJ/m^2, which is in close agreement with the values reported in the literature for rough thin films [113].

It is essential to highlight that the magnetostatic parameters obtained from SAW-FMR and B-FMR measurements are consistent. Since both methods produce the same M_{eff} value, we can deduce that the effect of the pump laser heating is negligible and locally the sample can be considered at room temperature, as it has also been observed in similar pump-probe experiments [17]. The FWHM linewidth ΔB of the resonances is shown in Fig. 4.10.e. For B-FMR, the linewidth corresponds to the FWHM in a sweep of B_{ext}. In the case of SAW-FMR, the FWHM is measured for the resonance peak along the field strength axis. To properly compare these values, the FWHM for SAW-FMR must be divided by $\sqrt{3}$. This adjustment is necessary, because the SAW-FMR maps display the FFT magnitude rather than the imaginary part, as in the B-FMR case; details based on Ref. [106] explaining the origin of the $\sqrt{3}$ factor can be found in App. A. Following standard FMR analysis [111], the Gilbert damping parameter α is determined by fitting the linear relationship between linewidth and resonance frequency:

$$\Delta B = \frac{4\pi\alpha}{\gamma} f + \Delta B_{\text{inh}}, \tag{4.6}$$

where ΔB_{inh} represents the inhomogeneous broadening term, leading to frequency-independent resonance broadening that creates an offset. This broadening is generally attributed to magneto-structural disorder [111]. The best-fit parameters are $\alpha = (47 \pm 5) \times 10^{-3}$ and $\Delta B_{\text{inh}} = (1.8 \pm 0.5)$ mT for SAW-FMR, and $\alpha = (52 \pm 2) \times 10^{-3}$ and $\Delta B_{\text{inh}} = (3.9 \pm 0.4)$ mT for B-FMR. The close agreement between these two techniques suggests that they probe the same underlying physics. The Gilbert damping values are consistent within the error bars, although the inhomogeneous broadening is slightly more pronounced in B-FMR. This difference can be attributed to larger-scale sample in-

homogeneities that contribute more to B-FMR, which is an area-integrated technique. The $25\,\mu$m diameter of the SAW-FMR probe footprint sets the spatial resolution of this technique: due to locality the influence of such inhomogeneities is greatly reduced.

It is important to note that the possibility to compare SAW-FMR with B-FMR is fundamentally determined by the SW dispersion at low q. As discussed in Sec. 1.3, the spin wave dispersion can exhibit non-monotonic behavior at low q due to dipolar interactions. However, in the specific case under consideration, the band dispersion is essentially flat within the relevant wavevector range; the calculation of the dipole-exchange spin wave dispersion for a polycristalline 14-nm-thick Ni thin film is reported in the supplementary of Ref [20]. Even though the TG excitation mechanism introduces a non-zero wavevector, if the band dispersion is flat in this range, no significant deviation from the FMR in frequency is observed. This is why Eq. 4.4 accurately describes the SAW-driven SW resonance as well.

4.4 Conclusions

In this chapter, we have explored the TG approach for investigating acoustically-driven dynamics in polycrystalline Ni thin films. We have demonstrated the importance of characterizing both acoustic and magnetic dynamics in a complementary manner for effective magnetoelastic studies. Additionally, the TG method enabled us to perform SAW-driven SW resonance efficiently without the need to fabricate additional devices for our samples. Furthermore, by comparing with B-FMR results, SAW-FMR is validated as an effective method for magnetic and magneto-elastic characterization. The spatial resolution is primarily limited by the probe laser footprint and the SAW wavelength, enabling potential sub-micron investigations with tight focusing and small Λ. This provides sensitivity to local magnetization dynamics, which is not possible with area-integrated techniques like B-FMR, as in the case of the SiO_2(10)/Ni(40nm)/SiO_2.

To conclude, Fig. 4.11 shows the phase space of an SAW-FMR - or SAW-SW resonance - experiment. Our SAW-FMR resonance data (black spheres) obtained for the SiO_2(10)/Ni(14nm)/SiO_2 sample are represented as a function of resonance frequency f, resonance magnetic field B_{res}, and SAW wavevector q. The resonance frequency f and resonance field $B_{\text{res}} = \mu_0 H_{\text{res}}$ are extracted from our data as described in Fig. 4.10.a-c. The three wavevectors ($q = 1.57$, 2.05, and 2.47 rad/µm) are represented by vertical planes (orange, light blue, and purple, respectively). Two acoustic modes, RSAW and SSLW, are involved. At a fixed q, the phase velocity of each mode determines two frequencies, with the projection onto the (f, q) plane (green dots) resulting in linear acoustic dispersion (pink linear fit). Due to the flat SW dispersion in the relevant range, the projection onto the (f, B_{res}) plane (blue dots) follows the nonlinear Kittel model trend (red fit). In this experiment, q is fixed by the TG, and tuning the magnetic field moves the SW manifold in phase space, while the SAW dispersions remain unchanged. Resonance occurs when a SW frequency matches that of a driving SAW. The projection onto the (f, B_{res}) follows the trend of the Kittel formula only because in this specific case the band dispersion is flat in the range of the investigated wavevectors. If not, the projected curve would be distorted, each point corresponding to a different SW wavevector, requiring more advanced models beyond the Kittel model. This challenge also presents an opportunity: SAW-FMR - or better SAW-SW resonance - could be valuable for wavevector-selective studies of low-energy excitations, where refined models would be necessary.

Momentum-dependent time-resolved scattering techniques are essential for probing

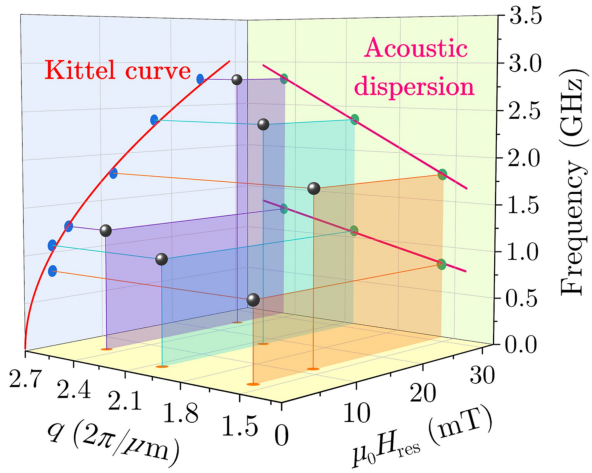

Figure 4.11: Phase space of SAW-FMR. Resonance frequencies are extracted from the 2D tr-Faraday maps with TG pitch of $\Lambda = 2.54$, 3.07, and 4.00 µm for SiO_2(10)/Ni(14nm)/SiO_2, plotted as a function of the observed resonance field $B_{res} = \mu_0 H_{res}$ and the TG-wavevector q (black spheres). Their wavevector dependency (projection on the green panel) gives the dispersions of the two SAWs (since they are acoustically driven); the magnetic field dependency (projection on the light blue panel) follows the Kittel model for FMR. From Ref. [20].

complex quantum systems, particularly in understanding the damping mechanisms of low-energy excitations. In SWs, a significant decay mechanism is two-magnon scattering, where a magnon at zero wavevector is annihilated, and a magnon with finite wavevector but the same energy is created. This process can only occur if the SW dispersion is non-monotonic. The presence of magnetostatic modulations at the wavevector of the resulting magnon enhances the TMS cross-section. Therefore, TG-based techniques could be advantageous in investigating this damping process, with potential indications of TMS manifesting as anomalies in Gilbert damping, as suggested by existing literature [114].

As a final note, it is important to mention that finer details of the SAW-SW dispersion crossing could be revealed through accurate time-domain analysis. While our current approach involved examining the FFT of the tr-Faraday 2D maps, a time-domain analysis might provide deeper insights into the phonon-magnon coupling mechanisms, revealing details not directly accessible from the coarse FFT structure (currently ongoing). This approach has proven effective in the investigation of magnetoelastic coupling in a ferromagnetic nanowire array, where the time-domain analysis allowed us to quantify the strength and the type of coupling involved in the phonon-magnon coupling [82].

CHAPTER 5

Magnonics

Time-resolved (tr) magneto-optical spectroscopy is a well-established technique for investigating magnetization dynamics across various time scales. In 2002, van Kampen et al. [17] demonstrated that FMR can be triggered and probed using tr-MOKE spectroscopy. Since this pioneering work, the approach has been widely adopted to study ultrafast demagnetization, relaxation, precession, and damping in various magnetic systems. These include thin films [115, 116], heterostructures [117], and nanostructured samples [82, 118]. The widespread application of this approach underscores the versatility and utility of tr-magneto-optical spectroscopy in exploring magnetization dynamics. More recently, Hascimoto et al. [119] developed a method based on the tr-Faraday technique to reconstruct the magnon dispersion in the $\mu\mathrm{m}^{-1}$ wavevector range, an approach that is highly valuable for investigating phenomena mediated by dipolar interactions. The diversity of the works cited so far highlights the broad applicability and potential of all-optical pump-probe spectroscopy for investigating spin waves in the ever-expanding zoo of functional materials. However, this conventional pump-probe scheme is limited to excitation of the normal modes of the sample [17, 120, 121], not allowing any control over the properties of the excited spin waves. The excitation of spin waves with specific properties and the investigation of the subsequent relaxation of the sample have been key research goals for decades, driven by both fundamental and technological interest. Numerous approaches have been explored and developed for this purpose.

As discussed in Sec. 2.2, the TG technique has been used since the 1970s to selectively excite acoustic and thermal dynamics in solids, soft materials, and liquids. Over the last decade, TG Spectroscopy has also become an effective tool for investigating spin excitations in solids. For instance, in magnetostrictive samples, acoustic waves with a tunable wavevector - excited by the TG pumping mechanism - can drive magnons of equal wavelength and acoustically trigger spin-wave resonance, as discussed in Ch. 4. However, this method is efficient only in samples with significant magnetoelastic coupling; furthermore, to efficiently drive magnetoelastic dynamics, the acoustic waves must resonate with the magnons, requiring the crossing of the acoustic and magnon dispersions curves. Cao et al. [74] addressed these limitations by directly exploiting the temperature profile generated by TG to excite magnons, without relying on magnetoelastic coupling. In their case, the TG pumping mechanism is implemented in a TEM, and the TG-driven standing magnons are probed via Lorentz microscopy. Here, we report on the possibility of implementing the very same approach in an all-optical table-top setup and at FELs, to achieve selectivity on a wide range of wavevectors, and consequently on the type of magnon.

This chapter is organized as follows: firstly, we will discuss how the TG excitation mechanism can be employed to excite coherent magnons at a tunable wavevector and

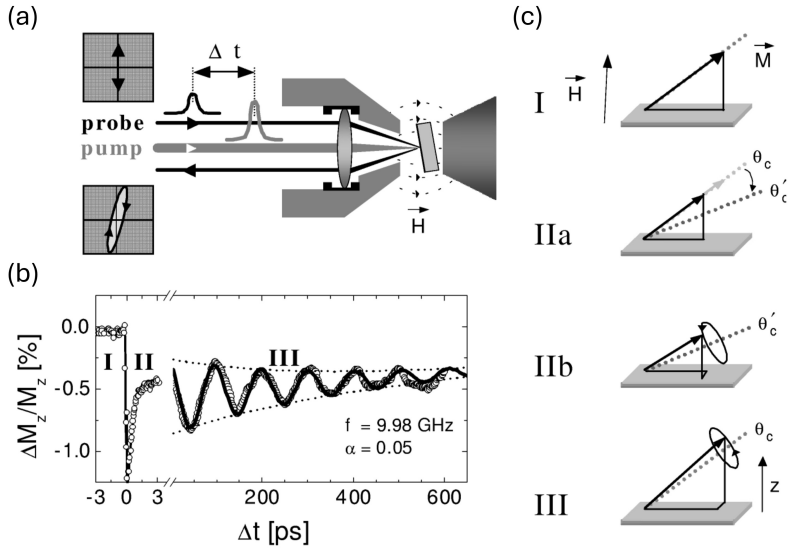

Figure 5.1: (a) Schematic pump-probe setup. The magnetization dynamics is measured via tr-MOKE. (b) Typical measurement on a 7 nm Ni film displaying the variation of the OOP component of the magnetization (ΔM_z) as a function of delay time Δt. Regions I, II and III represent the different stages of the dynamics. (c) Stages of the dynamics: I) Equilibrium IIa) Ultrafast demagnetization and softening of the anisotropy IIb) Precession around a non-equilibrium axis III) Precession around the equilibrium axis (FMR). Adapted from [17].

without relying on the magnetoelastic coupling; since we test this approach on a ferrimagnetic alloy with perpendicular magnetic anisotropy (PMA), this class of material will be introduced before diving into our experimental results.

5.1 Excitation and probing mechanism

In this section, we will discuss the pumping and probing mechanism of standing coherent magnons via TG spectroscopy.

Pumping

The key to understanding the excitation of standing magnons via the TG mechanism lies in the experiment conducted by Van Kampen et al. in 2002 [17] and illustrated in Fig. 5.1. In this study, tr-MOKE spectroscopy was employed to demonstrate that FMR can be driven in a 7-nm Ni thin film upon excitation with 100-fs long laser pulses. Fig. 5.1.a show a scheme of the pump-probe setup and Fig 5.1.b a measurement on a 7 nm thick polycrystalline Ni film on Si with IP anisotropy. Fig. 5.1.c provides a schematic representation of the laser-driven excitation mechanism for FMR. By applying an appropriate external OOP field H - along the hard axis of the Ni thin film - the magnetization is canted OOP. The canting angle θ_c is determined by the vectorial sum of external field and anisotropy fields. Upon impulsive heating by the pump pulse, two primary effects occur: (i) ultrafast demagnetization, which reduces the magnitude of the magnetization vector, and (ii) ultrafast softening of the magnetic anisotropy. This softening

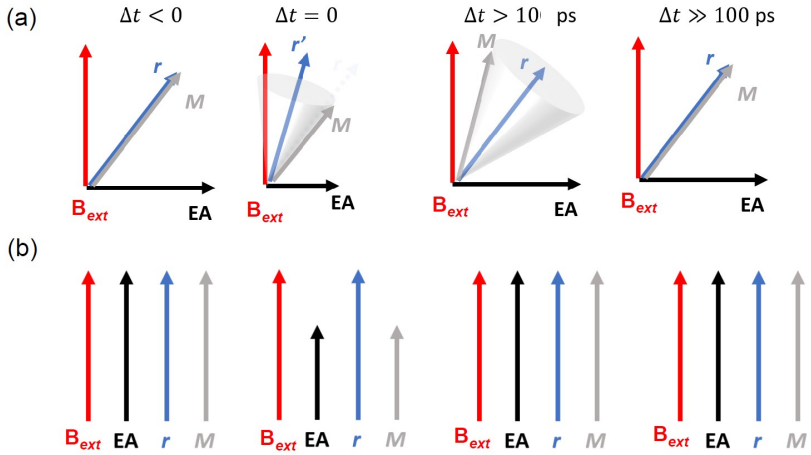

Figure 5.2: Sketch of the effect of the pump on the magnetization and the anisotropy EA at four different times to $\Delta t = 0$. B_{ext}, EA M, and r (r') are the external field, the easy axis/plane due to the anisotropy, the magnetization and the (non) equilibrium axis of the magnetization. (a) For non-collinear B_{ext} and EA a transient precessing dynamical state is excited. (b) For collinear B_{ext} and EA only magnetization quenching and recovery is observed.

arises from a weakening of the SOC and lattice distortion, which alters the energy landscape and reorients the magnetization's preferred directional axis. The redistribution of energy among the electron, spin, and lattice subsystems leads the quenched magnetization to gradually return to its equilibrium state. Typically, the time scale associated with electron-phonon interactions, referred to as fast remagnetization, occurs on the order of ps. In addition to this, the impulsive variation of the effective field causes the magnetization to precess around a non-equilibrium axis, which relaxes toward the equilibrium magnetization axis typically after tens of ps. At later times, the dynamics is essentially the one observed by FMR, with the magnetization precessing around the initial equilibrium axis on a timescale ranging from 100 picoseconds to nanoseconds. On this timescales, the coherent dynamics is superimposed to a slower remagnetization process, attributable to the energy dissipation from the lattice bath of the magnetic layer to the nonmagnetic layers and substrate. To drive magnetization precession (FMR), the magnetization must be displaced from its easy axis/plane. This means that a key condition for triggering precession is having a magnetic field component strong enough to combine with the anisotropy field and reorient the magnetization away from the easy axis/plane. In the case of an external field applied along the easy axis, the reduction of anisotropy field strength induced by the pump does not affect the direction of the equilibrium magnetic axis, so the only effect observed is thermal quenching and subsequent recovery. Fig. 5.2 schematically depicts the different dynamics depending on the orientation of the external magnetic field. It follows that in our case of a sample with PMA, the applied field to drive magnetization precession must have an IP component.

Let's now consider a TG excitation. The quasi-stationary temperature profile $T(x)$ arising from the pump interference, gives rise two main phenomena: a density grating that leads to the generation of surface acoustic waves via impulsive thermoelastic expansion [19, 54] and a transient magnetization grating arising from the local thermal

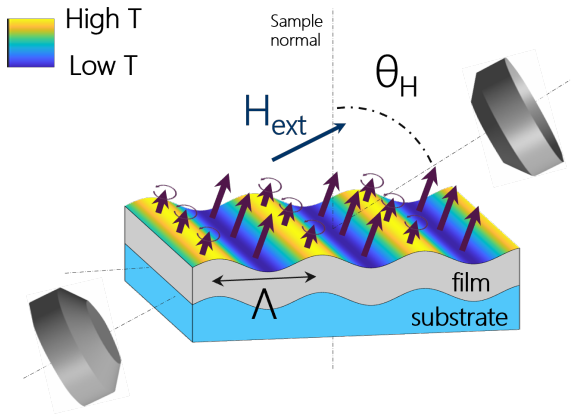

Figure 5.3: Simplified schematic of the excitation mechanism for standing spin waves via TG spectroscopy. The colormap illustrates the spatially periodic transient temperature profile created by the interference of pump pulses. In the high-temperature regions, the spins undergo demagnetization and anisotropy softening, which eventually leads to precession around the magnetization equilibrium axis. In contrast, the spins in the low-temperature regions of the sample remain unaffected. As this initial transient dynamic relaxes towards equilibrium, standing magnons form with a wavelength equal to the TG pitch Λ. Surface acoustic waves (wavy substrate) are also excited by impulsive thermoelastic expansion; however, they do not influence the magnetization dynamics.

demagnetization of the sample. The first case has been discussed in Ch. 4, so here we will focus on the latter one. The transient magnetization grating induces a periodic time-dependent variation of the optical constants, causing the probe to be diffracted. Fig. 5.3 depicts the effects of an intensity grating in a magnetic sample at a $\Delta t \simeq 10$ ps. The color map represents the spatially periodic transient temperature profile arising from the interference of pump pulses. As a result, in the "high T" region of the sample - where the two pump beams interfere constructively - the impulsive temperature rise locally triggers the precession of the magnetization as depicted in Fig. 5.1.c, while spins remain unaffected in the "low T" regions - where destructive interference of the pump beams takes place. Fig. 5.3 schematically represents this initial transient dynamics. Finally, the locally induced FMR dynamics combined with the spatial periodicity characteristic of the TG excitation results in standing spin waves at the TG wavevector. However, the precise visualization and time evolution of such spin waves is pretty complicated since, after the $\simeq 10$ ps transient, the initial precessional angle of the magnetization θ (amplitude of the precessional cone) is directly related to the spatial and temporal profile of the TG temperature grating. To better understand this, in Fig. 5.4 is reported the correlation of some key parameters and their dependence along the TG spatial profile at a fixed time delay. Depending on the incident pump fluence the variation of the angle θ can go up to $\simeq 20°$ in the high-T regions, while remains essentially zero in the low-T areas. This holds for every $\Delta t > 0$, giving rise to a complex and spatially-and-temporally periodic collective precessional dynamic: by definition, a standing spin wave.
As discussed above, the SW wavevector selectivity is intrinsic to the excitation mechanism. This selectivity is especially desirable for investigating how spin wave properties - such as frequency, amplitude, and damping - vary as a function of the wavevector. Additionally, the tunability of the wavevector allows for the excitation of spin waves

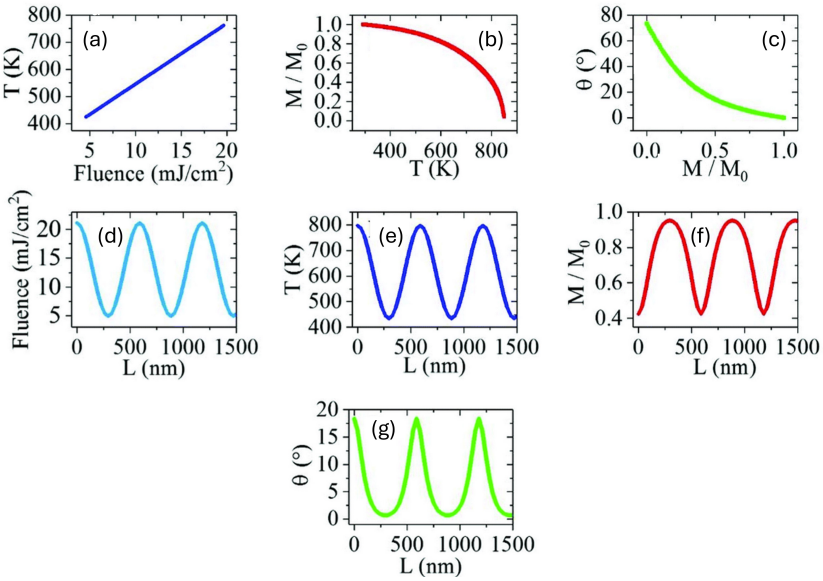

Figure 5.4: (a) Correlation of local laser fluence and local temperature. (b) Temperature dependence of the saturation magnetization of a permalloy. (c) Initial precession angle (θ), as a function of saturation magnetization. Spatial distributions for a TG pitch of $\Lambda \simeq 750$ nm (d) laser fluence, (e) sample temperature, (f) magnetization, and (g) precession angle across the transient grating after the initial magnetic transient photoexcitation. Adapted from [74].

mediated by different interactions. For instance, excitation in the near-infrared (near-IR) or visible range - where the TG pitch is on the order of micrometers - results in the excitation of dipolar waves. The same approach implemented at photon energies in the EUV or X-ray range, as available at FELs, allows the excitation of exchange-mediated spin waves [53, 122]. By combining results obtained from both the visible and EUV ranges, it is then possible to gain a comprehensive understanding of the system's response to "forced" magnetic excitations, spanning from the nanoscale sensitive to short ranged interactions to the mesoscale where only dipolar terms survive.

Probing

Typically, in all-optical spectroscopy, the spin wave are detected by isolating the rotated component of the polarization of the incoming probe beam, as done in standard tr-MOKE or tr-Faraday. Here, we implement a similar polarization analysis, but on the diffracted probe beam. Adopting the convention of designating s-polarized beams as "vertically" polarized (V) and p-polarized beams as "horizontally" polarized (H), we label the experimental configuration for typical acoustic measurements as $VVVV$. In this notation, the first two "V"s refer to the polarization state of the pump beams, the third denotes the polarization of the probe beam, and the final one specifies the measured component of the TG diffracted probe beam. In the case of a non-birefringent isotropic sample, all information about the acoustic dynamics is collected from the V component of the diffracted probe beam. In contrast, the magnetic dynamics arising from the transient magnetic texture induces an H-polarized component in the diffracted probe beam,

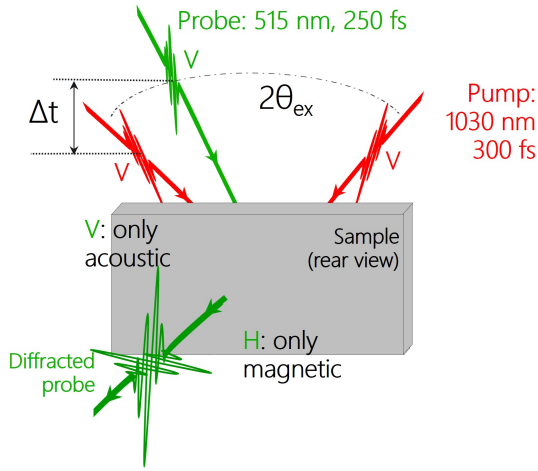

Figure 5.5: Rear view of the experimental scheme. Pump beams (in red) are vertically polarized (V) and impinging on the sample with an angle of $2\theta_{ex}$. Probe beam (in green) is also vertically polarized. Acoustic or magnetic dynamics is efficiently isolated via polarization analysis.

requiring polarization analysis. If the experimental conditions allow for the excitation of standing spin waves via TG pumping, the H-component of the magnetization is expected to exhibit oscillations related to the coherent magnetization dynamics. The $VVVH$ signal $\mathcal{S}_{VVVH}(t)$ - at $\Delta t \gtrsim 10$ ps - can then be treated as any other signal generating from the superposition of a quasi-static grating with a dynamical one, therefore it can be phenomenologically expressed as [53]

$$\mathcal{S}_{VVVH}(t) = \left[a_0 e^{-\frac{t}{\tau}} + a_1 e^{-\frac{t}{\tau_1}} \sin(2\pi f + \phi)\right]^2 + C, \tag{5.1}$$

which describes the slow remagnetization of the sample via thermal transport (first term) and the damped spin wave oscillations (second term) on a background (C). Therefore, τ is the thermal relaxation time of the magnetization grating, while f, τ_1 and ϕ are the frequencies, decay time and phase of the standing spin wave, respectively.

In our specific case, we isolate the time-dependent H-polarized component and record its intensity with a photoreceiver fed into a lock-in amplifier.

5.2 Sample details

Ferrimagnets are a class of magnetic materials exhibiting properties that fall between those of antiferromagnets and ferromagnets, as schematically depicted in Fig. 5.6. They consist of two or more magnetic sublattices where the magnetic moments have different magnitudes and orientations. Within each sublattice, the magnetic moments align on average in the same direction, but between sublattices, the directions are opposite, creating the antiparallel alignment typical of antiferromagnets. This provides ferrimagnets with several properties associated with antiferromagnets that are desirable for technological applications, including benefits, such as reduced stray magnetic field, rapid dynamic responses, and weak dependence on external magnetic fields. However, unlike anti-

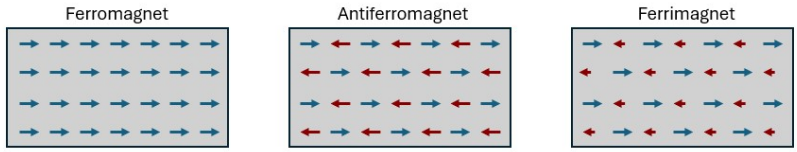

Figure 5.6: Simplified scheme of the magnetic order for ferromagnets, antiferromagnets and ferrimagnets. Ferrimagnets have intermediate properties between ferromagnets and antiferromagnets, due to the antiferromagnetic coupling between sublattices having magnetic moments of different magnitude.

ferromagnets, the difference in the magnitude of the magnetic moments between the sublattices ensures a small net magnetization. Such ferromagnetic-like behaviour makes ferrimagnets suitable to be investigated with the same - well established - experimental techniques and methods used for ferromagnets. This is a major practical advantage over antiferromagnets, whose properties are typically difficult to measure. Several materials display ferromagnetic order. We adopt as a case of study a rare-earth (RE) transition-metal (TM) binary compound. The stoichiometry is of the type RE_xTM_{1-x}; among the many possible combinations RE-TM combinations, Tb and Gd are the most common RE elements, and Fe or Co the most common TM metal ones. These alloys are particularly interesting from both a fundamental and a technological point of view because by tuning the stoichiometry, the magnetic properties can be finely controlled. The most interesting magnetic behaviors are typically restricted at $20 < x < 35$, where compensation of magnetic and angular momentum of the sublattices can be achieved [123]. It follows that this class of materials displays intriguing phenomena, that will be addressed in the following section by analyzing both the equilibrium magnetic properties and the dynamics on the fs-ps timescale.

5.2.1 Static magnetic properties

The magnetic interaction between inter and intra-sublattice spins in a ferrimagnet can be described with three interaction parameters: $J_{\text{TM-TM}}$, $J_{\text{TM-RE}}$ and $J_{\text{RE-RE}}$ [124, 125]. $J_{\text{TM-TM}}$ ($J_{\text{RE-RE}}$) quantifies the ferromagnetic coupling of the TM (RE) spins forming the TM (RE) sublattice. Typically, $J_{\text{RE-RE}} \ll J_{\text{TM-TM}}$ because of the small spatial extent of the $4f$ orbitals: in pure RE elements, ferromagnetism, is determined by the 6s and 5d valence electrons mediated through the Ruderman-Kittel-Kasuya-Yosida (RKKY) interaction, involves spin polarization induced by 4f ions that oscillates and weakens with distance. This leads to parallel or antiparallel coupling and remains weakly ferromagnetic even when RE atoms are alloyed with TMs, but the $J_{\text{RE-RE}}$ its two orders of magnitude smaller than $J_{\text{TM-TM}}$. $J_{\text{TM-RE}} < 0$ describes the antiferromagnetic coupling between the TM and RE spin belonging to different sublattices; typically, it holds that $J_{\text{TM-TM}} > J_{\text{TM-RE}} > J_{\text{RE-RE}}$.

Magnetization compensation point

The intra-sublattice ferromagnetic-like and inter-sublattice antiferromagnetic-like coupling, at given composition x and temperature T determines the net magnetic moment

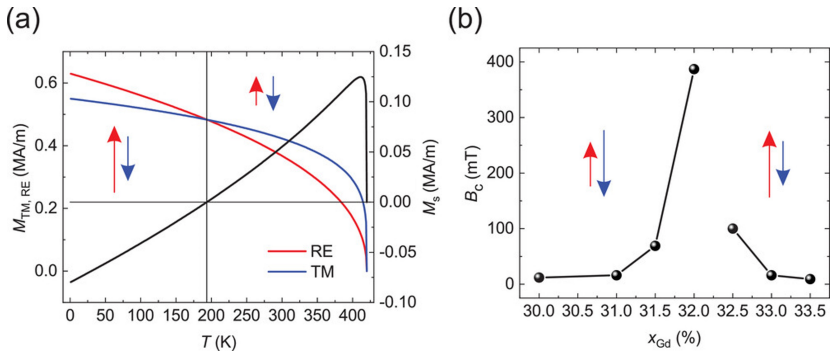

Figure 5.7: Magnetization compensation point of RE-TM ferrimagnets. (a) Calculated temperature dependence of the RE = Gd (red) and TM = FeCo (blue) magnetizations according to a Bloch-like law. The red and blue arrows represent the magnitude of the sublattice magnetizations. Their different temperature dependence causes the net magnetization $M_{\mathrm{TM}} - M_{\mathrm{RE}}$ (right vertical axis) vanish at the magnetization compensation temperature T_M (190 K in this specific case). Above the Curie temperature $T_c = 440$ K, the entire system becomes paramagnetic. (b) Dependence of the coercive field on the Gd concentration measured via the Anomalous Hall Effect in sputtered $Gd_x(FeCo)_{1-x}$ films. The divergence at $x_{\mathrm{Gd}} = x_{\mathrm{M}} \simeq 32\%$ identifies the magnetization compensation point. Adapted from [123].

μ_{net} and average equilibrium magnetization M_s:

$$\mu_{\mathrm{net}}(x,T) = |(1-x)\mu_{\mathrm{TM}} - x\mu_{\mathrm{RE}}|, \tag{5.2}$$

$$M_s(x,T) = |M_{\mathrm{TM}} - M_{\mathrm{RE}}| \tag{5.3}$$

From Equation 5.2 it is clear that it is possible to obtain a nearly-perfect antiferromagnetic behaviour by tuning the composition. A similar result can also be obtained by adjusting the temperature, since the curve $M_{\mathrm{RE}}(T)$ decays more rapidly with the temperature relative to $M_{\mathrm{TM}}(T)$. The compensation composition and temperature at which the ferrimagnets have a nearly zero average magnetization are called magnetization compensation composition x_M and temperature T_M. Fig. 5.7.a illustrates the temperature dependence of RE and TM magnetizations calculated using a mean-field model [123]. The RE magnetization is dominant at low temperatures but decreases more rapidly than the TM magnetization. Thus, the total magnetization is RE-like at low temperatures and TM-like at high temperatures, with the compensation temperature $T_c = 190$ K marking the switchover. Above the Curie temperature, T_c the material becomes paramagnetic [126]. The dominant sublattice at a fixed temperature depends on the concentration. Likewise, the coercive field peak in 5.7.b identifies x_{M} and the transition point, caused by the disappearance of net magnetization and reduced magnetic susceptibility. Measuring x_{M} or T_{M} helps determine the magnetic configuration of the given alloy, which can vary with growth conditions, substrates, thicknesses, and capping layers [127].

Magnetic anisotropy

RE-TM ferrimagnets, despite their amorphous structure which suggests isotropic properties [128, 129], exhibit uniaxial anisotropy ($E = k_1 \sin^2\theta + k_2 \sin^4\theta$), with k_1 often positive, favoring OOP orientation. The exact cause of this anisotropy is still unclear

and is connected to several factors such as sample growth conditions, large single-ion anisotropy of RE atoms due to electrostatic interactions [130], structural inhomogeneities from phase separation, magnetostriction and anisotropic stress. These factors indicate that the anisotropy can be influenced by various parameters such as stoichiometry, element type, growth conditions, and thickness in the case of thin film samples. The anisotropy is an intrinsic bulk property, enhanced in thick films, and does not require interface engineering for OOP orientation. This anisotropy is most significant near the magnetization compensation point, minimizing demagnetizing field effects, which makes ferrimagnets ideal for data storage applications due to their stability against thermal fluctuations.

5.2.2 Dynamical properties

Effective LLG equation

The dynamics of ferrimagnetic alloys can be described by the same LLG equation employed for ferromagnets, by replacing the Gilbert damping α and the gyromagnetic ratio γ with effective parameters. Let's consider the case of two sublattices. If we define the net unitary magnetization $\mathbf{m} = \mathbf{M_1}/M_1 + \mathbf{M_2}/M_2$ in terms of the magnetization of the two sublattices $\mathbf{M_1}$ and $\mathbf{M_2}$, it can be demonstrated that the LLG equation can be written as

$$\frac{d\mathbf{m}}{dt} = -\gamma_{\text{eff}}\mathbf{m} \times \mathbf{H}_{\text{eff}} + \alpha_{\text{eff}}\mathbf{m} \times \frac{d\mathbf{m}}{dt} \tag{5.4}$$

$$\gamma_{\text{eff}} = \frac{M_1 - M_2}{\frac{M_1}{\gamma_1} - \frac{M_2}{\gamma_2}} = \frac{M}{A} \tag{5.5}$$

$$\alpha_{\text{eff}} = \frac{\frac{\alpha_1 M_1}{\gamma_1} + \frac{\alpha_2 M_2}{\gamma_2}}{\frac{M_1}{\gamma_1} - \frac{M_2}{\gamma_2}} = \frac{\alpha_1 A_1 + \alpha_2 A_2}{A} \tag{5.6}$$

where $\alpha_{1(2)}$, $\gamma_{1(2)}$ and $A_{1(2)}$ are the damping parameter, gyromagnetic ratio and angular momentum of the sublattice 1 (2); therefore, it follows that $M = M_1 - M_2$ and $A = A_1 - A_2$ are the net magnetization and the net angular momentum, respectively.
From equations 5.4-5.6, few consideration can be made:

- At the magnetization compensation point, where the ferrimagnet behaves statically as a an antiferromagnet ($M \to 0$), $\gamma_{\text{eff}} \to 0$ and the effective field $\mathbf{H_{eff}}$ practically does not play a role anymore in the dynamics equation
- Since $A_{1(2)} = \frac{M_{1(2)}}{\gamma_{1(2)}}$ and $M_{1(2)} = M_{1(2)}(T)$, it follows that $A_{1(2)} = A_{1(2)}(T)$ and $A = A(T) = A_1(T) - A_2(T)$. This suggests that there is a temperature T_A - commonly defined as the angular momentum compensation temperature - at which the net angular momentum vanishes $A \to 0$ and any variation of $\mathbf{m}$ becomes infinitely fast, as experimentally observed also in antiferromagnets.
- Given that $g_{\text{RE}} < g_{\text{TM}}$, T_A is expected to be higher than T_M.

Similarly to magnetization compensation, angular momentum compensation can be attained by not only adjusting the temperature but also by modifying the composition x of the ferrimagnetic alloy, as demonstrated in various experiments (see e.g. Ref. [131]).

Physical quantity	T_M, x_M	T_A, x_A
Total magnetization	0	finite
Total angular momentum	finite	0
Resonance frequency	finite	∞
Damping	finite	∞
Gyromagnetic ratio	0	∞
Coercive field	∞	finite
Anisotropy	finite	finite

Table 5.1: Relevant physical quantities at magnetization (T_M, x_M) and angular momentum compensation point (T_A, x_A). Adapted from [123]

It is of crucial importance to stress the differences of the *magnetization* and *angular momentum* compensation phenomena. At the magnetization compensation point, the net equilibrium magnetization $M \to 0$ and the magnetic ordering can be considered antiferromagnetic; however, it is at the angular momentum compensation point that the dynamic behavior of ferrimagnets switches from ferromagnetic-like to antiferromagnetic-like even if there a finite magnetization remains. This is a direct consequence of the quantum-mechanical behavior of the magnetization that is related to the total angular momentum commutator.
Tab. 5.1 summarizes the expected behavior of the main relevant physical quantities at the magnetization and angular momentum compensation points. However, it must be underlined that the divergences at the compensation points are not physical but arise from treating ferrimagnets similarly to ferromagnets. This approach can be reasonable near the magnetization compensation point because the transition there only reverses the quantization axis without any other physical effects. However, the divergence associated with the coercive field H_c is not physically meaningful, since H_c is not defined in a system without net magnetization. In contrast, the dynamics of antiferromagnets is fundamentally different from those of ferromagnets, causing the standard LLG equation to fail near T_A. Furthermore, this oversimplified model, as good as it is to understand the complexity of ferrimagnetic dynamics, fails in predicting the normal modes of the system observed experimentally [121] since it does not take into account the antiferromagnetic coupling between sublattices.

LLG equation for two coupled sublattices

A more accurate picture can be obtained describing the equation of motion of a two-sublattice ferrimagnetic system can be written in the form of two coupled LLG equations [4, 121, 132]:

$$\frac{d\mathbf{M}_i}{dt} = \gamma_i(\mathbf{M}_i \times \mathbf{H}_i^{\text{eff}}) + \frac{\alpha_i}{|\mathbf{M}_i|}(\mathbf{M}_i \times \frac{d\mathbf{M}_i}{dt}), \tag{5.7}$$

where α_i is the phenomenological Gilbert damping parameter, γ_i is the gyromagnetic ratio, and $|\mathbf{M}_i|$ is the saturation magnetization of the ith sublattice ($i = 1, 2$). $\mathbf{H}_i^{\text{eff}}$ represents the total effective field, including the external field, the anisotropy field, and the inter-sublattice exchange coupling field that acts on the magnetic moments of the ith sublattice.

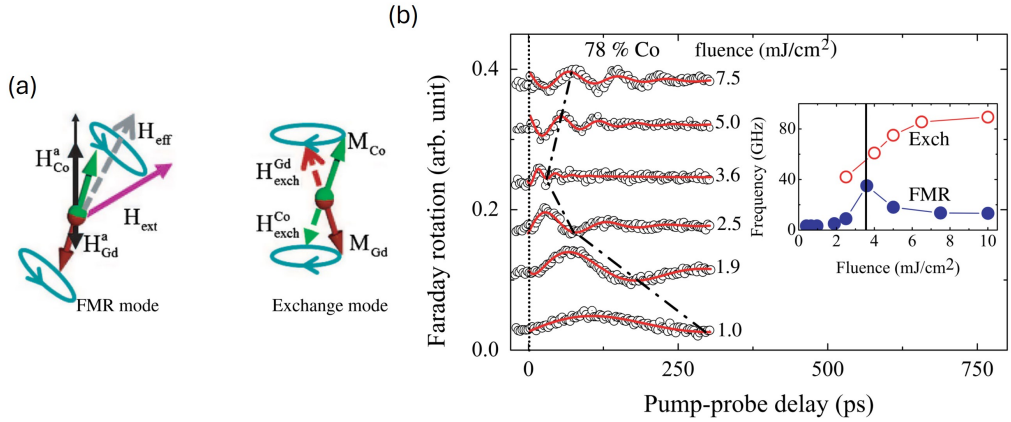

Figure 5.8: (a) Schematics showing the expected modes in an CoGd ferrimagnetic alloy. Precession of the magnetization around the effective field $\mathbf{H}_{\text{eff}}$ results in the ferromagnetic resonance mode; the exchange fields $\mathbf{H}_{\text{exc}}^{\text{Co, Gd}}$ give rise to the exchange mode. (b) tr-Faraday signals as a function of pump fluence for a 20-nm-thick $CO_{78}Gd_{22}$ amorphous thin film. Pumping with 100-fs pulses at 805 nm and a fluence of 3.6 mJ/cm^2 brings the sample to the angular momentum compensation point. In the neighborhood of this fluence, an increase in the FMR mode frequency by approximately 40 GHz is observed, along with a softening of the exchange mode. Adapted from [121]

The effective fields experienced by the first and second sublattices can be written as:

$$\mathbf{H}_1^{\text{eff}} = \mathbf{H}_{\text{ext}} + \mathbf{H}_1^{\text{A}} + \lambda_{2\to1}\mathbf{M}_2, \tag{5.8}$$

and

$$\mathbf{H}_2^{\text{eff}} = \mathbf{H}_{\text{ext}} + \mathbf{H}_2^{\text{A}} + \lambda_{1\to2}\mathbf{M}_1, \tag{5.9}$$

where $\mathbf{H}_{\text{ext}}$ is the externally applied magnetic field, $\lambda_{2\to1}$ is the inter-sublattice exchange coupling coefficient between the two sublattices, $\mathbf{H}_1^{\text{A}}$ and $\mathbf{H}_2^{\text{A}}$ are the magnetic anisotropy fields of the first and second sublattices, and $\lambda_{2\to1}\mathbf{M}_2$ and $\lambda_{1\to2}\mathbf{M}_1$ are the exchange fields created by the second and first sublattices, respectively.

The approximate solution of Eq. 5.7 provides two homogeneous modes of spin resonance, schematically depicted in Fig. 5.8. The first one is the FMR mode, the frequency of which is proportional to the effective magnetic field [133]:

$$f_{\text{FMR}} = \gamma_{\text{eff}} H_{\text{eff}}, \tag{5.10}$$

where γ_{eff} is express as in Eq. 5.10. In addition to the well-known ferromagnetic resonance mode, ferrimagnets can also exhibit an additional high-frequency exchange mode. This mode arises due to the inter-sublattice exchange coupling, which is similar to the behavior observed in antiferromagnetic modes. The frequency of this exchange mode is given by [133, 134] :

$$f_{\text{exch}} = \lambda_2\gamma_1\gamma_2[M_1/\gamma_1 - M_2/\gamma_2]. \tag{5.11}$$

The frequencies of both modes thus depend on the relative concentrations of TM and RE ions in the alloy as well as on temperature. Because of the large value of the exchange fields, the frequency of the exchange mode, f_{exch}, usually falls in the infrared (THz) region. It is evident from Eq. 5.10 and Eq. 5.11 that, at the angular momentum

compensation point, f_{FMR} is expected to sharply increase, while f_{exch} is expected to exhibit the opposite behavior. This has been experimentally observed, for example, in Ref. [121], where the authors employ tr-Faraday polarimetry to demonstrate the possibility of impulsively bringing the sample - an amorphous $Co_{78}Gd_{22}$ alloy thin film - to angular momentum compensation by tuning the pump laser fluence, as shown in Fig. 5.8.b.

A complete picture for ferrimagnetic dynamics

Considering two coupled sublattices allows to obtain a better picture of the active modes but still does not overcome the problem connected to the divergent physical quantities at the angular momentum compensation point. A more rigorous approach for describing the ferrimagnetic dynamics is based on considering the Néel vector rather than the net magnetization, as described in detail in Ref. [135]. Furthermore, the issues related to the divergent physical quantities at the angular momentum compensation point (see Tab. 5.1) can be solved by considering the ferrimagnetic system as a whole rather than two coupled subsystems; this is generally implemented by introducing a Rayleigh function. The interested reader can find more details in the following references [4, 136, 137]. In the framework of this thesis, the models described above are adequate to analyze the data and propose an interpretation of the observed phenomena.

5.3 Experimental results

In this section, we will discuss measurements performed in the framework of an international collaboration, aimed at demonstrating how the TG excitation mechanism can be used to selectively excite magnons over a broad range of wavevectors by pumping in both the optical and EUV ranges. Most of this chapter will present and interpret the laser-based measurements. In the final section, the main results obtained through the collaborative beamtime access at the TIMER@FERMI beamline in Trieste will be discussed. We show the complementarity and potential of both optical and EUV TG approaches for investigating coherent magnons over a broad range of selected wavevectors.

5.3.1 Results on $Co_{78}Gd_{22}$ via TG optical spectroscopy

The experimental results presented in this section are obtained at the NFFA-SPRINT lab using the setup operational mode described in Sec. 3.1.

The sample consists of a CoGd ferrimagnetic alloy with PMA. The detailed sample structure and composition is Pt(3nm)/$Co_{78}Gd_{22}$(15nm)/Pt(1.5nm)/Ta(1.5nm) deposited on float glass by magnetron spattering. The static magnetic characterization performed via polar MOKE shows a clear OOP uniaxial magnetic anisotropy and coercive and saturation field of $\mu_0 H_c \simeq \mu_0 H_s \simeq 176$ mT. The hysteresis is omitted here for the sake of brevity but can be found in App. B, along with further details on the growth of the sample.

The pump footprint (FWHM) on the sample is measured as 38 x 35 μm^2, while the probe one is 20 x 19 μm^2. The pump fluences reported below account for the presence of two pump beams on the sample and the inhomogeneity of the TG excitation, which results in an effective area that is half the size of the actual spot footprint on the sample; this latter aspect is also taken into account in the probe fluence calculation. The effective laser repetition rate was kept fixed at 100 KHz. All measurements were performed

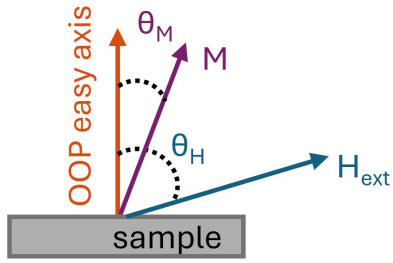

Figure 5.9: Experimental scheme. The applied field is at an angle $\theta_H = 72°$ (unless differently specified) from the OOP the easy axis (surface sample normal). The equilibrium magnetization is at an angle θ_M determined by the vectorial sum of external field and anisotropy.

in air and with a TG pitch of 2.54 µm. The magnetic field was generated by a pair of permanent magnets; to regulate its intensity, we mechanically fine-adjust the distance between the poles. Due to the OOP easy axis, the magnet was positioned coplanar with the scattering plane and oriented at $\theta_H = 72°$ relative to the sample normal to have an IP component to excite magnons as described in Sec. 5.1. A sketch of the described geometry is shown in Fig. 5.9. The orientation of the equilibrium magnetization is determined by the vector sum of the external magnetic field and the OOP uniaxial anisotropy. Since the magnetic fields applied during the measurements of B_{ext} =260 mT and B_{ext} =180 mT are not intense enough to saturate the sample along the $\mathbf{B}_{\text{ext}} = \mu_0 \mathbf{H}_{\text{ext}}$ direction, we use *Ubermag* [138] - a Python package for conducting micromagnetic simulations - to obtain a complete understanding of the equilibrium state and extract this information. The simulations based on energy minimization are reported in App. B, and predict $\theta_M \simeq 21°$ and $\theta_M \simeq 5°$ for $B_{\text{ext}} = 260$ mT and $B_{\text{ext}} = 180$ mT, respectively.

The detection branch is precisely aligned to capture the scattered probe at the phase-matching angle using the $m = -1$ order of 515 nm as a reference. Switching from the VVVV to VVVH configuration is easily done by bringing the polarizer in the detection branch close to extinction. The acoustic characterization (*VVVV* configuration) conducted during this measurement campaign is primarily aimed at verifying the distinct timescales of magnons and acoustic waves, as well as confirming that the magnons are excited independently of the thermoelastic TG-induced dynamics, therefore without relying on the magnetoelastic coupling. The acquired data are reported in App. B.

Observation of coherent magnons

Fig. 5.10. shows the *VVVH* signals measured with the external magnetic field at an angle $\theta_H = 72°$ and two different magnetic field intensities (180 and 260 mT). Fitting the signal with Eq. 5.1 accurately reproduces the data, allowing the extraction of parameters describing the magnon with acceptable accuracy. As expected, we observe an increase in frequency from 7.07 ± 0.03 to 9.58 ± 0.03 GHz: at a fixed wave vector (q = 2.47 μm^{-1}), an increase in the magnetic field intensity results in a shift of the magnonic band dispersion $\omega = \omega(k, \mathbf{H})$ towards higher frequencies [22]. This key observation allows us to attribute the observed oscillatory behavior to magnons, rather than to other polarization-dependent but magnetic-field-independent phenomena (e.g. birefringence). In addition to this, since the detection branch of the experimental setup has been finely aligned to collect only the probe beam scattered at the angle imposed by the phase matching con-

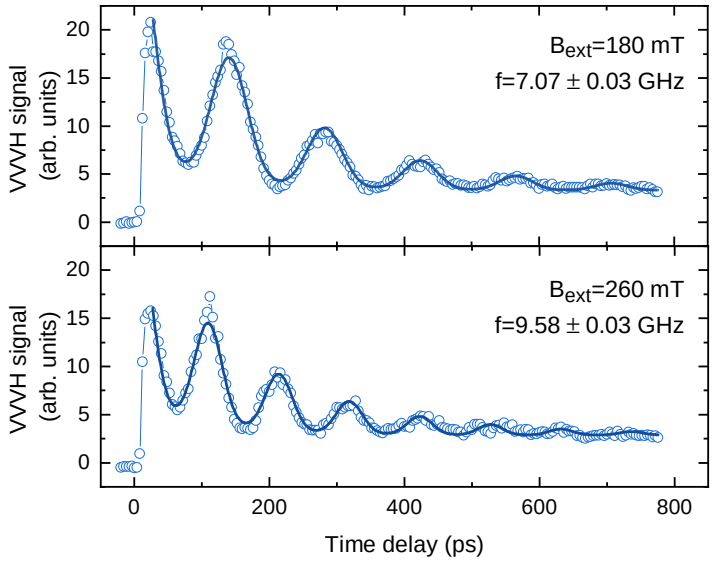

Figure 5.10: Magnetic signals acquired with applied magnetic fields of 180 mT and 260 mT. For both signals, the pump and probe incident fluence on sample is set at 18.8 mJ/cm^2 and 0.26 mJ/cm^2, respectively. Solid lines are the best fit to the data using Eq. 5.1.

dition (see Ch. 2.2), we can also confidently claim that the excited magnon has been the very same wavevector imposed by the TG. Indeed, if the magnon wavevector were different, the probe beam would be diffracted at a different angle determined by the phase-matching condition and consequently would not be collected by the detection branch. The frequency we extract at B_{ext} =260 mT is compatible with the FMR one measured in [131] by performing tr-MOKE on a similar sample and in an equivalent magnetic field configuration. This indicates that although we excite magnons at the finite TG wavevector of $q = 2.47\,\mu\text{m}^{-1}$ - similarly to what was observed in Ch. 4 - the magnon band in $Co_{78}Gd_{22}$ does not disperse significantly in the low-q range. As a result, it is difficult to distinguish a consistent difference from the precessional FMR frequency, as also demonstrated in Ref. [139] on a similar sample.

On the excitation mechanism

Fig. 5.11 shows the diffracted *VVVH* signals under similar conditions of pump fluence and external field intensity, but at different θ_{H}. Specifically, at $\theta_{\text{H}} = 72°$, magnons are excited, as discussed in the previous section. However, when the external field is aligned along the easy axis ($\theta_{\text{H}} = 0°$), no coherent dynamics is observed due to the absence of an IP B_{ext} component. We still observe a *VVVH* signal in this configuration, as the TG excitation thermally induces a transient magnetic texture that causes the probe to be diffracted, consistent with experimental observations using TG EUV-range pumping [49].

In addition to the lack of oscillations related to coherent magnetization dynamics, the trace acquired with $\theta_{\text{H}} = 0°$ shows a slower rise and a decay. A systematic investigation of the signal behavior as a function of θ_{H} is necessary to better understand these

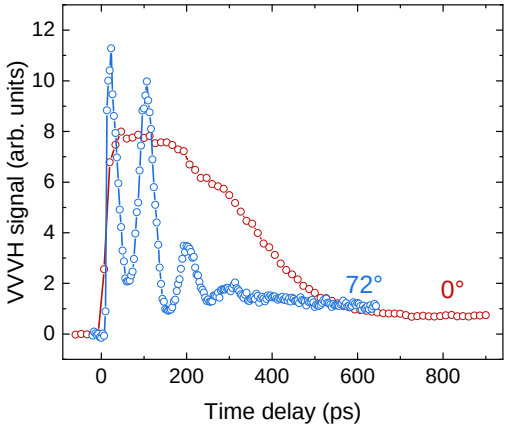

Figure 5.11: VVVH signals acquired at different magnetic field angles. The blue trace is acquired with pump fluence of 18.8 mJ/cm^2, $B_{\text{ext}} = 260$ mT and $\theta_{\text{H}} = 72°$. The red trace is acquired under similar conditions (pump fluence of 19.0 mJ/cm^2 and $B_{\text{ext}} = 220$ mT) but with $\theta_{\text{H}} = 0°$, i.e. with the external field oriented along the easy axis.

differences. At the fluence values used, the situation may be further complicated by additional phenomena, such as all-optical switching [140]. Therefore, these aspects require a dedicated measurement campaign for accurate interpretation.

Fluence dependence

Having demonstrated TG spectroscopy as an effective technique to drive and detect coherent magnons, we investigate the dependence on the laser fluence. Fig. 5.12 shows the experimental data in the 2.7-19.2 mJ/cm^2 range and the best fit (solid line) using equation 5.1. A smoothing of the data (in pink) has been done for the two lowest fluence values; this procedure allowed us to reduce noise and better extract the best-fit parameters. The measured dynamics is clearly dependent on the pump fluence. At low pump fluences (2.7 and 3.1 mJ/cm^2), there is a single overdamped mode (*mode A*). However, at a fluence value of 3.5 mJ/cm^2, a second mode, initially very small in amplitude, appears (*mode B*), becoming more prominent as the fluence increases; to accurately fit this trace, an additional damped sine term was added to Eq. 5.1. However, for pump fluences greater than 6.4 mJ/cm^2, adding a second damped sinusoidal mode to the fitting function leads to the fit failing due to over parameterization; therefore, these traces are fitted using Eq. 5.1. However, the fit does not accurately reproduce the data for $\Delta t < 30$ ps. We interpret this as *mode A* still being excited also at high fluence and affecting the initial part of the dynamics, which prevents the fit using a single damped sine - describing *mode B* - from accurately matching the data at short time delays.

Discussion and comparison with literature

In this section, we will offer an analysis of the trends in amplitude, frequency, phase, and effective Gilbert damping as shown in Fig. 5.13. The parameters for *mode A* are represented in blue, while those for *mode B* in red.
Fig. 5.13.a shows the amplitude trend as a function of fluence shows a progressive in-

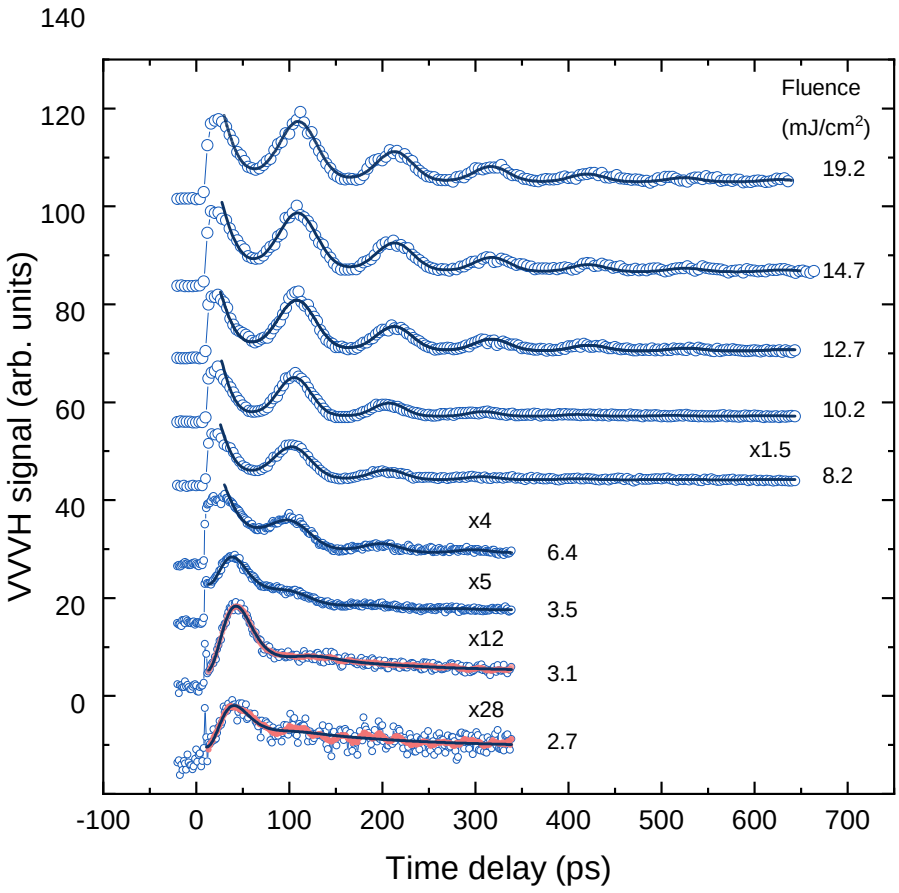

Figure 5.12: *VVVH* signals at different pump laser fluences. Experimental data are reported as open circles and the best fit as solid lines. In pink the smoothing of the data at low fluence. Data in the range 2.7-8.2 mJ/cm^2 are scaled by the reported factor and all the data are vertically spaced for graphical purposes.

crease for both *mode A* and *mode B*. Specifically, *mode B* gradually increases with fluence, experiencing a slight decrease at approximately 10 mJ/cm^2; this trend suggests that by increasing the power *mode B* gets progressively populated and then attenuated by some non-linear effects due to too high fluence.

Fig. 5.13.b depicts the trend of the frequency as a function of fluence. Interestingly, we observe a net increment at $\simeq$ 3.5 mJ/cm^2 for the *mode A*, and a decreasing trend for *mode B*; the phase (Fig. 5.13.c) trend shows an opposite sign for the two modes. This behavior resembles the dynamics around the angular momentum compensation point in similar samples [121, 126, 131, 141]. In particular, given the similarity between our sample and experimental conditions - such as magnetic field configuration, pump wavelength, fluence range, and deposited energy - and those reported in Ref. [121], we can reference their results, specifically those reported in Fig. 5.8.b, to provide insights into the observed trends. Here, no exchange mode is observed. However, given the

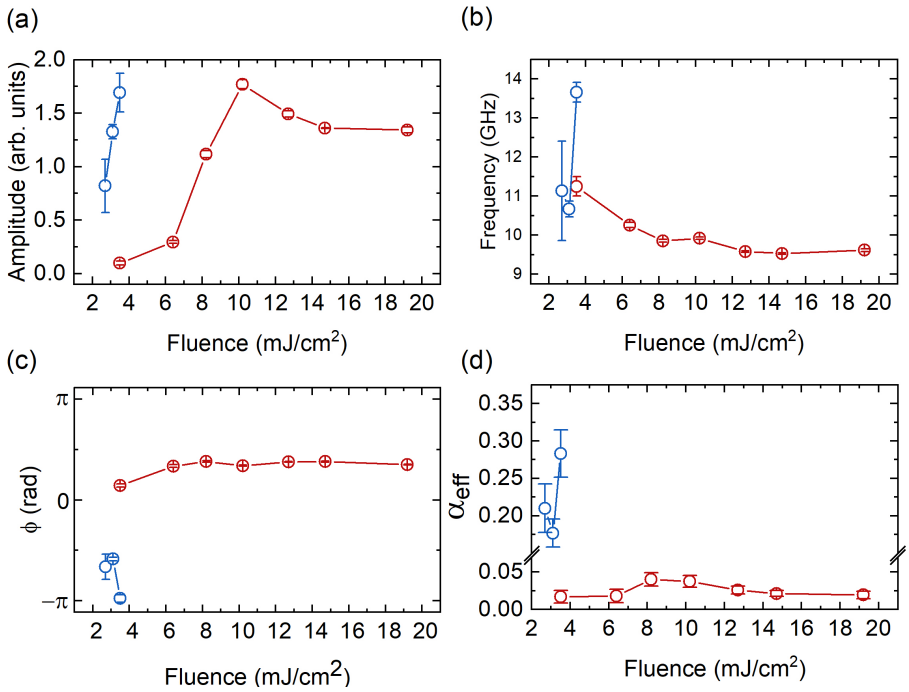

Figure 5.13: (a-c) Best fit parameters: (a) amplitude, (b) frequency (c) phase of the modes. Parameters related to *mode A* and *mode B* are in blue an red, respectively. (d) Calculated effective Gilbert damping α_{eff} as a function of the fluence.

dependence of the frequency on the magnetic field, the fact that we work at very small wavevectors ($\simeq 0$), and the excitation mechanism based on precession dynamics, it is reasonable to compare the frequency trend in Fig. 5.13.b with their results for the FMR mode. At the angular momentum compensation point reached with a pump laser fluence of 3.6 mJ/cm^2 (pumping at 805 nm with a pulse duration of 100 fs), the authors of Ref. [121] observe an increase in the frequency of $\simeq 40$ GHz. Our data do not show such big increase in frequency; however, smaller variations in frequency at the angular momentum compensation point are also reported in the literature (see e.g. Ref. [131]). In any case, this might explain the frequency increase we observe at 3.5 mJ/cm^2, but certainly not the presence of two different modes.

The excitation of *mode A* and *mode B* can be understood in terms of nonhomogeneous excitation. Fig. 5.14 shows a simulation of the energy distribution profile on the sample surface at pump fluences of 3.1, 3.5 and 6.4 mJ/cm^2. At low fluence the energy deposited at the maxima of the interference pattern on the sample surface is not enough to drive the sample beyond the compensation point; however, being anyway close to it, we observe the typical overdamped magnonic behavior experimentally observed also in Ref. [126] by performing polar tr-MOKE. At 3.5 mJ/cm^2, the energy deposited at the TG maxima is enough to bring the system beyond the angular momentum compensation point, causing *mode B* to appear. However, due to the interference pattern on the sample, there will always be regions where the deposited energy is lower, allowing *mode A* to persist. When the pump fluence becomes sufficiently high, causing most of the sample

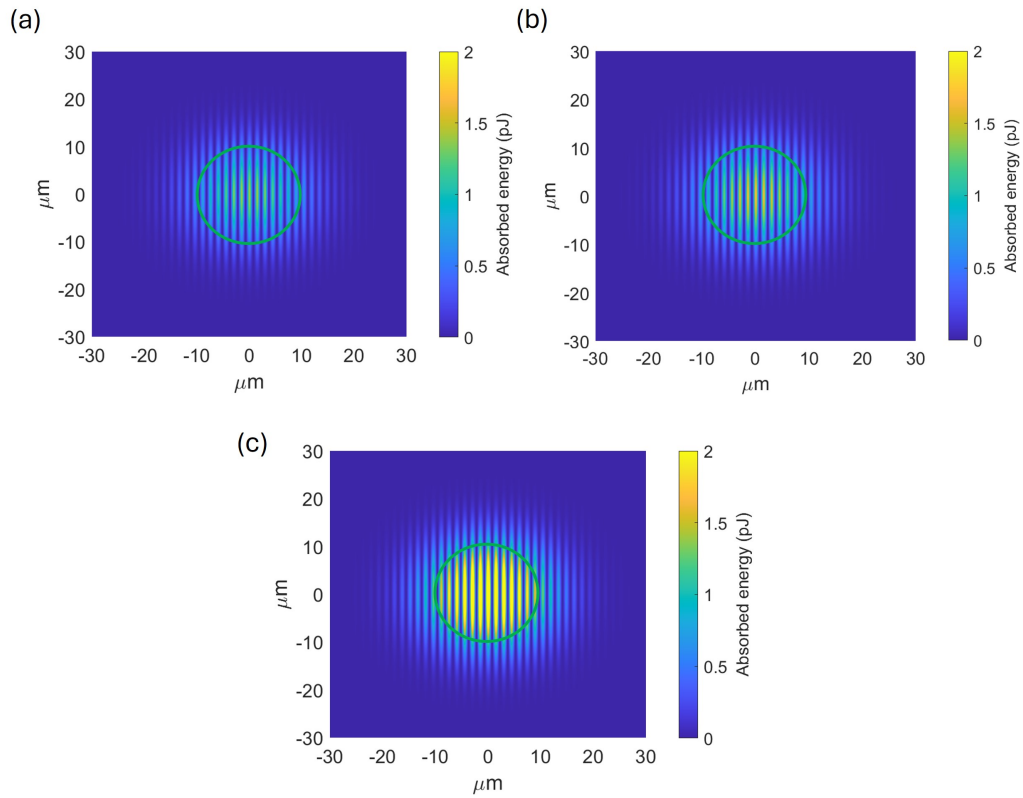

Figure 5.14: Simulation of absorbed energy distribution on the sample surface at (a) 3.1 (b) 3.5 and (c) 6.4 mJ/cm^2. The green circle is a guide for the eye for the probe spot footprint.

to be excited beyond the compensation point, *mode B* dominates over *mode A*, making *mode A* unidentifiable in the traces (and confined at short delays).

The different phase sign shown in Fig. 5.13.c for the two modes support this hypothesis. Crossing the angular momentum compensation point causes the gyromagnetic ratio to change sign [131, 142], with the dominant sublattice determining the direction of gyromagnetic rotation; at the compensation temperature, this dominance shifts from Gd to Co causing a π phase shift in the sense of rotation of the magnetization.

This interpretation is further reinforced by the trend of the Gilbert damping as a function of fluence, which is expected to peak in the neighborhood of the angular momentum compensation point, as also experimentally observed [126, 131]. In a sample with OOP anisotropy in a strong external magnetic field it can be expressed as $\alpha_{\text{eff}} = 1/(2\pi f\tau)$ [141, 143]. However, since the sample is not in saturation, we are rather in a weak field regime. It can be shown that in case of OOP uniaxial anisotropy K_{u} and in the limit of low-wavevector q$\simeq$0, the effective Gilbert damping α_{eff} can be expressed as [144]

$$\alpha_{\text{eff}} = \frac{1}{\tau\gamma\mu_0\left(H_{\text{ext}}\sin\theta_H + \frac{M_{\text{s}}}{2} - \frac{K_{\text{u}}}{\mu_0 M_s}\right)} \tag{5.12}$$

where τ is the decay time of the mode, γ_{eff} is the effective gyromagnetic ratio, $H_{\text{eff}}\sin(\theta_{\text{H}})$

is the IP projction of the external field, K_u the OOP anisotropy constant and M_s the saturation magnetization. The α_{eff} are calculated using the following parameters: the τ as extracted from the time-domain fit, the effective gyromagnetic ratio is calculated from $\gamma_{eff} = \frac{g_{eff}\mu_B}{\hbar}$ with $g_{eff} = 7$ as experimentally extracted from FMR measurements in Ref. [131], $M_s = 10^5$ A/m and $K_u = 3 \cdot 10^5$ erg/cm^3 as reported on Ref. [140]. The values reported in the literature are for nominally identical samples. Fig. 5.13.d shows the obtained α_{eff} values: a clear increase is observed for *mode A*, while for *mode B* the values are < 0.05. The values $\simeq 0.2 - 0.3$ found for the α_{eff} of *mode A* are consistent with what is reported in literature for tr-MOKE measurements performed close to the angular momentum compensation point [126, 131, 141]. We obtain slightly lower values of $\alpha_{eff} < 0.05$ for *mode B*, if compared to the ones reported in the literature for laser-driven FMR in Ref. [126, 131, 141]. This can be attributed to the different excitation mechanisms; however, this aspect requires further investigation in future studies.

It should be noted that this interpretation is compatible with our data and with the literature; to obtain a clearer understanding, more measurements around the critical fluence of 3.5 mJ/cm^2 will allow to better understand the differences between homogeneous (single pump) and heterogeneous (TG pumping) excitation.

5.3.2 Results on Fe/Gd ferrimagnetic multilayers

In this section, we will discuss the main results obtained during a collaborative beamtime[1] access at TIMER@FERMI-FEL in Trieste [69, 78], where TG spectroscopy can be performed in a EUV-pumping optical-probe scheme to validate the TG technique for as a tool coherent magnon spectroscopy also at high wavevectors. Additional details can be found in Ref. [53].

The samples are Fe/Gd multilayers having the structure Ta(2)/[Fe(x)Gd(0.8-x)]×25 /AlOx(2.5), where the values in parentheses denote thickness in nm. The samples were fabricated via sequential sputtering on SiN membranes and both exhibiting Gd-dominated magnetization; however, depending on the Fe layer thickness show different magnetic properties. For a Fe layer thickness of 0.36 nm, the sample exhibits compensated magnetic anisotropy (CMA); namely, the IP anisotropy caused by the demagnetization field is counterbalanced by the PMA at the interface, resulting in a coercive field of 0 mT in both the IP and OOP directions, and a magnetization of approximately $M \simeq 1.8 \times 10^5$ A/m. Note that CMA is different from compensated magnetization. On the other hand, the sample with a 0.38 nm thick Fe layer is closer to the magnetic compensation point and therefore exhibits a lower magnetization. Due to its reduced demagnetizing field, this sample exhibits PMA, with an IP coercive field of approximately $\mu_0 H_{IP} \simeq 300$ mT, an OOP coercive field of $\mu_0 H_{OOP} \simeq 1.5$ mT, and a magnetization of around $M \simeq 10^5$ A/m. Since the Fe and Gd layers are less than 1 nm thick, interlayer diffusion prevents the formation of distinct layers. Although we will continue to use the term "multilayers" to describe the samples, they can be more accurately described as concentration-modulated alloys.

The experimental setup is depicted in Fig. 5.15.a. The two coincident EUV pump pulses with a wavelength of λ_{ex} are crossed at an angle $2\theta_{ex} = 27.6°$, creating a sinu-

[1]Collaborators: A.A. Maznev (PI), N. Bernd, P. Miedaner, J. Deschamps, K.A. Nelson (MIT Chemistry) - F. Bencivenga, L. Foglia, R. Mincigrucci, D. Fainozzi (FERMI-Elettra) - N. Khatu, S. Bonetti (U. Stockholm, U. Venice) - R. Cucini (CNR-IOM, Trieste) - M. Brioschi, P. Carrara, G. Rossi (UniMi, CNR-IOM Trieste) - S. Wittrock, D. Engel, D. Schick (MBI Berlin) - D. Ksenzov, C. Gutt (U. Siegen) - S. Urazhdin (Emory U.) - R. Comin (MIT Physics)

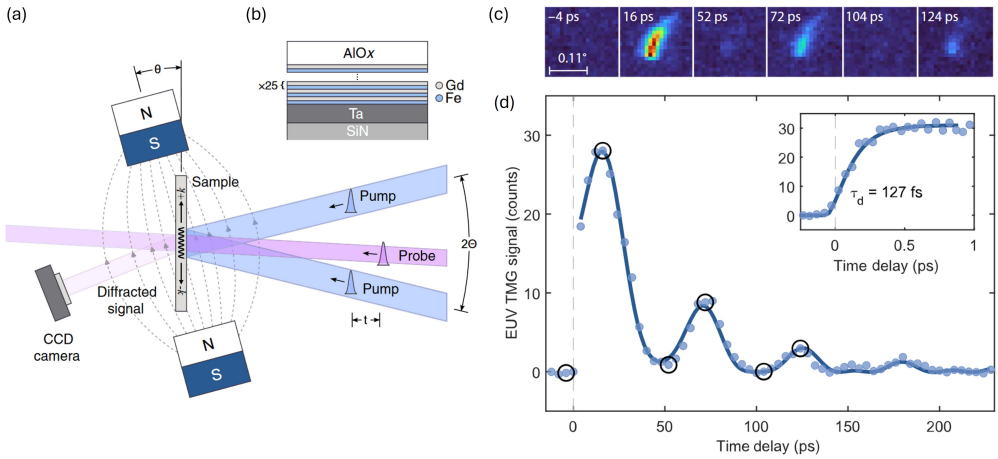

Figure 5.15: Experimental overview. (a) Experimental configuration. Two intersecting EUV pulses (blue) generate counter-propagating spin waves with wave vectors $\pm k$. A time-delayed EUV probe (pink) is diffracted by the spatially periodic modulation of the magnetization, producing a signal on the CCD camera. An external DC magnetic field is applied to tilt the magnetization direction. (b) A Schematic of the Fe/Gd multilayer sample. (c) Examples of CCD images of the diffracted probe intensity at different time delays for the CMA sample at $\Lambda = 52.5$ nm and $\theta_{\mathrm{H}} = 15°$. (d) Integrated signal versus pump-probe delay. Circled points are extracted from the images shown in (c). The solid curve is the best fit obtained with Eq. 5.1. The initial dynamics measured with a 50 fs time step is shown in the inset. Adapted from [53].

soidal intensity profile with a period of $\Lambda = \lambda_{ex}/(2\sin\theta_{\mathrm{ex}})$. The pump wavelength is varied from 8.34 to 41.7 nm, resulting in discrete TMG periods $\Lambda = 17.5, 52.5, 69.9, 87.4$ nm. The dynamics of the transient spatially periodic magnetization pattern induced by the pump pulses are examined through diffraction of a time-delayed probe pulse with a wavelength $\lambda_{pr} = 8.34$ nm, resonant with the $N_{4,5}$-edge of Gd, known for its large MO coefficients [145]. Hence, the detected magnetic signal is specifically sensitive to the Gd spin sublattice. The samples subjected to an external magnetic field of 250 mT, coplanar with the scattering plane, and applied at a variable angle θ_H relative to the sample surface. Fig. 5.15.c and 5.15.d show the data collected from the CMA sample at $\Lambda = 52.5$ nm. The raw data, i.e. CCD images of the diffracted signal, are shown in Fig. 5.15.c, while Fig. 5.15.d shows the integrated signal intensity as a function of the pump-probe time delay. The origin of the signal and its phenomenological description have been described above; the solid line represents the best fit with Eq. 5.1. In this particular case, the setup did not allow for polarization analysis after the sample. However, the thermoelastic response is assumed to be negligible [53]. To confirm the magnonic origin of the observed oscillations, in this case we do not vary the intensity of the magnetic field but rather the θ_{H} angle to examine the dependence of the oscillations on the applied magnetic field. For more information, the interested reader can refer to the full paper [53].

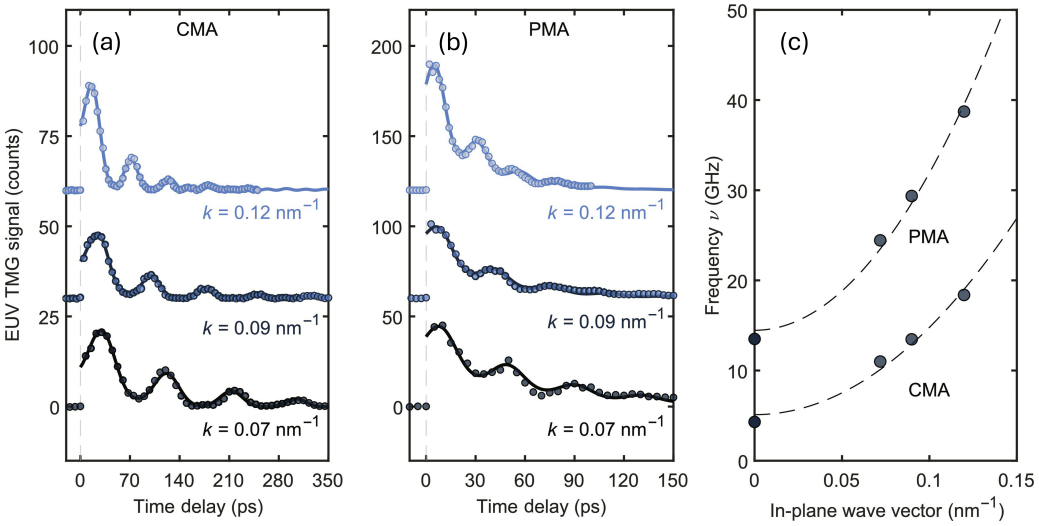

Figure 5.16: Time-domain data for (a) CMA and (b) PMA samples at the labeled wave vectors. Solid curves represent fits. (c) Spin wave dispersions, $\omega(k)/(2\pi)$, for the two samples; dashed curves represent fits by Eq. 5.13. Adapted from [53].

Some experimental results and considerations

To reconstruct the spin-wave dispersion, we use different pump photon energy to excite magnons at the wavevectors $k = 0.12, 0.09$ and 0.07 nm^{-1}, corresponding to TG pitches of $\Lambda = 17.5, 52.5, 69.9, 87.4$ nm. Frequencies of the excited magnons, as extracted from fitting with Eq. 5.1 the time-domain traces shown in Fig. 5.16.a and Fig. 5.16.b, are reported in Fig. 5.16.c as a function of the TG wavevector. The frequencies at $k = 0$ are extracted from tr-Faraday measurements; TG measurements in the optical range would yield similar results since optical pump allow to access wavevector $k \simeq \mu\text{m}^{-1}$, which can be considered approximately zero on this scale of wavevectors. The typical $\omega(k) \propto k^2$ confirm that the magnons we observe are dominated by the exchange interaction. The dispersions are fitted by the ferromagnetic dispersion relation [146]:

$$\omega(k)/(2\pi) = \nu(k) = \Delta + Dk^2 \tag{5.13}$$

where Δ and D are the zone-center magnon gap and magnon stiffness, respectively. For a ferrimagnet, Δ and D are given by Eq. 119 of [146]. The quadratic behavior at high k is characteristic for spin waves dominated by the exchange interaction. The magnon stiffness obtained from the dispersion analysis is $D = 1000$ GHz nm^2 for the CMA sample and 1700 GHz nm^2 for the PMA sample. While there has been extensive research on FMR in RE-TM alloys [121, 131, 147], data on spin-wave dispersion in the exchange-dominated region of these materials is lacking: measurements are typically conducted on thin films, which are not suitable for inelastic neutron scattering. This is just one of the strengths of EUV TG spectroscopy that is likely to play a big role in the investigation of magnons with wavelengths down to the 100-nm range (or even below), which are particularly appealing for spintronics applications.

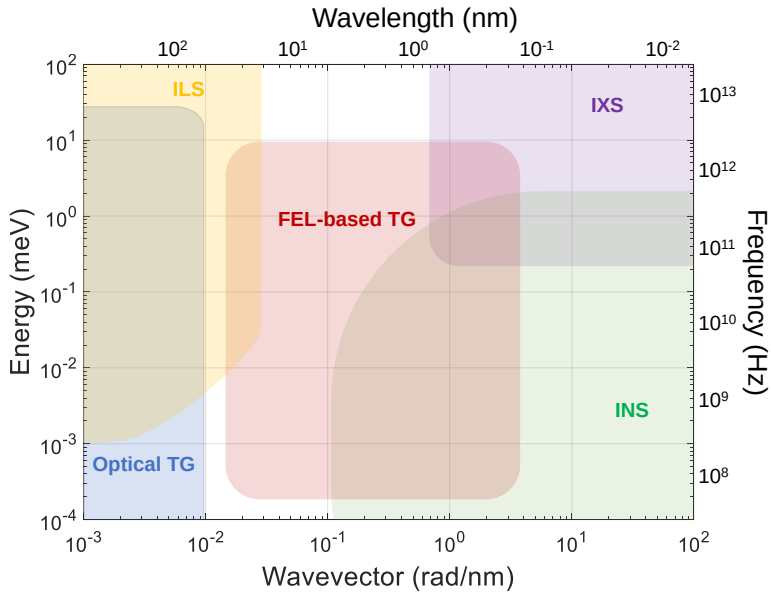

Figure 5.17: The typical range of accessible frequencies and wavevectors for FEL-based TG and various inelastic scattering techniques, all of which are also capable of magnetization-sensitive detection. The diagram includes: ILS (Inelastic Light Scattering, such as Brillouin and Raman), IXS (Inelastic X-ray Scattering), and INS (Inelastic Neutron Scattering).

5.4 Conclusions

In this chapter, we have shown complementary results on magnon spectroscopy, which allow in principle to excite coherent magnon at any possible wavevector within the limitations of the experimental setups. This is *per se* relevant since the investigation of spin waves at a selected wavevector typically requires the fabrication of specific nanostructured samples. In the optical range, we demonstrated that the approach implemented by Cao et al. [74] in a Lorentz microscope can also be implemented in an all-optical tabletop setup. We have demonstrated results on a sample exhibiting PMA, but the principle can be extended to all magnetic samples by appropriately tuning the magnetic field's direction and intensity. Furthermore, the interpretation of the fluence scan, although it still needs to be refined with further measurements, provided a first insight to the application of TG spectroscopy to the study of the coherent dynamics originating from periodically pumping the system above critical points - e.g. the angular momentum compensation point in ferrimagnets - or locally induce phase transitions.

Although EUV transient grating spectroscopy has been extensively used to probe coherent phonons, the potential of EUV radiation to study nanoscale spin waves has not yet been fully realized. Here we show how this method allows the study of spin waves in a range of wave vectors beyond the reach of other available inelastic scattering techniques, as depicted in Fig. 5.17. Here, we have shown the excitation of coherent magnons via EUV TG in Fe/Gd multilayers. The possibility of performing measurements over a wide wavevector range allowed the reconstruction of the spin wave dispersion and extraction of physical parameters, such as the spin wave stiffness. Overall, the

results demonstrate the potential of EUV radiation for studying magnons and introduce EUV transient gratings as a tool for high-wavevector coherent magnon spectroscopy, providing the means to broaden our understanding of ultrafast magnetic dynamics at the nanoscale and to advance research toward high-speed magnonic devices.

Part III

Magnetization dynamics in Fe_5GeTe_2

CHAPTER 6

Magnetization dynamics in Fe_5GeTe_2

Two-dimensional (2D) magnetic van der Waals (vdW) materials, such as $Fe_{5-x}GeTe_2$ ($0 < x < 2$), have garnered significant attention due to their promising magnetic properties, including magnetic anisotropy and T_c approaching room temperature, making them highly appealing for spintronics applications [148].

In recent years, the static properties of $Fe_{5-x}GeTe_2$ have been extensively studied, ranging from single-crystal bulk to nanoflakes [148–152]. Promising results on these compounds have also been achieved on the manipulation of magnetic properties and phases by applying external stimuli, e.g voltage [153–155], strain[156] or doping [157, 158]. Furthermore, several studies have explored heterostructures involving $Fe_{5-x}GeTe_2$ compounds designed to achieve properties potentially beneficial for device applications (see e.g. Refs. [159, 160]).

$Fe_{5-x}GeTe_2$ compounds have been extensively studied at equilibrium. However, to better understand the properties of these materials, it is essential to investigate their dynamical behavior, e.g. the recovery of the ground state after sudden excitation using all-optical methods, which has not yet been thoroughly explored. Ref. [161] presents a study on demagnetization dynamics using all-optical pump-probe spectroscopy in Fe_3GeTe_2 (F3GT). There are no reports in the literature insofar on coherent magnetization dynamics using all-optical techniques. Such studies are indeed challenging because of the strong coercive field and significant magnetic anisotropy of F3GT. In contrast, coherent magnetization dynamics in Fe_5GeTe_2 (F5GT) has been studied using B-FMR, including temperature-dependent investigations [162, 163]. We have shown above that to achieve direct insights into the magnetic dynamics, a stroboscopic approach is required.

This chapter presents the results of our systematic investigation of magnetization dynamics in an F5GT thin film as a function of the applied magnetic field ($\mu_0 H_{\text{ext}} = B_{\text{ext}} <$ 60 mT) across a temperature range of 100 K$< T <$290 K. To date, no studies reported in the literature have explored coherent magnetization dynamics in this family of samples using tr-MOKE: our investigation aims to fill this gap. In particular, we characterize the Kittel mode at different external magnetic fields and T, and we extract values of effective Gilbert damping α_{eff}, magnetization M_{eff} and anisotropy K_{eff} at different T.

These results, made possible by the capabilities of the experimental chamber described in Sec. 3.4, do provide valuable insight into the magnetization dynamics of F5GT. Furthermore, they provide evidence that our approach could be effectively applied to study magnetization dynamics in this class of materials and systems, such as F3GT and F4GT, or FGT-based heterostructures.

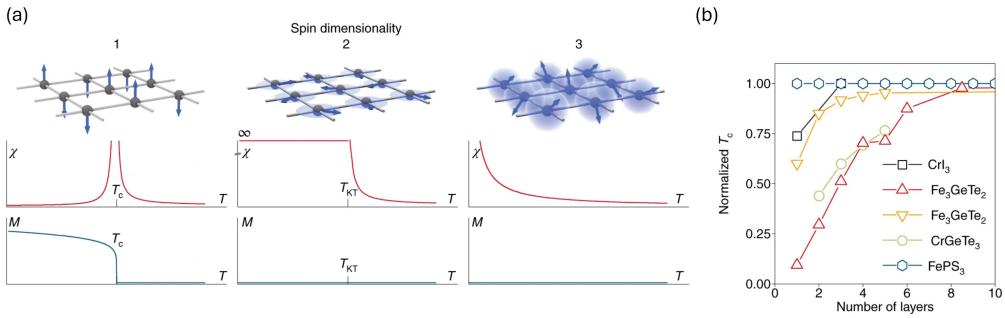

Figure 6.1: (a) A system with spin dimensionality of n= 1 exhibits strong uniaxial anisotropy, with spins confined to two possible orientations ('up' or 'down') along a specific axis. This effectively reduces the system to having only one spin component along the easy axis, and the corresponding spin Hamiltonian for localized spins is described by the Ising model. In the case of n = 2, the system has easy-plane anisotropy, which favors the spins to align within a particular plane, although their orientation within that plane is unrestricted. As a result, the spins are considered to have only two effective components (corresponding to the two in-plane directions), which are described by the XY model. It is important to note that for $T < T_{\mathrm{KT}}$, the susceptibility χ tends to infinity. Lastly, in isotropic systems with n = 3, there are no constraints on spin direction, and the spin Hamiltonian is represented by the isotropic Heisenberg model. (b) Plot shows of critical temperature T_c (normalized to the bulk T_c^{3D} of the material) as a function of the number of layers. Adapted from [164]

6.1 Sample details

2D Van der Waals materials

2D materials are a class of materials composed of stacks of strongly bonded atomic layers weakly connected by van der Waals (vdW) forces. These materials are typically just a few atomic layers thick, sometimes reduced to a single layer, which gives them unique electronic, optical, and mechanical properties. The most well-known example of a 2D material is graphene, a single layer of carbon atoms arranged in a hexagonal lattice. Since the discovery of graphene, research has expanded to include a variety of 2D materials with diverse characteristics, including semiconductors, insulators, and superconductors. However, the existence of magnetic 2D materials posed an intriguing challenge, particularly due to the Mermin-Wagner theorem [165]. This theorem predicts that in 2D systems with continuous symmetries, such as isotropic magnetic systems, long-range magnetic order cannot exist at finite temperatures because thermal fluctuations would destroy it. For years, this prediction led to the assumption that magnetism could not be sustained in atomically thin layers. Despite this, certain symmetry reduction mechanisms - such as magnetic anisotropy or SOC - can break the continuous symmetry and stabilize magnetism in 2D materials, overcoming the limitations imposed by the Mermin-Wagner theorem. This theoretical possibility paved the way for research into 2D magnetic materials [164, 166, 167].

Before 2017, the absence of known 2D magnetic materials was surprising, especially given the well-known existence of layered magnetic crystals held together by vdW forces. The breakthrough came with the discovery of intrinsic magnetism in a CrI_3 monolayer [168], which built up momentum in the study of 2D magnetic materials, with exciting

perspectives in fields like spintronics, magnonics, and quantum computing.

2D vdW materials possess several unique properties that make them peculiar compared to bulk three-dimensional (3D) crystals, primarily due to their spin dimensionality effects, as schematically depicted in Fig. 6.1 [164, 166]. One key feature is the ability to stack few-layer crystals to form vdW heterostructures with tailored functionalities. These few-layer crystals are highly sensitive to their local environment, and proximity effects where one layer influences the behavior of an adjacent layer have emerged. For example, proximity-induced SOC has been observed in graphene on WS_2 [169], while the anomalous Hall effect and Zeeman spin Hall effect have been detected in graphene on thin films of magnetic insulators such as yttrium iron garnet (YIG) and EuS [170].

Despite significant progress in understanding and exploring potential applications of 2D magnetic materials, several challenges persist. One major challenge is increasing the T_c of 2D magnetic materials to or above room temperature, which would be crucial for applications like spintronics. Further research is needed to discover new materials with strong exchange interactions and improve the thermal stability of magnetic order. Additionally, significant improvements are still needed in developing scalable synthesis methods to produce high-quality atomic layers over large areas. While mechanical exfoliation has been effective for small-scale research, it is not scalable; alternatives such as chemical pulsed laser deposition (PLD) [171], chemical vapor deposition (CVD) [172], molecular beam epitaxy (MBE) [173] offer promising pathways. Finally, ensuring the chemical stability in ambient conditions is critical for the long-term reliability of devices. Metallic 2D magnetic materials degrade in the presence of air and moisture (e.g. VI_3), leading to a loss of magnetic properties. Therefore, passivation and encapsulation techniques are required to protect these materials from environmental exposure. The interested reader can explore the topic further in Ref. [166].

$Fe_{5-x}GeTe_2$ compounds

The $Fe_{5-x}GeTe_2$ family of compounds, with typical values of $0 < x < 2$, has attracted considerable attention in materials science due to its unique combination of structural, magnetic, and electronic properties. Recent advances have demonstrated the successful growth of high-quality $Fe_{5-x}GeTe_2$ compounds using MBE [173]. These samples are generally not very stable in air and require capping to avoid surface oxidation; however, they remain in the solid state under ambient conditions.

The number and specific arrangement of Fe and Ge atoms, together with the presence of iron vacancies, greatly influences the magnetic properties of the $Fe_{5-x}GeTe_2$ compounds [174], which ultimately determine their suitability for various technological applications. They crystallize in a hexagonal structure, where the Fe and Ge atoms are sandwiched between two layers of Te atoms [173]. This arrangement corresponds to strong IP bonding and weak OOP vdW interactions. However, F5GT contains additional Fe atoms, creating a more complex lattice configuration than F3GT, as illustrated in Fig. 6.2 [149, 173]. A monolayer of Fe_5GeTe_2 consists of six atomic layers of Fe stacked together; four of these layers are fully occupied, while the remaining two have only 50% of occupancy [173]. The termination of the structure with Te atoms contributes to the system's ferromagnetism with its strong SOC. Unlike 2D ferromagnets such as CrI_3 - or F3GT [150] - where magnetic atoms are confined to a single plane, F5GT features 3D network of magnetic atoms. This configuration results in 3D interlayer exchange interactions, which explain the observed 3D magnetic behavior and higher T_c [149, 173].

In F5GT thin films thicker than a few monolayers (ML), the Curie temperature (T_c)

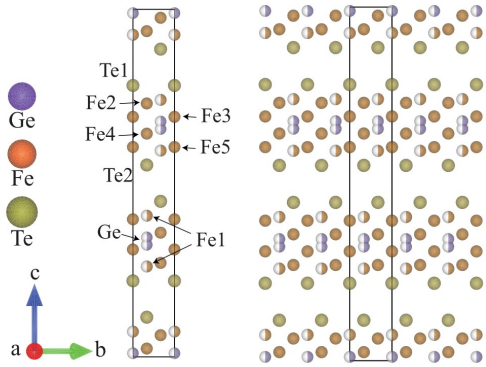

Figure 6.2: The unit cell is shown in projection along the [100] direction, highlighting the F5GT layers, which are separated by a vdW gap between adjacent Te sublayers. The panel on the right depicts the same projection for multiple repetitions of the unit cell. The occupation probability of certain atomic sites is illustrated using half-filled solid spheres. Adapted from [173].

approaches that of the bulk material, around 300 K. This higher T_c makes F5GT more suitable for high temperature applications compared to F3GT, which has a lower T_c of approximately 230 K [149, 173, 175]. F3GT displays strong uniaxial magnetic anisotropy, with the easy magnetization axis aligned along the c-axis (OOP) [176]. In contrast, F5GT shows weak OOP anisotropy; however, the stronger IP shape anisotropy leads to an overall IP effective anisotropy, especially in thin films. [155, 173]. In both F3GT and F5GT, the magnetic anisotropy and coecitivity increase as the temperature decreases [173, 176].

6.2 Experimental results

In this section, we present experimental data on an 8.8-nm-thick - or 9 ML-thick - F5GT sample, based on systematic measurements aimed at investigating its magnetic dynamics as a function of temperature and applied magnetic field.

This sample has a temperature-dependent coercive field H_c, saturation field H_s and saturation magnetization M_s. Hysteresis loops acquired via longitudinal (static) MOKE (i. e. with an IP external field) are reported in App. C, along with details on the growth of the sample. Hysteresis loops show a $T_c \simeq 290$ K and IP magnetic anisotropy at all temperatures explored. The F5GT thin films have weak OOP uniaxial anisotropy $K_u > 0$ and stronger shape anisotropy $K_d < 0$; therefore, the effective anisotropy $K_{eff} = K_u + K_d < 0$ favors IP magnetization [173]. It is important to note that the measured values of H_c and H_s with an IP field set a lower limit for our system: in our geometry we can expect higher H_c and H_s due to the OOP component of the applied magnetic field [173].

This section is organized as follows: first, we will introduce the technical experimental details, followed by considerations on the expected active magnetic modes. Finally, we will present the experimental results; specifically, we will discuss the data obtained at a fixed temperature of T =220 K, followed by a systematic analysis of the data acquired at different temperatures.

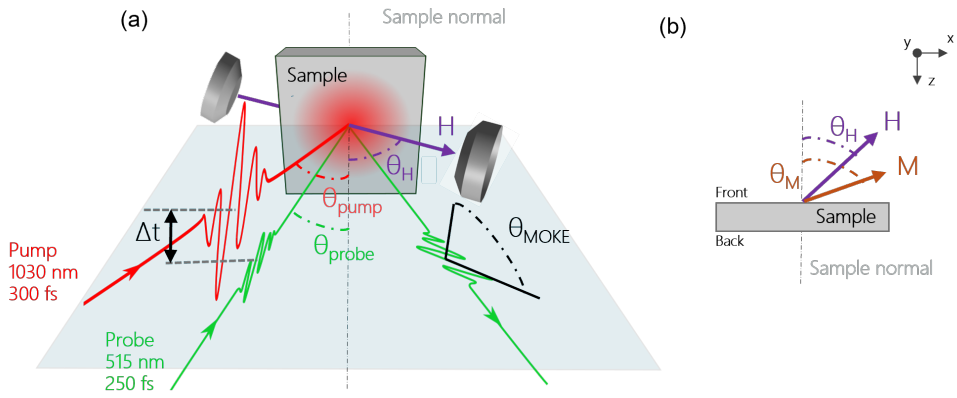

Figure 6.3: (a) Front view end-station of our tr-MOKE setup. The s-polarized pump (probe) beam impinges on the sample at an angle $\theta_{\text{pump}} = 12°$ ($\theta_{\text{probe}} = 6°$) to the sample surface normal; Δt is the time-delay between pump and probe. Due to the MOKE effect, the reflected beam exhibits a rotation of the polarization θ_{MOKE}. The sample is positioned in the vertical (x, y) plane, with the external magnetic field H coplanar with the scattering plane and at an OOP angle $\theta_H = 55°$ to the sample surface normal. (b) Top view of the sample. θ_M is the equilibrium angle of the magnetization when the external field is applied, determined by the sum applied external magnetic field and magnetic anisotropy field.

6.2.1 Setup and experimental details

The experimental setup is derived from the TG setup described in Ch. 3, with minor adjustments: by blocking one of the pump beams and capturing the reflected probe signal from the sample, the TG setup is transformed into a tr-MOKE spectro-magnetometer. The layout of the optical end station and the experimental geometry are shown in Fig. 6.3; the sample environment is implemented within in the UHV chamber described in Sec. 3.4, enabling measurements also at low temperature. The sample lies in the (x, y) plane, with its normal along the z-axis. The s-polarized pump and probe beam impinges on the sample at an angle of $\theta_{\text{pump}} = 12°$ and $\theta_{\text{probe}} = 6°$ with respect to the normal to the sample surface, respectively; since the angle of incidence of the probe beam is slightly off-normal, the set-up is mostly sensitive to the OOP component of the magnetization (M_z). The laser spot size (FWHM) on the sample is approximately 65 × 53 μm^2 for the pump and 30 × 26 μm^2 for the probe, with the slight ellipticity resulting from the off-normal incidence of the beams. Unless otherwise stated, the pulse energy is set to 13 nJ/pulse for the pump and 1 nJ/pulse for the probe, corresponding to average fluences of around 0.5 mJ/cm^2 and 22 µJ/cm^2, respectively. The effective laser repetition rate was set at 100 kHz for all measurements. Given that the F5GT compounds exhibit IP anisotropy, the external magnetic field $H_{\text{ext}} = \mu_0 B_{\text{ext}}$ was applied coplanar to the scattering plane, at an angle of $\theta_H = 55°$ relative to the sample surface normal. This configuration is chosen to employ the same excitation scheme as described in Sec. 5.1.

6.2.2 What is expected?

In all-optical pump-probe experiments, the pump pulse drives the magnetization out of equilibrium within the optical penetration depth δ. Different magnetic precession modes arise depending on the thickness of the ferromagnetic layer as the combination of the applied magnetic field, the exchange field, and/or dipole field reorient the magnetization axis [17, 120]. Since a direct measurement of the complex refractive index of FGT is not available in the literature, and Fe is the most abundant element in the F5GT compound, we approximate the lower limit of the penetration depth at 1030 nm using the Fe absorption coefficient α_{Fe}. Thus, we estimate $\delta_{\text{F5GT}} \simeq \delta_{\text{Fe}} = 1/\alpha_{\text{Fe}} \simeq 20$ nm; the value of α_{Fe} is sourced from the *refractiveindex.info* database [177]. However, δ_{F5GT} will be realistically longer. This is further supported by findings in Refs. [178, 179], which report penetration depths in the range of 40–50 nm for $Cr_2Ge_2Te_6$, which is another 2D vdW Germanium Telluride compound. In any case, being the thickness of the sample at least a factor two smaller than the lower limit of the penetration depth, we can assume that the whole sample is uniformly excited directly by the pump laser pulse. In this condition, we expect to observe the Kittel mode only [17, 120]. However, the effective magnetic field is neither fully IP nor OOP, and this must be considered in the functional dependence of the frequency on the applied magnetic field. By solving the LLG equation in spherical coordinates in the case of an applied magnetic field at an angle θ_H with respect to the sample normal, it can be shown [120] that the Kittel formula can be written as

$$f = \frac{\gamma\mu_0}{2\pi}\sqrt{H_{\text{ext}}\sin\theta_H\,(H_{\text{ext}}\sin\theta_H + M_{\text{eff}})}. \tag{6.1}$$

As discussed above, the typical tr-MOKE signal consists of an exponential decay superimposed by coherent damped oscillations. Since we expect to trigger only the Kittel mode, the tr-signals can be fit with a sinusoidal term superimposed on an experimental background (see Eq. 6.4) describing coherent and incoherent contributions to the magnetization dynamics, respectively. The decay time τ_1 of the Kittel mode is a key parameters to calculate the effective Gilbert damping α_{eff}, which can be quantified as [120, 180]

$$\alpha_{\text{eff}} = \frac{1}{\tau_1\gamma\mu_0(H_{\text{ext}}\sin\theta_H + M_{\text{eff}}/2)} \tag{6.2}$$

where M_{eff} is obtained by fitting $f(H_{\text{ext}})$ with Eq. 6.1.

Finally, the effective anisotropy $K_{\text{eff}} = K_u + K_{\text{d}} < 0$ can be calculated from M_{s} and M_{eff} as

$$K_{\text{eff}} = \frac{\mu_0 \cdot M_s \cdot (M_s - M_{\text{eff}})}{2} \tag{6.3}$$

6.2.3 Magnetization dynamics at 220 K

Fig. 6.4 shows the tr-MOKE traces for the 9ML Fe_5GeTe_2 sample, acquired by scanning the applied magnetic field from $\simeq$ 50 mT to $\simeq -50$ mT, with a step size of $\simeq$ -7 mT. The negative sign in the external magnetic field step size emphasizes that the applied field is swept from positive to negative values. The solid lines represent the best fit to the data using

$$\mathcal{S}(t>0) = a_0\exp^{-t/\tau} + a_1\exp^{-t/\tau_1}\sin(2\pi f + \phi) + c \tag{6.4}$$

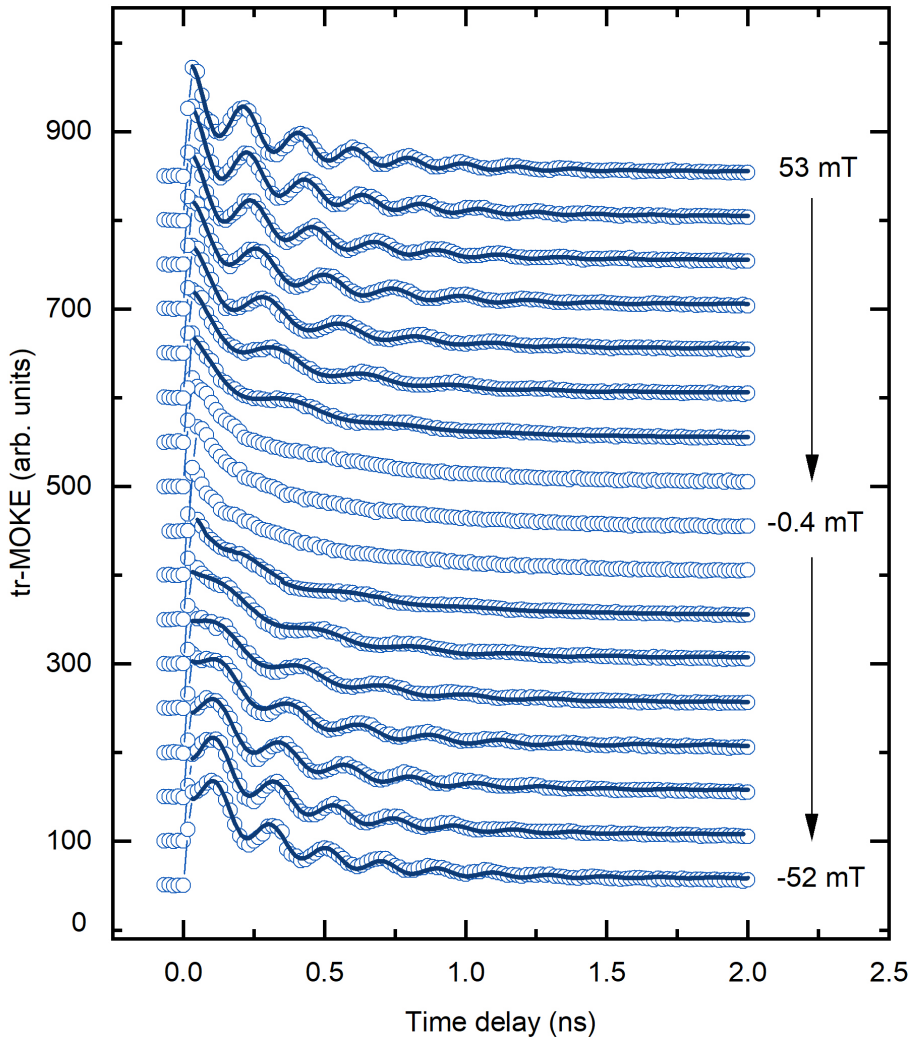

Figure 6.4: tr-MOKE traces acquired scanning the applied magnetic field from 53 mT to -52 mT with $\simeq -7$ mT step. The solid line represents the best fit to the data using Eq. 6.4. The traces are vertically translated for graphical purposes.

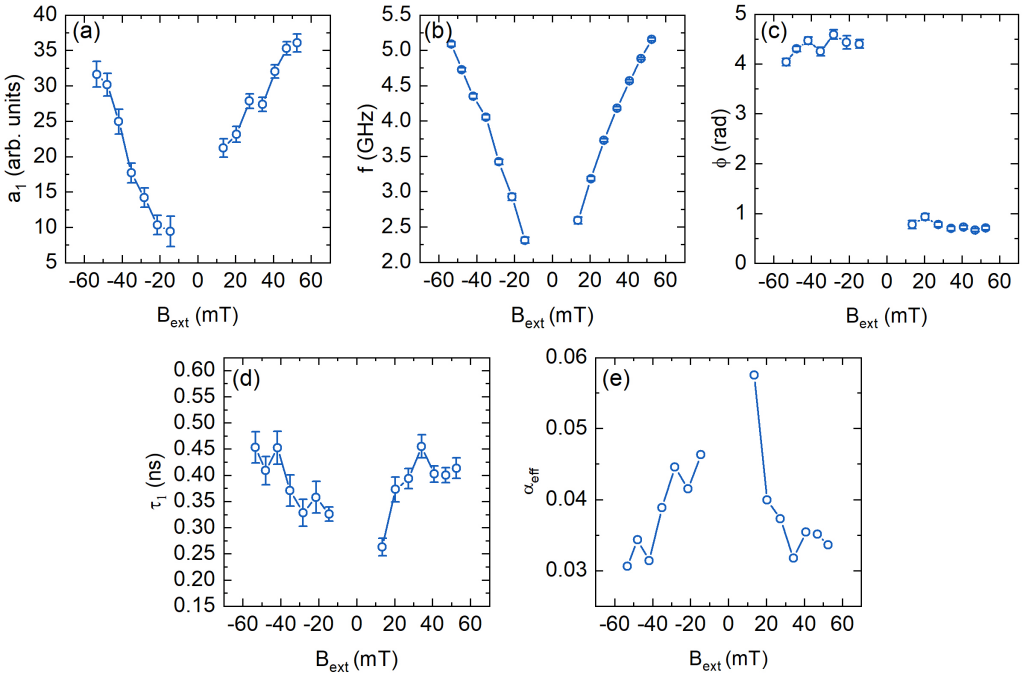

Figure 6.5: Best fit parameters of the tr-MOKE traces presented in Fig. 6.4. (a) Precessional amplitude (b) precessional frequency (c) phase (d) relaxation time (e) effective Gilbert damping calculated from Eq. 6.2.

The best-fit parameters are reported in Fig. 6.5 as a function of the external magnetic field. The coherent dynamics show a clear dependence on the magnetic field; however, despite following the expected exponential decay, the incoherent contribution does not depend on the intensity or direction of the applied magnetic field, suggesting a non-magnetic origin; therefore, it will not be discussed below.

Fig. 6.5.(a-d) shows the trend of the precession amplitude (a_1), frequency (f), phase (ϕ), decay constant (τ_1) and effective Gilbert damping (α_{eff}) as a function of the applied magnetic field $B_{\text{ext}} = \mu_0 H_{\text{ext}}$. As expected, the amplitude of the precession increases with increasing B_{ext} [181, 182]. For $B_{\text{ext}} \lesssim 20$ mT, no oscillation amplitude is observed, likely due to the presence of magnetic domains limiting the tr-MOKE contrast. By increasing the external field from $\simeq 0$ to $\simeq 50$ mT, the frequency of the laser-driven magnetization precession frequency ranges from 2.5 to 5 GHz, following the trend described by the Kittel formula. Furthermore, when the applied magnetic field is reversed, the phase shifts by approximately π. This shift occurs because the equilibrium axis of the magnetization flips, resulting in an opposite sense of precession and M_z component, as schematically illustrated.

The relaxation time increases by $\simeq 50\%$, while α_{eff} has an opposite trend. It should be specified that the calculation of α_{eff} has been performed by using Eq. 6.2 with $\gamma/(2\pi) = 2.9$ GHz/kOe and $M_{\text{eff}} = 560 \pm 3$ kA/m, which is the value found by fitting the frequency trend with the Kittel formula, as will be shown in the next section. The error on α_{eff} is obtained propagating the errors of τ_1 and M_{eff}. The increase of τ_1 can be attributed to the presence of magnetic domains [182], which, at this temperature and with the applied

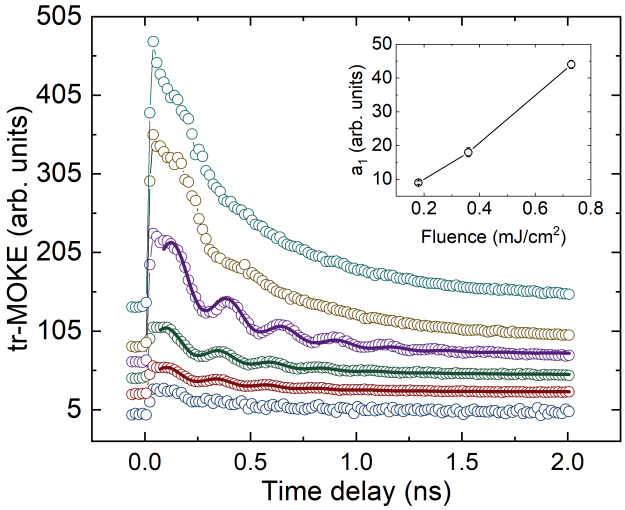

Figure 6.6: tr-MOKE traces at different pump fluence; from bottom to top 0.04, 0.18, 0.36, 0.73, 1.84 and 2.58 mJ/cm^2 for all traces. The probe fluence is set at 22 µJ/cm^2. The inset shows the trend of the amplitude of coherent precession, as obtained by the best fit (solid lines).

magnetic field oriented at $\theta_{\mathrm{H}} = 55°$, appear to persist until the applied magnetic field intensity reaches 30 mT. This observation aligns with the measured hysteresis loops reported in App. C and with the results presented in Ref. [173] for similar samples, which show an increase H_{s} as θ_H decreases. Based on the discussion so far, $H_{\mathrm{c}} \simeq 20$ mT and $H_{\mathrm{s}} \simeq 30$ mT appear as consistent values; however, these still need to be confirmed by additional measurements and/or simulations.

α_{eff} includes both the intrinsic damping α and additional contributions, such as those arising from magnetostructural disorder and spatial variations of the anisotropy field. When the applied magnetic field increases, α_{eff} approaches α [182, 183]. In our case, α_{eff} stabilizes at approximately 0.03 for $|B_{\mathrm{ext}}| > 30$ mT, which can be considered close to α since a similar value is reported in the literature for a single crystal bulk sample [162] at a similar temperature. The value we obtain is quite big with respect to the one reported for instance for Fe (10^{-3}, see e.g. Ref. [184]) or YIG (10^{-5}, see Ref. [185]). A possible explanation for the relatively high value of α_{eff} is the strong SOC resulting from band hybridization with Te atoms. This is attributed to the high atomic number of Te $Z_{\mathrm{Te}} = 52$, as SOC scales approximately with Z^4.

Finally, at $B_{\mathrm{ext}} = 35$ mT, we investigate the laser fluence dependence behavior of the tr-MOKE signal. Fig. 6.6 shows different traces acquired at different pump fluences. No oscillations are observed at 0.04 mJ/cm^2; when the pump fluence is set in the range 0.18-0.73 mJ/cm^2, the coherent dynamics is clear and the precession amplitude linearly increases with the fluence. This trend is expected in the "low-fluence regime", where the precession amplitude increases; however, at higher fluence, the decrease in the effective anisotropy field dominates, leading to a reduction in the amplitude, as for example observed in Ref. [182]. We do not observe this trend in our dataset, perhaps because of coarse fluence sampling. In the "high-fluence regime", at 1.84 mJ/cm^2 and 2.58 mJ/cm^2, a weak oscillatory behavior is observed; however, the best fit with Eq. 6.4 fails. We interpret this as the disappearance of coherent dynamics. Additionally, the smaller increase at

high fluence in the exponential background suggests that the sample may begin to experience a non-linear regime as it approaches the damage threshold [186]. This conclusion is supported by the fact that after measuring at the highest fluence, by reducing the fluence we recovered the signal of the "low fluence" regime. However, this high-fluence non-liner regime deserves further investigation.

6.2.4 Magnetization dynamics at different temperatures

We investigated the magnetization dynamics also as a function of temperature.

Fig. 6.7.a shows tr-MOKE traces acquired at an external applied field of $B_{\text{ext}} = 53$ mT in a temperature range of 80-290 K. We observe no detectable dynamics at $T = 290$ K and $T = 80$ K. In the first case, this is attributable to the proximity of the nominal T_c, which implies reduced M_s and consequently lower magnetic contrast. Following the same procedure adopted above, we fit the time-domain traces with Eq. 6.4, that approximates the data fairly well; the best-fit parameters are reported in Fig. 6.7.b-e.

In the temperature range of 270–100 K, we observe an increase in frequency of approximately 3.5 GHz. This trend can be readily explained by the increase in M_{eff} as the temperature decreases, an interpretation that is consistent with Eq. 6.1 and our findings shown in Fig. 6.9.c. An explanation for the observed decrease in amplitude reported in Fig. 6.7.c is provided in the following section. Furthermore, we observe a general decrease of α_{eff}, calculated with Eq. 6.2 using the M_{eff} values reported in Fig. 6.9.b. Indeed, at lower temperatures, the reduction in thermal agitation and scattering processes leads to less energy dissipation in the spin reservoir, which manifests as lower α_{eff}.

Similarly to what has been shown for $T = 220$ K, we conducted a scan of the applied magnetic field at a fixed temperature. Fig. 6.8 summarizes our results, presenting 2D colormaps that illustrate the behavior of the parameters as a function of both temperature and applied magnetic field. In the "low-field" and "low-temperature" regions, where no precessional dynamics are observed, the parameter values have been set to zero. The general trends discussed above can be easily recognized.

Finally, we focus on the trend of the precessional frequency as a function of the applied magnetic field. Fig. 6.9 displays the measured values. The solid lines are the best fit to the data using Eq. 6.1. In the fitting process, we assume $\gamma/(2\pi) = 0.0029$ GHz/Oe $= 29$ GHz/T, as reported in Ref. [187] for a similar experimental setup. Other values reported in the literature - such as in Ref. [162, 163] - are not significantly different. We extract a value of M_{eff} at each temperature, as reported in Fig. 6.9.b along with the corresponding K_{eff} values. The K_{eff} values have been calculated using Eq. 6.3 and the M_s values extracted from literature; specifically, we used the M_s values shown in Fig. 6.9.b, which are extracted from the magnetic characterization of a 12-nm-thick thin film grown by the same procedure reported in Ref. [173]. Unexpectedly, at $T = 250$ K, we observe a small OOP anisotropy. In contrast, within the $220 - 120$ K range, there is a noticeable increase in IP anisotropy, though it remains an order of magnitude smaller than that reported in Ref. [173] for the 12-nm-thick Fe_5GeTe_2 thin film. It is worth mentioning that the values of K_{eff} are only estimates. We believe a more detailed analysis, including direct measurements of K_{eff} for this specific sample, is necessary to obtain more reliable values.

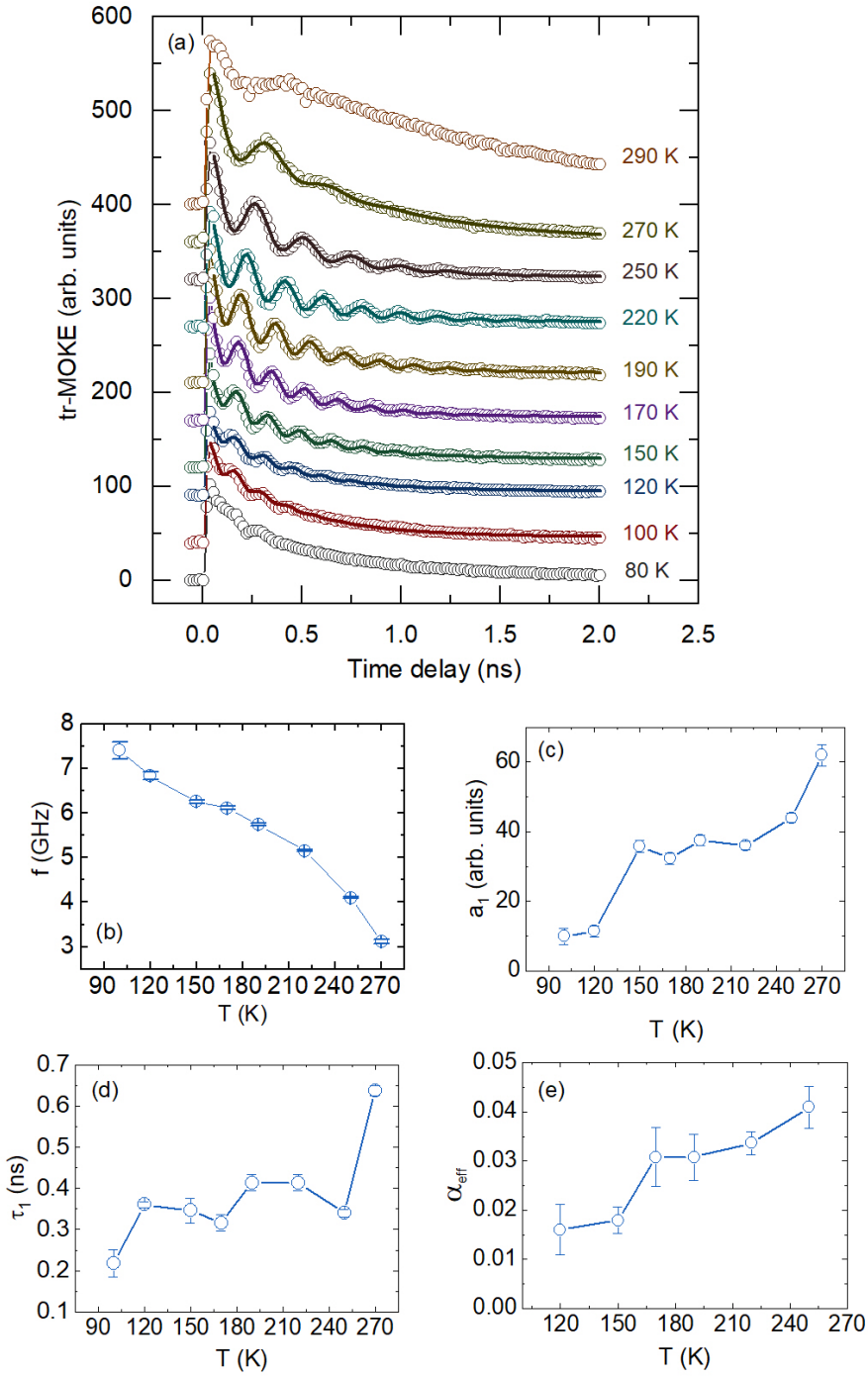

Figure 6.7: (a) tr-MOKE traces at different temperatures. Solid lines are the best fit to the data. The traces are vertically shifted for graphical purposes. Trend of (b) frequency, (c) amplitude, (d) decay time and (e) α_{eff} as a function of temperature.

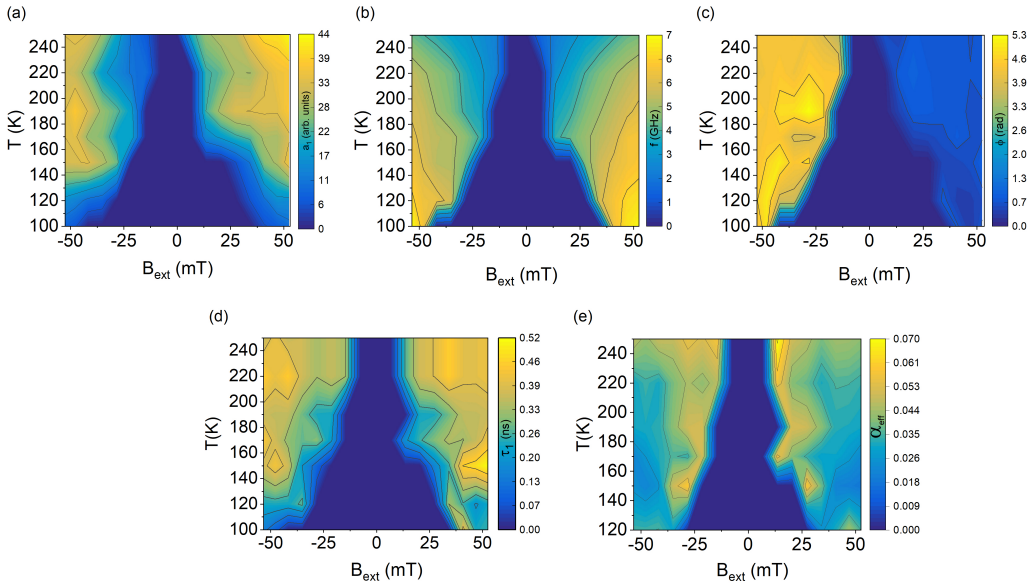

Figure 6.8: Temperature and external magnetic field dependence of precessional (a) amplitude (b) frequency (c) phase (d) decay time (e) α_{eff}.

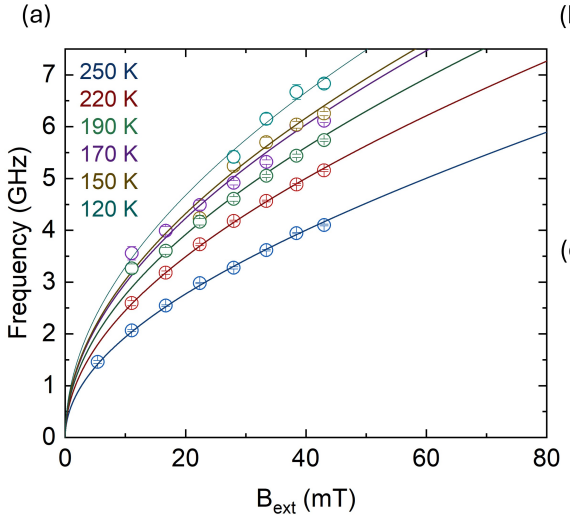

(b)

T (K)	M_{eff} (kA/m)	M_s (kA/m)	K_{eff} (J/cm^3)
250	347 ± 3	400	0.013 ± 0.001
220	560 ± 3	465	-0.028 ± 0.001
190	710 ± 18	515	-0.063 ± 0.005
170	831 ± 28	541	-0.099 ± 0.005
150	849 ± 27	562	-0.101 ± 0.008
120	1019 ± 21	587	-0.159 ± 0.007

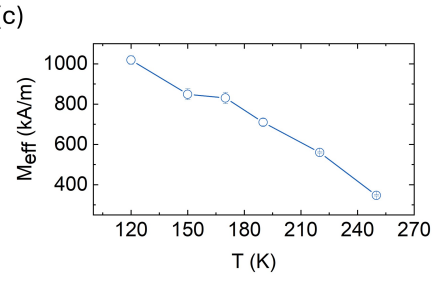

Figure 6.9: (a) Trend of the precessional frequency as a function of B_{ext} and for different temperatures. Solid lines are the best fit using Eq. 6.1. (b) Table reporting values of temperature, M_{eff}, M_s and K_{eff}. (c) Trend of M_{eff} as a function of T.

6.2.5 On the amplitude of the magnetization precession

In this measurement campaign, we observe a reduction in the precessional amplitude, eventually disappearing entirely at low temperatures and low magnetic fields. Here, we will provide an interpretation of this observation, drawing on insight from Ref. [181, 182, 188, 189].

The amplitude of the tr-MOKE signal can be expressed as [181, 182]

$$\theta_{\text{MOKE}} \propto \frac{\Delta M_z}{M_z} \propto \sin(\theta_{\text{M}} - \theta_H)\sin(\theta_{\text{M}}) \tag{6.5}$$

where θ_{H} represents the angle of the external field relative to the sample surface normal, and θ_{M} denotes the angle of the equilibrium effective field, or equivalently, the direction of the magnetization at equilibrium, as shown in Fig. 6.3.b. Thus, the amplitude of the precession approaches zero both when the magnetization aligns with the applied field ($\theta_M = \theta_H$), eliminating the torque induced by the laser pulse, and when the magnetization's equilibrium axis approaches the sample surface normal ($\theta_{\text{M}} \to 0$). In our experimental setup, the magnetic field is not aligned with the easy axis, and the first scenario is expected at "high" applied magnetic fields, where the external field is strong enough to overcome the sample's anisotropy field and align the sample magnetization, as experimentally observed in Ref. [183]. However, in our measurement campaign B_{ext} is too low to observe this phenomenology. The "low" value of B_{ext}, combined with the sample's primarily IP orientation ($\theta_{\text{H}} = 55°$) and the IP magnetic anisotropy, results in an expected IP magnetization. Moreover, as the temperature decreases, the effective anisotropy of IP K_{eff} increasingly favors IP magnetization, which means $\theta_{\text{M}} \to \pi/2$. Therefore, Eq. 6.5 predicts an increase in precessional amplitude at lower temperatures. However, Fig. 6.7 and 6.8 show an opposite trend. This can be explained by the increase in magnetic anisotropy at lower temperatures. As T decreases, the rise in K_{eff} leads to a stronger anisotropy field H_{a}. Consequently, the magnetization becomes more "pinned" by H_{a}, making it harder to initiate magnetization precession. The driving torque responsible for precession is reduced, resulting in a smaller precession cone and, consequently, a smaller amplitude in the tr-MOKE signal [188, 189]. This explains why no signal is observed at low temperatures in Fig. 6.8, and why a stronger B_{ext} is needed to induce magnetization precession at low temperatures.

This explains qualitatively the observed phenomenology. However, additional efforts are required to incorporate into Eq. 6.5 a term accounting for the anisotropy contribution to the dynamics - and consequently to the MOKE contrast - alongside the geometric terms. In addition to being useful for the quantitative interpretation of the data from this measurement campaign, it would also aid in predicting the magnetization dynamics in thinner samples or those with different anisotropy, such as F3GT.

6.3 Conclusions

We investigated the magnetization dynamics of an 8.8 nm Fe_5GeTe_2 thin film using tr-MOKE measurements. The study successfully revealed coherent magnetization dynamics, namely the Kittel mode. The magnetization dynamics exhibited a strong dependence on applied magnetic field and temperature, with the signal weakening at both high temperatures (near T_{c}) and low temperatures (where the IP anisotropy becomes stronger). The results are fully consistent with literature and theory, offering a clear understand-

ing of field-dependent and temperature-dependent behavior; however, more extensive datasets are needed to be able to extract more accurate values of K_{eff} and provide a quantitative description of the precessional amplitude as a function of θ_{M}, B_{ext} and K_{eff}.

Soon, the same approach will be applied to thinner FGT compounds, including samples down to a few monolayers (or even a single monolayer), as well as FGT-based heterostructures like F3GT/F5GT. The aim is to develop a comprehensive and systematic understanding of FGT magnetization dynamics and to explore interfacial effects and anisotropies that may emerge in the heterostructures, strengthening our understanding of the physics that is reflected in the magnetic behavior of these systems.

Conclusions

This thesis focuses on investigating coherent magnetic dynamics in various magnetic metallic thin films, both at zero and finite wavevectors, exploiting all-optical pump-probe spectroscopy.

In the polycrystalline Ni thin film samples, we investigated how acoustic waves generated in the substrate by a TG influence the magnetization dynamics of the overlayer ultrathin films . In particular, by tuning the intensity of the IP external magnetic field, we observed resonant magnetization precession. Analysis of the resonance field and linewidth allowed a comparison with photon-driven B-FMR measurements. The agreement between SAW-FMR and B-FMR confirms the validity of SAW-FMR as a local magnetometry technique, with spatial resolution determined by the probe's footprint on the sample. In these samples, the SAW-driven dynamics closely reflects uniform precession. However, the finite wavevector selectivity intrinsic in the TG excitation mechanism offers an additional degree of freedom for magnetization dynamics that turns out very valuiable to explore more complex material systems.

A preliminary measurement campaign on a ferrimagnetic $Co_{78}Gd_{22}$ alloy thin film, conducted at the NFFA-SPRINT lab ahead of the beamtime at FERMI-FEL, demonstrated that this approach can be successfully implemented in a table-top setup. The results, analyzed as a function of pump laser fluence, suggest local excitation of the system near the angular momentum compensation point, highlighting the potential of the TG non-homogeneous excitation mechanism. This finding indicates a promising future application of the TG technique for investigating locally confined phase transitions in solids, such as identifying relevant timescales and low-energy excitations (e.g., magnons, phonons, excitons) involved in the relaxation process leading to equilibrium. Additionally, the main outcomes from the beamtime access at the TIMER@FERMI beamline on Fe/Gd ferrimagnetic multilayers confirm TG spectroscopy as an effective method for probing magnons at wavevectors inaccessible to conventional inelastic techniques, yet highly relevant for spintronic applications.

Finally, laser-driven ferromagnetic resonance in a 9ML Fe_5GeTe_2 thin film was systematically investigated as a function of pump laser fluence, external magnetic field, and temperature. This measurement campaign complete the commissioning of the cryogenic system of the NFFA-SPRINT, and in fact demonstrated the possibility of addressing the gap in the literature regarding laser-driven dynamics in this class of 2D van der Waals ferromagnets. Although further experimental and theoretical work is necessary to fully

interpret the data, the results are sound and definitely justify point future efforts in investigating laser-driven coherent magnetization dynamics as a function of sample properties as thickness and Fe composition, or in heterostructures based on FGT compounds.

To conclude, addressing cutting-edge challenges in the physics of matter necessitates the development of specialized instruments and novel methods, as well as a deep understanding of prior work in the field using different approaches. It is crucial to determine which experimental results can be meaningfully compared to theoretical analyses and to recognize where these analyses fail when confronted with strong experimental evidence. Throughout this thesis, I have successfully integrated these key components, and I am pleased to have had the opportunity to engage with all critical aspects of research. This process has provided valuable experience in instrument design and construction, methodological reasoning, data analysis, phenomenology, and – although to a lesser extent – theoretical exploration.

Appendices

APPENDIX A

Supplementary material on the Ni samples

Details on Sample Growth

The films and capping layers for samples SiO_2(10nm)/Ni(40nm)/SiO_2 and SiO_2(10nm)/Ni(14nm)/CaF_2(001) are deposited using e-beam evaporation at the CNR-IOM FNF clean room facility in Trieste, Italy. After cleaning with acetone and ethanol, the substrates are placed in the deposition chamber, where a base pressure of 10^{-6} mbar is maintained. The thin films and capping layers were deposited using a Ni rod (99.995%, Alfa Aesar) and fused silica powder (99.995%, Alfa Aesar). The targets were placed inside a tungsten crucible and heated by a 10 keV electron beam. The deposition rates, r, for Ni and SiO_2 were measured before deposition using a calibrated quartz microbalance, resulting in $r_{\mathrm{Ni}} = 0.1$ Å/s and $r_{\mathrm{SiO_2}} = 0.3$ Å/s, respectively. An uncertainty of ± 2 nm in the deposited thickness is estimated considering the uncertainties of the calibration.

Structural quality: amorphous vs crystalline substrate

To prove the lower structural quality of the SiO_2(10nm)/Ni(40nm)/SiO_2 with respect to the SiO_2(10nm)/Ni(14nm)/CaF_2(001), we compare GIXRD and XRR measurements performed in collaboration with CNR-IMM and Università degli Studi di Milano-Bicocca on the same SiO_2(10nm)/Ni(14nm)/CaF_2(001) and on a SiO_2(10nm)/Ni(14nm)/SiO_2, grown with same protocol as the Ni(40nm)/SiO_2. Therefore, we can extend the same conclusions can be extended to the Ni(40nm)/SiO_2 sample. Therefore, we extend the conclusions drawn from the SiO_2(10nm)/Ni(14nm)/SiO_2 to SiO_2(10nm)/Ni(40nm)/SiO_2. In the following, we refer to SiO_2(10nm)/Ni(14nm)/CaF_2(001) as "Sample A", while to SiO_2(10nm)/Ni(14nm)/SiO_2 as "Sample B".

GIXRD measurements were performed using a Cu K_α X-ray source and a position-sensitive gas detector. For all measurements, the take-off angle between the X-ray beam and the sample was fixed at $\omega = 0.5°$. Fig. A.1.a displays the GIXRD patterns for sample A (black solid line) and sample B (red solid line) over a 2θ range of $90° - 110°$. By comparing the raw data to the standard diffraction patterns of Ni powder, the peaks near $93°$ and $103°$ were attributed to the (311) and (222) reflections, respectively. In powder diffraction analysis, it is common practice to estimate the crystallite size D using the Scherrer formula [190]:

$$D = \frac{K\lambda}{\beta \cos\theta}, \tag{A.1}$$

where K is the Scherrer constant, typically set to 0.94 for spherical crystallites with cubic symmetry, $\lambda = 1.542$ Å represents the X-ray wavelength, β is the FWHM of the peak expressed in radians, and θ is the peak position. For polycrystalline samples, applying

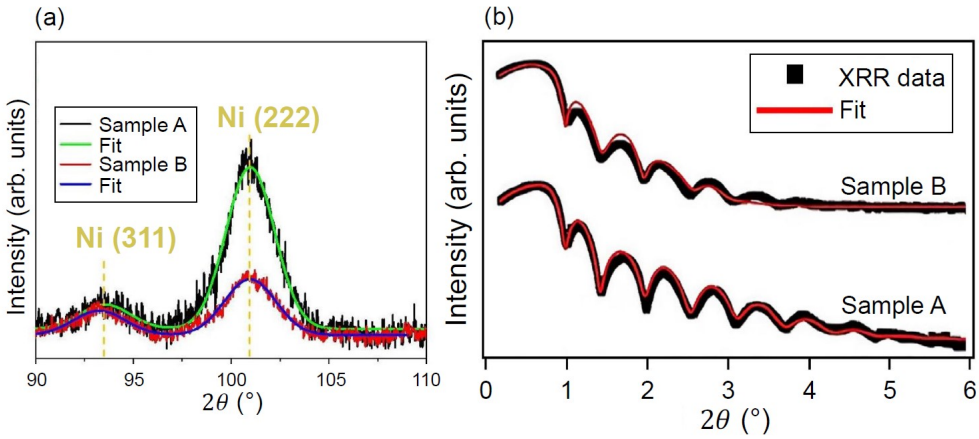

Figure A.1: GIXRD patterns for Sample A (black solid line) and Sample B (red solid line) are shown, along with cumulative Gaussian fits for the two diffraction peaks (green and blue solid lines, respectively). According to the powder diffraction database, these peaks correspond to the Ni (311) and Ni (222) reflections. (b) XRR data for both Sample A and Sample B are represented as black squares, with the corresponding fits displayed as red solid lines.

this method yielded a crystallite size of $D = (4.4 \pm 0.5)$ nm for both samples. It should be noted that, due to the horizontal orientation of the scattering plane in GIXRD geometry, D primarily reflects the IP crystallite size. There is no strong indication to suspect highly asymmetric grains, such as columnar structures elongated along the OOP axis, especially in cubic crystals like Ni. The increased intensity of the Ni (222) diffraction peak in Sample A is likely due to a distinct structural arrangement of the ferromagnetic film, showing more pronounced grain texturing compared to Sample B. This observation aligns with sample Sample A being grown on a crystalline substrate, while Sample B was deposited on an amorphous one. This indicates the chemical stability of the systems under investigation, as significant Ni oxidation would cause variations in electron density. The roughness of the Ni film is largely determined by the substrate used: for Sample B, which was deposited on an amorphous SiO_2 substrate, the roughness is more than three times that of Sample A, which was grown on a crystalline $CaF_2(001)$ substrate. These findings suggest that the Ni layer on the crystalline substrate is more structurally ordered, consistent with the GIXRD measurements.

Table A.1: Best-fit parameters to the XRR data for Sample A and B.

Sample A				**Sample B**			
Layer	t (nm)	r (nm)	ρ_e ($e^-/\text{Å}^3$)	Layer	t (nm)	r (nm)	ρ_e ($e^-/\text{Å}^3$)
SiO_2	8.5	1.2	0.67	SiO_2	9.6	1.3	0.67
Ni	14.4	0.4	2.30	Ni	14.4	1.3	2.38
CaF_2	Inf	0.7	0.95 (fixed)	SiO_2	Inf	0.9	0.67 (fixed)

The thickness t, surface roughness r, and electronic density ρ_e for each layer within the stack were determined using XRR measurements. The data were simulated using the Parratt formula [191], with corrections applied via a Croce-Névet factor [192]. In this model, the substrate was assumed to have infinite thickness and its electron density was set to the nominal value. Fig. A.1.b presents the XRR spectra for Samples A and B as black squares, with the red solid lines indicating the model fits to the experimental data. The best-fit parameters are detailed in Tab. A.1 The measured layer thicknesses agree with the expected nominal values, and the same applies to ρ_e, with the anticipated values being 0.67, 2.29, and 0.95 $e^-/\text{Å}^3$ for SiO_2, Ni, and CaF_2, respectively. The roughness of the Ni film varies significantly depending on the substrate used: for Sample B on an amorphous SiO_2 substrate, the roughness is over three times greater than for Sample A, which is on a crystalline $CaF_2(001)$ substrate. This indicates that the Ni layer is more morphologically ordered on the crystalline substrate, a conclusion that aligns with the GIXRD findings. These observations underscore the reliability of the studied systems from a chemical standpoint, as substantial Ni oxidation would lead to changes in electron density.

Static magnetic characterization

We performed longitudinal Magneto-Optical Kerr Effect (MOKE) measurements at the NFFA facility in connection with the APE-HE beamline of IOM at Elettra Synchrotron [83] to probe the in-plane magnetic anisotropy of the sample. We used a 658 nm CW low-power WorldStarTech TECBL-10GC laser source. The incident angle was set to be $45°$ with respect to the normal to the sample surface and the intensity on sample was set to ~ 8 mWcm^{-2}. Fig. A.2 shows the hysteresis loops for SiO_2(10nm)Ni(14nm)/CaF_2(001) [panel (a)] and the SiO_2(10nm)/Ni(40nm)/SiO_2 [panel (b)]. For the SiO_2(10nm)/Ni(14nm) /CaF_2(001), $0°$ corresponds to having the external field aligned with the [100] axis of the substrate; in the case of the SiO_2(10nm)/Ni(40nm)/SiO_2, $0°$ correspond to having the external field aligned along an edge of the sample.

SiO_2(10nm)/Ni(40nm)/SiO_2 shows a good IP anisotropy, as expected for a polycrystalline thin film; on the other hand, a small uniaxial anisotropy is observed for SiO_2(10nm) /Ni(14nm)/CaF_2(001). A possible explanation is reported in literature [193], where they report on the possibility for ferromagnetic thin films to exhibit a small uniaxial anisotropy when grown by sputtering or evaporation; in this case the origin could be the off-normal axis of the cone. In both cases, the coercive field and saturation field are very small, being less than 2 mT and 3 mT, respectively. Therefore, the samples are magnetically saturated in all measurements presented in Ch. 4.3.

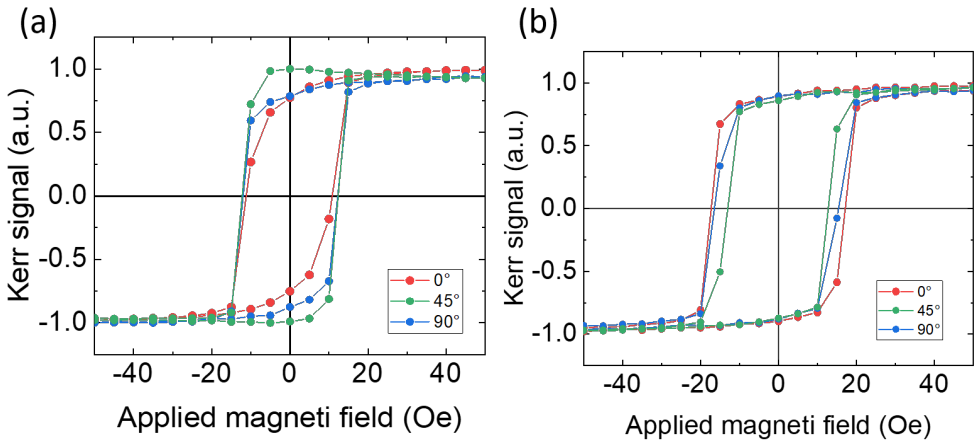

Figure A.2: Magnetic hysteresis loops acquired via longitudinal MOKE of (a) SiO_2(10nm)/Ni(14nm)/CaF_2(001) and (b) SiO_2(10nm)/Ni(40nm)/SiO_2.

A simple model for an efficient TG-pumped magnetoscoustic dynamics

The selection of substrates is informed by a straightforward model based on the analysis in Ref.[64], where the interaction between thermal and stress-strain gratings is considered within the context of TG spectroscopy. For isotropic or cubic systems, particularly when the TG wavevector q is oriented along a $\langle 100 \rangle$ crystallographic direction, the longitudinal strain component ϵ_{xx} in the direction of q (taken as the x axis) can be expressed as

$$\epsilon_{xx} = \beta_{\text{eff}} \Delta T, \tag{A.2}$$

where ΔT represents the temperature increase in the material, and

$$\beta_{\text{eff}} = \alpha_{\text{th}} \left(1 + 2\frac{C_{12}}{C_{11}} \right) \tag{A.3}$$

is the effective thermal expansion coefficient applicable in the context of plane-wave propagation. In this expression, α_{th} is the thermal expansion coefficient, and C_{ij} are the elastic stiffness constants (expressed using Voigt notation). The ratio C_{12}/C_{11} can be rewritten in terms of Poisson's ratio $\nu = \frac{C_{12}}{C_{11}+C_{12}}$. Therefore, Eq. A.3 simplifies to

$$\beta_{\text{eff}} = \alpha_{\text{th}} \frac{1+\nu}{1-\nu}. \tag{A.4}$$

Moreover, considering a sample volume V, the energy Q deposited as heat, and the specific heat capacity c_{th} at constant pressure, the resulting temperature increase can be described by

$$\Delta T = \frac{Q}{V c_{\text{th}}}. \tag{A.5}$$

Table A.2: Thermo-elastic efficiency η and figure of merit $\mathcal{F}$ as from Eq.3.6, both normalized to the CaF_2 value, together with relevant parameters for different substrates (mainly transparent). The substrates employed in the present experiment are highlighted in bold.

Substrate	α_{th} (10^{-6} K^{-1})	ν	c_{th} (J/kg·K)	k_{th} (W/m·K)	η_{norm}	$\mathcal{F}_{\text{norm}}$
CaF_2[a]	18.85	0.26	854	9.7	1	1
Al_2O_3[b]	5.8	0.21-0.33	753	41.9	0.31-0.41	0.07-0.09
$SrTiO_3$[c]	9.4[c]	0.24[d]	518[d]	12[c]	0.79	0.64
MgO[e]	9-12	0.35-0.37	880-1030	30-60	0.48-0.79	0.08-0.26
SiO_2[f]	0.54-0.57	0.15-0.16	700-750	1.0-1.5	0.03	0.17-0.29
Si[g]	7-8	0.27	668-715	84-100	0.45-0.55	0.04-0.06

[a] Ref.[194], [b] Ref.[195], [c] Ref.[196], [d] Ref.[197], [e] Ref.[198], [f] Ref.[199], [g] Ref.[200].

For comparative purposes across different substrates, a thermo-elastic efficiency η can be defined as follows:

$$\eta = \frac{\epsilon_{xx}}{Q/V} = \frac{\alpha_{\text{th}}}{c_{\text{th}}} \frac{1+\nu}{1-\nu}. \tag{A.6}$$

This efficiency η characterizes the extent of acoustic excitation generated for a given thermal stress density input. Beyond thermo-elastic efficiency, the magneto-optical contrast is influenced by the periodic temperature variations and their effect on magnetization. Consequently, higher thermal conductivity k_{th} is detrimental for the experiment, as it brings to faster thermalization.

A cumulative figure of merit $\mathcal{F}$ can be expressed using the following equation:

$$\mathcal{F} = \frac{\eta}{k_{\text{th}}} = \frac{\alpha_{\text{th}}}{k_{\text{th}} c_{\text{th}}} \frac{1+\nu}{1-\nu}. \tag{A.7}$$

Tab. A.2 presents the values for several commonly used substrates, with those utilized in this study highlighted in bold. From the extracted $\mathcal{F}$, results that the crystalline CaF_2 substrate has a high $\mathcal{F}$, while the amorphous SiO_2 is characterized by a lower $\mathcal{F}$ (approximately four times smaller). The accuracy of the model that leads to Eq. A.7 relies on the following three assumptions:

- The dominant stress component is longitudinal and aligned with q. This holds for TG spectroscopy on metallic systems and for the intensity grating scenario discussed here.
- The heat deposited Q is independent of the substrate material. In this experiment, this assumption is valid since the pump laser's radiant energy is primarily absorbed by the Ni overlayer, with minimal contribution from the transparent substrate and capping layer. Thus, the thermal input stress can be considered consistent across samples with the same Ni film thickness (though it will be smaller as the thickness of the film reduces).
- The volume of the substrate involved in expansion is assumed to be independent of the material under investigation. This assumption may not be entirely valid in the current scenario, as the volume engaged in SAW oscillation depends on the

specific acoustic mode and wavevector considered. Additionally, heat diffusion effects are not accounted for; for instance, the volume of the substrate involved in thermal expansion depends on thermal conductivity, thermal contact resistance, and time.

Comparing linewidths in SAW-FMR and B-FMR Measurements

The main hypotesis is that the signal is proportional to the magnetic susceptibility χ. In SAW-FMR, we acquire a time-domain signal and than we extract 2D maps of the FFT magnitude, and we extract the resonance linewidth ΔH_{magn} as described in Fig. 4.10. In the B-FMR measurements, the signal is proportional to the imaginary part of the χ; in this case the linewidth ΔH_{imag} can be directly extracted from the measurement. The question is: what is the relationship between ΔH_{magn} and ΔH_{imag}?
The starting point is Ref. [106], in particular equations (1.74) and (1.75) on page 20.
The resonance condition in this context is expressed in terms of the susceptibility tensor $\chi = \chi' - i\chi''$, where χ' and χ'' represent the real and imaginary parts of the susceptibility, respectively. The lineshape of both χ' and χ'' close to resonance is illustrated in Fig. A.3. For external fields close to the resonant condition, the real and imaginary parts of the susceptibility can be expressed as [106]:

$$\frac{\chi'}{\chi''_{\text{res}}} \approx \frac{\beta}{1+\beta^2}, \tag{A.8}$$

$$\frac{\chi''}{\chi''_{\text{res}}} \approx \frac{1}{1+\beta^2}, \tag{A.9}$$

where $\beta = \frac{H_0 - \omega/\gamma}{\alpha\omega/\gamma}$ for an experiment where the RF field is fixed and the static magnetic field is scanned. Here, $H_0 = \omega/\gamma$ is the resonance condition.

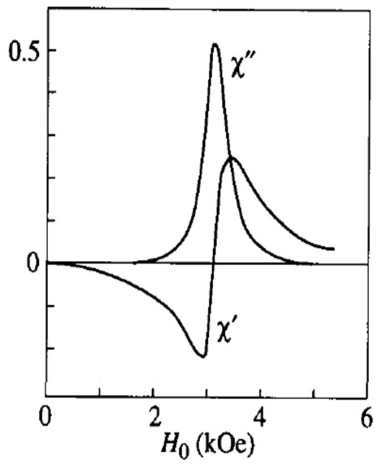

Figure A.3: General trend of real (χ') and imaginary (χ'') parts of the susceptibility in the proximity of resonance. Adapted from Ref. [106].

Assuming the magnitude of the FFT maps obtained from the time-domain signal is proportional to the magnitude of the complex susceptibility, it follows that:

$$|\chi| = \sqrt{(\chi')^2 + (\chi'')^2} = \chi''_{\text{res}} \sqrt{\frac{1}{1+\beta^2}}. \tag{A.10}$$

Thus, the lineshape of the magnitude of the complex susceptibility is similar to the imaginary component but is broader, as it is multiplied by the factor under the square root.

The magnetic field at which the magnitude peak is half of its maximum is given by:

$$\frac{|\chi|}{\chi''_{\text{res}}} = \sqrt{\frac{1}{1+\beta^2}} = \frac{1}{2}. \tag{A.11}$$

Simplifying:

$$\frac{1}{1+\beta^2} = \frac{1}{4} \quad \Rightarrow \quad \beta^2 = 3 \quad \Rightarrow \quad \beta = \pm\sqrt{3}. \tag{A.12}$$

Substituting $\beta = \frac{H-\omega/\gamma}{\alpha\omega/\gamma}$, the condition for the half-width at half-maximum (HWHM) is:

$$H = \frac{\omega}{\gamma} \pm \frac{\sqrt{3}\alpha\omega}{\gamma}. \tag{A.13}$$

The full width at half maximum (FWHM) of the FFT magnitude is then:

$$\Delta H_{\text{magn}} = 2\frac{\sqrt{3}\alpha\omega}{\gamma} = \sqrt{3}\Delta H_{\text{imag}}. \tag{A.14}$$

Therefore, the damping parameter α can be extracted using the relation:

$$\alpha = \frac{\Delta H_{\text{magn}}\gamma}{\sqrt{3}\,2\omega}. \tag{A.15}$$

It is evident that to compare the resonance linewidth extracted from SAW-FMR (ΔH_{magn}) and B-FMR (ΔH_{imag}), the results must be divided by the $\sqrt{3}$ factor. Thus, when extracting the α parameter in both cases, the same expression is used:

$$\alpha = \frac{\Delta H_{\text{eff}}\gamma}{2\omega}, \tag{A.16}$$

where $\Delta H_{\text{eff}} = \Delta H_{\text{imag}}$ in the case of B-FMR and $\Delta H_{\text{eff}} = \Delta H_{\text{magn}}/\sqrt{3}$ for SAW-FMR.

APPENDIX B

Supplementary material on the $Co_{78}Gd_{22}$ sample

Details on sample growth

The Pt(3nm)/$Co_{78}Gd_{22}$(15nm)/Pt(1.5nm)/Ta(1.5nm) thin film was grown on float glass by magnetron spattering using the following growth parameters: Ar pressure of $3 \cdot 10^{-3}$ mbar and sample rotation 20 rpm. Sputtering rates are 0.157, 0.172, 0.139 and 0.167 for Ta, Pt, Gd and Co, respectively.

Static magnetic characterization

Magnetic characterization of the sample was performed by polar MOKE measurements at the NFFA facility in connection with the APE-HE beamline of IOM at Elettra Synchrotron [83] to probe the expected OOP uniaxial magnetic anisotropy of the sample. We used a 658 nm continuous-wave low-power WorldStarTech TECBL-10GC laser source. The incident angle was set to 5° with respect to the normal to the sample surface; the incident laser power was set to ~ 8 mWcm^{-2}. Fig. B.1 shows the hysteresis loop at room temperature; integration time for each point was set at 10 ms for a loop total acquisition time of $\sim$ 20 s. As expected, the hysteresis loop is squared and presents a remanence close to the saturation magnetization indicating the OOP easy-axis magnetic anisotropy. The coercive field and saturation field are $\mu_0 H_c \simeq \mu_0 H_s \simeq 176$ mT.

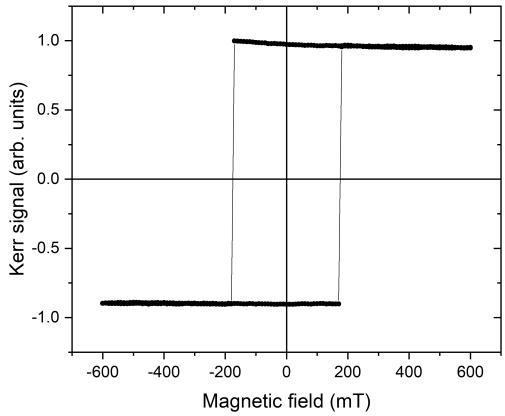

Figure B.1: Hysteresis loop obtained via static polar MOKE.

Equilibrium orientation of the magnetization in experimental geometry

To perform the energy minimization we used the following parameters:

- Exchange stiffness $A \sim 10$ pA/m as reported for a similar sample on [125]. The antiferromagnetic exchange interaction between Co and Gd is not taken into account since for the concentration of the case of study as it can be considered negligible for the concentration of this case of study [125].
- Saturation magnetization $M_s \sim 100$ emu/cm^3 = 10^5 A/m, as reported in [140] by the group who fabricated the sample
- Uniaxial anisotropy energy term $K_\mathrm{u} \sim 3 \cdot 10^4$ J/m^3 [140]
- External field $B_\mathrm{ext} = 260$ mT, oriented with an angle of 72° with respect to the sample normal

The results are showed in Fig. B.2. We found and OOP magnetization component of $m_z = 93288.0$ A/m and $m_x = 36018.6$ A/m, giving an equilibrium magnetization angle of $\theta_M \sim 21°$ with respect to the sample normal. The same calculation for $B_\mathrm{ext} = 180$ mT applied at the same $\theta_H = 72°$, gives $\theta_M \sim 15°$ ($m_z = 96551.7$ A/m and $m_x = 26033.8$ A/m).

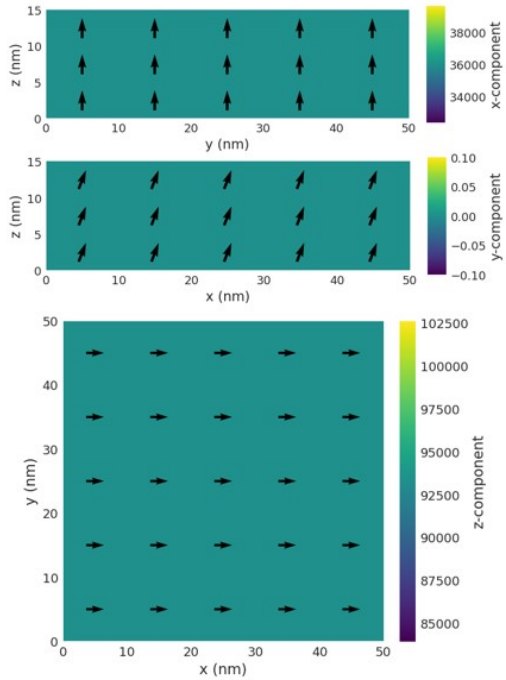

Figure B.2: Calculation of the static magnetization field in the experimental geometry when applied an external magnetic field of 260 mT. The plots show the the spin orientation to the different cross sections of the field and the magnetization values in A/m as colorscale.

Acoustic characterization of the sample

The acoustic signal is acquired in the *VVVV* configuration, i.e. by measuring the non-rotated component of the polarization of the diffracted beam. As discussed in Sec. 4.2, we expect to observe two active modes: the RSAW and the SSLW of the substrate. The measured intensity of the diffracted beam in the *VVVV* configuration is shown in Fig. B.3. We extracted the frequencies of the active modes by fitting the data with the equation 4.1, which in the case of two active modes can be written as

$$S_{VVVV}(t) = [a_0 e^{-t/\tau_0} + a_1 e^{-t/\tau_1} \sin(2\pi f_1 t + \phi_1) + a_2 e^{-t/\tau_2} \sin(2\pi f_2 t + \phi_2)]^2 + C, \quad \text{(B.1)}$$

where the first term describe the thermal decay, the second and the third one represent the damped oscillation associated to the RSAW and SSLW. From the best fit we obtain $f_1 = 1.15 \pm 0.06$ GHz and $f_2 = 2.22 \pm 0.03$ GHz, which correspond to sound velocities of 2.8 ± 0.15 and 5.5 ± 0.1 km/s, respectively. It is important to note that the magnetic dynamics occur on a faster timescale, indicating that the observed magnons are not elastically driven. Additionally, the isolation of the *H*-component of the diffracted probe beam is achieved efficiently.

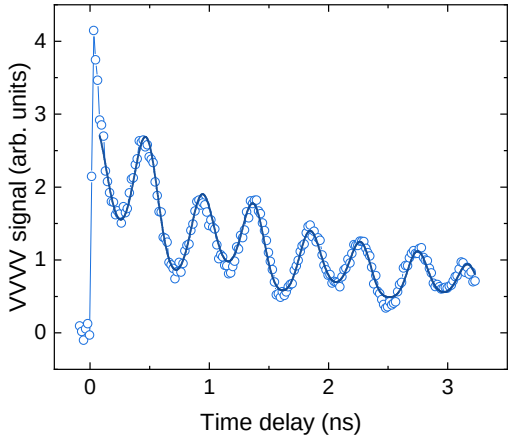

Figure B.3: Acoustic signal acquired in the VVVV experimental configuration. The solid line is the best fit using equation B.1.

APPENDIX C

Supplementary material on the Fe_5GeTe_2 sample

Details on sample growth

Al_2O_3(001) substrates with dimensions of 1×1 cm^2 were annealed in air at 900°C to get a smooth surface; the same procedure is then performed again at the same temperature in UHV. For the fabrication of Fe_5GeTe_2, high-purity Ge (99.999%) was evaporated at 1060°C, while high-purity Te (99.999%) was evaporated at 330°C and cracked at 1000°C. Fe (99.99%) was evaporated using standard e-beam techniques. The deposition rates of Fe and Te were calibrated by AFM on pre-patterned samples. The Ge deposition rate was calibrated through homoepitaxial Reflection High Energy Electron Diffraction (RHEED) oscillations on Ge(111). During the deposition, the Fe flux rate was monitored using a quartz microbalance, and the Ge and Te flux rates were checked before and after deposition using a UHV pressure gauge.

Static Magnetic characterization

Fig. C.1.a shows the temperature-dependent magnetic characterization of the samples performed by longitudinal MOKE measurements. Characterizations, ranging from 80 K up to 310 K, employed a s-polarized red laser (632.9 nm) and a photoelastic modulator (PEM) operating at 50 kHz coupled to a lock-in setup, with a laser spot diameter of about 500 µm. A phase retardation of 140° was used to deconvolute both the Kerr rotation and helicity, leading however to similar results. The curves shown have been corrected from linear slopes. The hysteresis loops show robust anisotropy IP, square loops, and small coercive field, relatable to a high structural quality of the film (few defects). Due to the hexagonal IP symmetry of the FGT lattices, no strong differences were observed for various direction of the applied magnetic field in the plane of the samples (not shown here). The coercive field H_c values are extracted from the hysteresis loops presented in Fig. C.1.b.

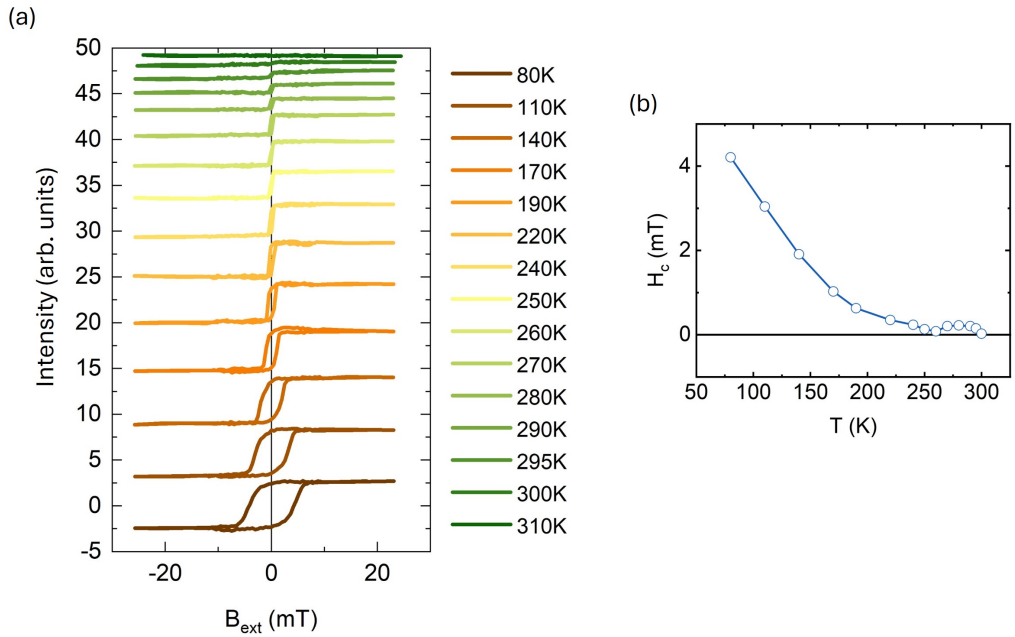

Figure C.1: (a) Hysteresis loops as a function of temperature. (b) Dependence of coercive field H_c on temperature.

Bibliography

1. Lloyd-Hughes, J., Oppeneer, P. M., Dos Santos, T. P., Schleife, A., Meng, S., Sentef, M. A., Ruggenthaler, M., Rubio, A., Radu, I., Murnane, M., *et al.* The 2021 ultrafast spectroscopic probes of condensed matter roadmap. *Journal of Physics: Condensed Matter* **33,** 353001 (2021).
2. J Stöhr, H. C. S. *Magnetism: From Fundamentals to Nanoscale Dynamics* 1st ed. (Springer-Verlag Berlin Heidelberg, 2006).
3. Coey, J. M. & Parkin, S. S. *Handbook of magnetism and magnetic materials* (Springer Cham, 2021).
4. Gilbert, T. L. A phenomenological theory of damping in ferromagnetic materials. *IEEE transactions on magnetics* **40,** 3443–3449 (2004).
5. Exl, L., Suess, D. & Schrefl, T. Micromagnetism. *Handbook of Magnetism and Magnetic Materials*, 1–44 (2020).
6. Stöhr, J. & Siegmann, H. C. Magnetism. *Solid-State Sciences. Springer, Berlin, Heidelberg* **5,** 236 (2006).
7. Yang, W.-G. & Schmidt, H. Acoustic control of magnetism toward energy-efficient applications. *Applied Physics Reviews* **8** (2021).
8. Kittel, C. Ferromagnetic resonance. *Journal de Physique et le Radium* **12,** 291–302 (1951).
9. Yalçın, O. *Ferromagnetic resonance: theory and applications* (BoD–Books on Demand, 2013).
10. Farle, M. Ferromagnetic resonance of ultrathin metallic layers. *Reports on Progress in Physics* **61,** 755 (1998).
11. Montiel, H. & Alvarez, G. in *Ferromagnetic Resonance-Theory and Applications* (Intech Rijeka, Croatia, 2013).
12. Celinski, Z., Urquhart, K. & Heinrich, B. Using ferromagnetic resonance to measure the magnetic moments of ultrathin films. *Journal of Magnetism and Magnetic Materials* **166,** 6–26 (1997).
13. Oogane, M., Wakitani, T., Yakata, S., Yilgin, R., Ando, Y., Sakuma, A. & Miyazaki, T. Magnetic damping in ferromagnetic thin films. *Japanese journal of applied physics* **45,** 3889 (2006).

14. Pu, Y., Odenthal, P., Adur, R., Beardsley, J., Swartz, A., Pelekhov, D., Kawakami, R., Pelz, J., Hammel, P. & Johnston-Halperin, E. Spin accumulation detection of FMR driven spin pumping in silicon-based metal-oxide-semiconductor heterostructures. *arXiv preprint arXiv:1311.0965* (2013).

15. Demidov, V., Urazhdin, S., Edwards, E. & Demokritov, S. Wide-range control of ferromagnetic resonance by spin Hall effect. *Applied Physics Letters* **99,** 172501 (2011).

16. Wang, Y., Ramaswamy, R. & Yang, H. FMR-related phenomena in spintronic devices. *Journal of Physics D: Applied Physics* **51,** 273002 (2018).

17. Van Kampen, M., Jozsa, C., Kohlhepp, J., LeClair, P., Lagae, L., De Jonge, W. & Koopmans, B. All-optical probe of coherent spin waves. *Physical Review Letters* **88,** 227201 (2002).

18. Dreher, L., Weiler, M., Pernpeintner, M., Huebl, H., Gross, R., Brandt, M. S. & Gönnenwein, S. T. Surface acoustic wave driven ferromagnetic resonance in nickel thin films: Theory and experiment. *Physical Review B* **86,** 134415 (2012).

19. Janušonis, J., Jansma, T., Chang, C., Liu, Q., Gatilova, A., Lomonosov, A., Shalagatskyi, V., Pezeril, T., Temnov, V. & Tobey, R. Transient grating spectroscopy in magnetic thin films: simultaneous detection of elastic and magnetic dynamics. *Scientific reports* **6,** 29143 (2016).

20. Carrara, P., Brioschi, M., Longo, E., Dagur, D., Polewczyk, V., Vinai, G., Mantovan, R., Fanciulli, M., Rossi, G., Panaccione, G., *et al.* All-Optical Generation and Time-Resolved Polarimetry of Magnetoacoustic Resonances via Transient Grating Spectroscopy. *Physical Review Applied* **18,** 044009 (2022).

21. Lenk, B., Ulrichs, H., Garbs, F. & Münzenberg, M. The building blocks of magnonics. *Physics Reports* **507,** 107–136 (2011).

22. Patton, C. E. Magnetic excitations in solids. *Physics Reports* **103,** 251–315 (1984).

23. Stancil, D. D. & Prabhakar, A. in *Spin Waves: Theory and Applications* 33–66 (Springer US, Boston, MA, 2009).

24. Bhattacharya, D., Bandyopadhyay, S. & Atulasimha, J. Voltage induced strain control of magnetization: computing and other applications. *Multifunctional Materials* **2,** 032001 (2019).

25. Lee, E. W. Magnetostriction and magnetomechanical effects. *Reports on progress in physics* **18,** 184 (1955).

26. Sander, D. Magnetostriction and magnetoelasticity. *Handbook of Magnetism and Magnetic Materials,* 1–45 (2020).

27. Sandlund, L., Fahlander, M., Cedell, T., Clark, A., Restorff, J. & Wun-Fogle, M. Magnetostriction, elastic moduli, and coupling factors of composite Terfenol-D. *Journal of Applied Physics* **75,** 5656–5658 (1994).

28. Klokholm, E. & Aboaf, J. The saturation magnetostriction of thin polycrystalline films of iron, cobalt, and nickel. *Journal of Applied Physics* **53,** 2661–2663 (1982).

29. Weiler, M., Dreher, L., Heeg, C., Huebl, H., Gross, R., Brandt, M. S. & Gönnenwein, S. T. Elastically driven ferromagnetic resonance in nickel thin films. *Physical review letters* **106,** 117601 (2011).

30. Gowtham, P. G., Moriyama, T., Ralph, D. C. & Buhrman, R. A. Traveling surface spin-wave resonance spectroscopy using surface acoustic waves. *Journal of Applied Physics* **118** (2015).

31. Rovillain, P., Duquesne, J.-Y., Christienne, L., Eddrief, M., Pini, M. G., Rettori, A., Tacchi, S. & Marangolo, M. Impact of Spin-Wave Dispersion on Surface-Acoustic-Wave Velocity. *Physical Review Applied* **18,** 064043 (2022).

32. Casals, B., Statuto, N., Foerster, M., Hernández-Mínguez, A., Cichelero, R., Manshausen, P., Mandziak, A., Aballe, L., Hernández, J. M. & Maciá, F. Generation and imaging of magnetoacoustic waves over millimeter distances. *Physical Review Letters* **124,** 137202 (2020).

33. Yang, W., Jaris, M., Hibbard-Lubow, D., Berk, C. & Schmidt, H. Magnetoelastic excitation of single nanomagnets for optical measurement of intrinsic Gilbert damping. *Physical Review B* **97,** 224410 (2018).

34. Rado, G. T. & Weertman, J. R. Spin-wave resonance in a ferromagnetic metal. *Journal of Physics and chemistry of solids* **11,** 315–333 (1959).

35. Weiler, M. *Mgnon-phonon interactions in ferromagnetic thin films* PhD thesis (Technischen Universität München, 2012).

36. Chang, C.-L. *Opto-magnonic Crystals: Optical Manipulation of Spin Waves* PhD thesis (University of Gröningen, 2019).

37. Bloch, P., Doe, N., Paige, E. & Yamaguchi, M. *Observations on surface skimming bulk waves and other waves launched from an IDT on lithium niobate* in *1981 Ultrasonics Symposium* (1981), 268–273.

38. Janušonis, J. *Magneto-elastic waves in thin ferromagnetic films* PhD thesis (University of Gröningen, 2017).

39. Zhang, J. & Averitt, R. D. Dynamics and control in complex transition metal oxides. *Annual Review of Materials Research* **44,** 19–43 (2014).

40. Zhang, X., Shao, J., Yan, C., Qin, R., Lu, Z., Geng, H., Xu, T. & Ju, L. A review on optoelectronic device applications of 2D transition metal carbides and nitrides. *Materials & Design* **200,** 109452 (2021).

41. Zak, J., Moog, E., Liu, C. & Bader, S. Magneto-optics of multilayers with arbitrary magnetization directions. *Physical Review B* **43,** 6423 (1991).

42. Qin, H., Holländer, R., Flajsman, L., Hermann, F., Dreyer, R., Woltersdorf, G. & Dijken, S. Nanoscale magnonic Fabry-Pérot resonator for low-loss spin-wave manipulation. *Nature Communications* **12,** 2293 (Apr. 2021).

43. Haider, T. A review of magneto-optic effects and its application. *International Journal of Electromagnetics and Applications* **7,** 17–24 (2017).

44. Hansteen, F., Kimel, A., Kirilyuk, A. & Rasing, T. Nonthermal ultrafast optical control of the magnetization in garnet films. *Physical Review B* **73,** 014421 (2006).

45. Kimel, A., Kirilyuk, A., Usachev, P., Pisarev, R., Balbashov, A. & Rasing, T. Ultrafast non-thermal control of magnetization by instantaneous photomagnetic pulses. *Nature* **435,** 655–657 (2005).

46. Hintermayr, J., Li, P., Rosenkamp, R., van Hees, Y. L., Igarashi, J., Mangin, S., Lavrijsen, R., Malinowski, G. & Koopmans, B. Ultrafast single-pulse all-optical switching in synthetic ferrimagnetic Tb/Co/Gd multilayers. *Applied Physics Letters* **123** (2023).
47. Fidler, A. P., Camp, S. J., Warrick, E. R., Bloch, E., Marroux, H. J., Neumark, D. M., Schafer, K. J., Gaarde, M. B. & Leone, S. R. Nonlinear XUV signal generation probed by transient grating spectroscopy with attosecond pulses. *Nature Communications* **10,** 1384 (2019).
48. Foglia, L., Wehinger, B., Perosa, G., Mincigrucci, R., Allaria, E., Armillotta, F., Brynes, A., Cucini, R., De Angelis, D., De Ninno, G., *et al.* Nanoscale transient polarization gratings. *arXiv preprint arXiv:2310.15734* (2023).
49. Ksenzov, D., Maznev, A. A., Unikandanunni, V., Bencivenga, F., Capotondi, F., Caretta, A., Foglia, L., Malvestuto, M., Masciovecchio, C., Mincigrucci, R., *et al.* Nanoscale transient magnetization gratings created and probed by femtosecond extreme ultraviolet pulses. *Nano Letters* **21,** 2905–2911 (2021).
50. Maznev, A., Bencivenga, F., Cannizzo, A., Capotondi, F., Cucini, R., Duncan, R., Feurer, T., Frazer, T., Foglia, L., Frey, H.-M., *et al.* Generation of coherent phonons by coherent extreme ultraviolet radiation in a transient grating experiment. *Applied Physics Letters* **113** (2018).
51. Wang, G., Liu, B., Balocchi, A., Renucci, P., Zhu, C., Amand, T., Fontaine, C. & Marie, X. Gate control of the electron spin-diffusion length in semiconductor quantum wells. *Nature Communications* **4,** 2372 (2013).
52. Wang, J., Guo, Y., Huang, Y., Luo, H., Zhou, X., Gu, C. & Liu, B. Diffusion dynamics of valley excitons by transient grating spectroscopy in monolayer WSe2. *Applied Physics Letters* **115,** 131902 (2019).
53. Miedaner, P. R., Berndt, N., Deschamps, J., Urazhdin, S., Khatu, N., Fainozzi, D., Brioschi, M., Carrara, P., Cucini, R., Rossi, G., *et al.* Excitation and detection of coherent nanoscale spin waves via extreme ultraviolet transient gratings. *Science Advances* **10,** eadp6015 (2024).
54. Rogers, J. A., Maznev, A. A., Banet, M. J. & Nelson, K. A. Optical generation and characterization of acoustic waves in thin films: Fundamentals and applications. *Annual Review of Materials Science* **30,** 117–157 (2000).
55. Cucini, R., Taschin, A., Bartolini, P. & Torre, R. Acoustic, thermal and flow processes in a water filled nanoporous glass by time-resolved optical spectroscopy. *Journal of the Mechanics and Physics of Solids* **58,** 1302–1317 (2010).
56. Suresh, S., Ramanand, A., Jayaraman, D. & Mani, P. Review on theoretical aspect of nonlinear optics. *Rev. Adv. Mater. Sci* **30,** 175–183 (2012).
57. Fox, M. *Optical Properties of Solids* (Oxford University Press, 2001).
58. Goodman, J. W. *Introduction to Fourier optics* (Roberts and Company Publishers, 2005).
59. New, G. *Frequency mixing* 19–44 (Cambridge University Press, 2011).
60. Bloembergen, N. Conservation laws in nonlinear optics. *Journal of the Optical Society of America* **70,** 1429–1436 (1980).

61. Thiel, C. Four-wave mixing and its applications. *Faculty of Washington, Washington DC* (2008).
62. Torre, R. *Time-resolved spectroscopy in complex liquids* (Springer, 2007).
63. Cucini, R. *Transport processes in nano-heterogeneous materials by Transient Grating experiments* PhD thesis (University of Firenze, 2008).
64. Eichler, H. J., Günter, P. & Pohl, D. W. *Laser-induced dynamic gratings* (Springer, 2013).
65. Bencivenga, F. & Masciovecchio, C. FEL-based transient grating spectroscopy to investigate nanoscale dynamics. *Nuclear Instruments and Methods in Physics Research Section A: Accelerators, Spectrometers, Detectors and Associated Equipment* **606,** 785–789 (2009).
66. Kuhn, H., Wagner, J., Han, S., Bernhardt, R., Gao, Y., Xiao, L., Zhu, J. & van Loosdrecht, P. H. Excitonic Transport and Intervalley Scattering in Exfoliated MoSe2 Monolayer Revealed by Four-Wave-Mixing Transient Grating Spectroscopy. *arXiv preprint arXiv:1911.08939* (2019).
67. Taschin, A. *Relaxation processes on supercooled liquids by heterodyne detected transient grating experiments* PhD thesis (Università degli Studi di Firenze, 2003).
68. Maznev, A., Mincigrucci, R., Bencivenga, F., Unikandanunni, V., Capotondi, F., Chen, G., Ding, Z., Duncan, R., Foglia, L., Izzo, M., *et al.* Generation and detection of 50 GHz surface acoustic waves by extreme ultraviolet pulses. *Applied Physics Letters* **119** (2021).
69. Bencivenga, F., Capotondi, F., Foglia, L., Mincigrucci, R. & Masciovecchio, C. Extreme ultraviolet transient gratings. *Advances in Physics: X* **8,** 2220363 (2023).
70. Käding, O., Skurk, H., Maznev, A. & Matthias, E. Transient thermal gratings at surfaces for thermal characterization of bulk materials and thin films. *Applied Physics A* **61,** 253–261 (1995).
71. Sander, M., Herzog, M., Pudell, J.-E., Bargheer, M., Weinkauf, N., Pedersen, M., Newby, G., Sellmann, J., Schwarzkopf, J., Besse, V., *et al.* Spatiotemporal coherent control of thermal excitations in solids. *Physical Review Letters* **119,** 075901 (2017).
72. Huberman, S., Duncan, R. A., Chen, K., Song, B., Chiloyan, V., Ding, Z., Maznev, A. A., Chen, G. & Nelson, K. A. Observation of second sound in graphite at temperatures above 100 K. *Science* **364,** 375–379 (2019).
73. Boechler, N., Eliason, J., Kumar, A., Maznev, A., Nelson, K. & Fang, N. Interaction of a contact resonance of microspheres with surface acoustic waves. *Physical Review Letters* **111,** 036103 (2013).
74. Cao, G., Jiang, S., Åkerman, J. & Weissenrieder, J. Femtosecond laser driven precessing magnetic gratings. *Nanoscale* **13,** 3746–3756 (2021).
75. Janušsonis, J. Magnetoelastic waves in thin ferromagnetic films (2017).
76. Brioschi, M., Carrara, P., Polewczyk, V., Dagur, D., Vinai, G., Parisse, P., Dal Zilio, S., Panaccione, G., Rossi, G. & Cucini, R. Multidetection scheme for transient-grating-based spectroscopy. *Optics Letters* **48,** 167–170 (2023).

77. Foglia, L., Mincigrucci, R., Maznev, A., Baldi, G., Capotondi, F., Caporaletti, F., Comin, R., De Angelis, D., Duncan, R., Fainozzi, D., *et al.* Extreme ultraviolet transient gratings: A tool for nanoscale photoacoustics. *Photoacoustics* **29,** 100453 (2023).

78. Bencivenga, F., Mincigrucci, R., Capotondi, F., Foglia, L., Naumenko, D., Maznev, A., Pedersoli, E., Simoncig, A., Caporaletti, F., Chiloyan, V., *et al.* Nanoscale transient gratings excited and probed by extreme ultraviolet femtosecond pulses. *Science advances* **5,** eaaw5805 (2019).

79. Ukleev, V., Leroy, L., Mincigrucci, R., Deangelis, D., Fainozzi, D., Khatu, N. N., Paltanin, E., Foglia, L., Bencivenga, F., Luo, C., *et al.* Transient grating spectroscopy on a DyCo5 thin film with femtosecond extreme ultraviolet pulses. *Structural Dynamics* **11** (2024).

80. Fainozzi, D., Cucini, R., Vila-Comamala, J., Lima, F., Ardana-Lamas, F., Bañares, L., Bargheer, M., Bencivenga, F., Berndt, N., Beye, M., *et al.* Protocols for X-ray transient grating pump/optical probe experiments at X-ray Free Electron Lasers. *Journal of Physics B: Atomic, Molecular and Optical Physics* (2024).

81. Kuroda, K., Satoh, T., Cho, S.-J., Iida, R. & Shimura, T. *Measurement of inverse Faraday effect in NiO using ultrashort laser pulses* in *Nonlinear Optics and Applications IV* **7728** (2010), 378–384.

82. Carrara, P., Brioschi, M., Silvani, R., Adeyeye, A., Panaccione, G., Gubbiotti, G., Rossi, G. & Cucini, R. Coherent and Dissipative Coupling in a Magnetomechanical System. *Physical Review Letters* **132,** 216701 (2024).

83. Vinai, G., Motti, F., Petrov, A. Y., Polewczyk, V., Bonanni, V., Edla, R., Gobaut, B., Fujii, J., Suran, F., Benedetti, D., Salvador, F., Fondacaro, A., Rossi, G., Panaccione, G., Davidson, B. A. & Torelli, P. An integrated ultra-high vacuum apparatus for growth and in situ characterization of complex materials. *Review of Scientific Instruments* **91,** 085109 (2020).

84. Cucini, R., Pincelli, T., Panaccione, G., Kopic, D., Frassetto, F., Miotti, P., Pierantozzi, G. M., Peli, S., Fondacaro, A., De Luisa, A., *et al.* Coherent narrowband light source for ultrafast photoelectron spectroscopy in the 17–31 eV photon energy range. *Structural Dynamics* **7** (2020).

85. *NFFA-Trieste project* `https://www.trieste.nffa.eu/`.

86. Maznev, A., Crimmins, T. & Nelson, K. How to make femtosecond pulses overlap. *Optics Letters* **23,** 1378–1380 (1998).

87. Hofmann, F., Short, M. P. & Dennett, C. A. Transient grating spectroscopy: An ultrarapid, nondestructive materials evaluation technique. *MRS Bulletin* **44,** 392–402 (2019).

88. Vega-Flick, A., Eliason, J., Maznev, A., Khanolkar, A., Abi Ghanem, M., Boechler, N., Alvarado-Gil, J. & Nelson, K. Laser-induced transient grating setup with continuously tunable period. *Review of Scientific Instruments* **86** (2015).

89. `https://www.iom.cnr.it/research-facilities/facilities-labs/synthesis-and-nano-fabrication/fnf/`.

90. Meshalkin, A. Y., Podlipnov, V., Ustinov, A. & Achimova, E. *Analysis of diffraction efficiency of phase gratings in dependence of duty cycle and depth* in *Journal of Physics: Conference Series* **1368** (2019), 022047.

91. Maznev, A., Nelson, K. & Rogers, J. Optical heterodyne detection of laser-induced gratings. *Optics letters* **23,** 1319–1321 (1998).
92. Hirohata, A., Yamada, K., Nakatani, Y., Prejbeanu, I.-L., Diény, B., Pirro, P. & Hillebrands, B. Review on spintronics: Principles and device applications. *Journal of Magnetism and Magnetic Materials* **509,** 166711 (2020).
93. Dieny, B., Prejbeanu, I. L., Garello, K., Gambardella, P., Freitas, P., Lehndorff, R., Raberg, W., Ebels, U., Demokritov, S. O., Akerman, J., *et al.* Opportunities and challenges for spintronics in the microelectronics industry. *Nature Electronics* **3,** 446–459 (2020).
94. Zakeri, K. Terahertz magnonics: Feasibility of using terahertz magnons for information processing. *Physica C: Superconductivity and its applications* **549,** 164–170 (2018).
95. Yoshii, S., Ohshima, R., Ando, Y., Shinjo, T. & Shiraishi, M. Detection of ferromagnetic resonance from 1 nm-thick Co. *Scientific Reports* **10,** 15764 (2020).
96. Farnell, G. W. & Adler, E. Elastic wave propagation in thin layers. *Physical Acoustics* **9,** 35–127 (2012).
97. Hassan, W. & Nagy, P. B. Simplified expressions for the displacements and stresses produced by the Rayleigh wave. *The Journal of the Acoustical Society of America* **104,** 3107–3110 (1998).
98. Lüth, H. *Surfaces and interfaces of solid materials* (Springer Science & Business Media, 2013).
99. Sathish, S., Martin, R. W. & Moran, T. J. Local surface skimming longitudinal wave velocity and residual stress mapping. *The Journal of the Acoustical Society of America* **115,** 165–171 (2004).
100. Caliendo, C. & Hamidullah, M. Guided acoustic wave sensors for liquid environments. *Journal of Physics D: Applied Physics* **52,** 153001 (2019).
101. Huang, Y., Das, P. K. & Bhethanabotla, V. R. Surface acoustic waves in biosensing applications. *Sensors and Actuators Reports,* 100041 (2021).
102. Fishman, I., Marshall, C., Meth, J. S. & Fayer, M. D. Surface selectivity in four-wave mixing: transient gratings as a theoretical and experimental example. *Journal of the Optical Society of America B* **8,** 1880–1888 (1991).
103. Fishman, I., Marshall, C., Tokmakoff, A. & Fayer, M. D. Transient grating diffraction from an interface between two materials: theory and experimental application. *Journal of the Optical Society of America B* **10,** 1006–1016 (1993).
104. Slayton, R. M., Nelson, K. A. & Maznev, A. Transient grating measurements of film thickness in multilayer metal films. *Journal of Applied Physics* **90,** 4392–4402 (2001).
105. Tokmakoff, A., Banholzer, W. & Fayer, M. Thermal diffusivity measurements of natural and isotopically enriched diamond by picosecond infrared transient grating experiments. *Applied Physics A* **56,** 87–90 (1993).
106. Gurevich, A. G. & Melkov, G. A. *Magnetization oscillations and waves* (CRC press, 2020).
107. Coey, J. M. *Magnetism and magnetic materials* (Cambridge University Press, 2010).

108. Chang, C., Lomonosov, A., Janusonis, J., Vlasov, V., Temnov, V. & Tobey, R. Parametric frequency mixing in a magnetoelastically driven linear ferromagnetic-resonance oscillator. *Physical Review B* **95,** 060409 (2017).

109. Longo, E., Belli, M., Alia, M., Rimoldi, M., Cecchini, R., Longo, M., Wiemer, C., Locatelli, L., Tsipas, P., Dimoulas, A., *et al.* Large Spin-to-Charge Conversion at Room Temperature in Extended Epitaxial Sb2Te3 Topological Insulator Chemically Grown on Silicon. *Advanced Functional Materials* **32,** 2109361 (2022).

110. Kittel, C. On the theory of ferromagnetic resonance absorption. *Physical Review* **73,** 155 (1948).

111. Azzawi, S., Hindmarch, A. & Atkinson, D. Magnetic damping phenomena in ferromagnetic thin-films and multilayers. *Journal of Physics D: Applied Physics* **50,** 473001 (2017).

112. Longo, E., Wiemer, C., Belli, M., Cecchini, R., Longo, M., Cantoni, M., Rinaldi, C., Overbeek, M. D., Winter, C. H., Gubbiotti, G., *et al.* Ferromagnetic resonance of Co thin films grown by atomic layer deposition on the Sb2Te3 topological insulator. *Journal of Magnetism and Magnetic Materials* **509,** 166885 (2020).

113. Bruno, P. & Renard, J. .-. Magnetic surface anisotropy of transition metal ultrathin films. *Applied Physics A* **49,** 499–506 (1989).

114. Wu, S., Smith, D. A., Nakarmi, P., Rai, A., Clavel, M., Hudait, M. K., Zhao, J., Michel, F. M., Mewes, C., Mewes, T., *et al.* Room-temperature intrinsic and extrinsic damping in polycrystalline Fe thin films. *Physical Review B* **105,** 174408 (2022).

115. Salikhov, R., Alekhin, A., Parpiiev, T., Pezeril, T., Makarov, D., Abrudan, R., Meckenstock, R., Radu, F., Farle, M., Zabel, H. & Temnov, V. V. Gilbert damping in NiFeGd compounds: Ferromagnetic resonance versus time-resolved spectroscopy. *Physical Review B* **99,** 104412 (10 2019).

116. Panda, S. N., Mondal, S., Majumder, S. & Barman, A. Ultrafast demagnetization and precession in permalloy films with varying thickness. *Physical Review B* **108,** 144421 (2023).

117. Mondal, S., Lin, Y., Polley, D., Su, C., Zettl, A., Salahuddin, S. & Bokor, J. Accelerated Ultrafast Magnetization Dynamics at Graphene/CoGd Interfaces. *ACS Nano* **16,** 9620–9630 (2022).

118. Godejohann, F., Scherbakov, A. V., Kukhtaruk, S. M., Poddubny, A. N., Yaremkevich, D. D., Wang, M., Nadzeyka, A., Yakovlev, D. R., Rushforth, A. W., Akimov, A. V., *et al.* Magnon polaron formed by selectively coupled coherent magnon and phonon modes of a surface patterned ferromagnet. *Physical Review B* **102,** 144438 (2020).

119. Hashimoto, Y., Daimon, S., Iguchi, R., Oikawa, Y., Shen, K., Sato, K., Bossini, D., Tabuchi, Y., Satoh, T., Hillebrands, B., *et al.* All-optical observation and reconstruction of spin wave dispersion. *Nature Communications* **8,** 15859 (2017).

120. Walowski, J., Kaufmann, M. D., Lenk, B., Hamann, C., McCord, J. & Münzenberg, M. Intrinsic and non-local Gilbert damping in polycrystalline nickel studied by Ti: sapphire laser fs spectroscopy. *Journal of Physics D: Applied Physics* **41,** 164016 (2008).

121. Mekonnen, A., Cormier, M., Kimel, A., Kirilyuk, A., Hrabec, A., Ranno, L. & Rasing, T. Femtosecond Laser Excitation of Spin Resonances in Amorphous Ferrimagnetic Gd 1- x Co x Alloys. *Physical Review Letters* **107,** 117202 (2011).

122. Ksenzov, D., Maznev, A. A., Unikandanunni, V., Bencivenga, F., Capotondi, F., Caretta, A., Foglia, L., Malvestuto, M., Masciovecchio, C., Mincigrucci, R., Nelson, K. A., Pancaldi, M., Pedersoli, E., Randolph, L., Rahmann, H., Urazhdin, S., Bonetti, S. & Gutt, C. Nanoscale Transient Magnetization Gratings Created and Probed by Femtosecond Extreme Ultraviolet Pulses. *Nano Letters* **21,** 2905–2911 (2021).

123. Sala, G. & Gambardella, P. Ferrimagnetic Dynamics Induced by Spin-Orbit Torques. *Advanced Materials Interfaces* **9,** 2201622 (2022).

124. Buschow, K. Intermetallic compounds of rare-earth and 3d transition metals. *Reports on Progress in Physics* **40,** 1179 (1977).

125. Suzuki, D. H., Lee, B. H. & Beach, G. S. Compositional dependence of spintronic properties in Pt/GdCo films. *Applied Physics Letters* **123** (2023).

126. Stanciu, C., Kimel, A., Hansteen, F., Tsukamoto, A., Itoh, A., Kirilyuk, A. & Rasing, T. Ultrafast spin dynamics across compensation points in ferrimagnetic GdFeCo: The role of angular momentum compensation. *Physical Review B—Condensed Matter and Materials Physics* **73,** 220402 (2006).

127. Hebler, B., Hassdenteufel, A., Reinhardt, P., Karl, H. & Albrecht, M. Ferrimagnetic Tb–Fe Alloy thin films: composition and thickness dependence of magnetic properties and all-optical switching. *Frontiers in Materials* **3,** 8 (2016).

128. Cochrane, R., Harris, R. & Zuckermann, M. The role of structure in the magnetic properties of amorphous alloys. *Physics Reports* **48,** 1–63 (1978).

129. Mizoguchi, T. & Cargill III, G. Magnetic anisotropy from dipolar interactions in amorphous ferrimagnetic alloys. *Journal of Applied Physics* **50,** 3570–3582 (1979).

130. Hansen, P., Clausen, C., Much, G., Rosenkranz, M. & Witter, K. Magnetic and magneto-optical properties of rare-earth transition-metal alloys containing Gd, Tb, Fe, Co. *Journal of Applied Physics* **66,** 756–767 (1989).

131. Binder, M., Weber, A., Mosendz, O., Woltersdorf, G., Izquierdo, M., Neudecker, I., Dahn, J., Hatchard, T., Thiele, J.-U., Back, C. H., *et al.* Magnetization dynamics of the ferrimagnet CoGd near the compensation of magnetization and angular momentum. *Physical Review B* **74,** 134404 (2006).

132. Landau, L. & Lifshitz, E. On the theory of the dispersion of magnetic permeability in ferromagnetic bodies. *Physikalische Zeitschrift der Sowjetunion* **8,** 101–114 (1935).

133. Wangsness, R. K. Sublattice Effects in Magnetic Resonance. *Phys. Rev.* **91,** 1085–1091 (1953).

134. Kaplan, J. & Kittel, C. Exchange frequency electron spin resonance in ferrites. *The Journal of Chemical Physics* **21,** 760–761 (1953).

135. Kim, S. K., Beach, G. S., Lee, K.-J., Ono, T., Rasing, T. & Yang, H. Ferrimagnetic spintronics. *Nature Materials* **21,** 24–34 (2022).

136. Kamra, A., Troncoso, R. E., Belzig, W. & Brataas, A. Gilbert damping phenomenology for two-sublattice magnets. *Physical Review B* **98,** 184402 (2018).

137. Kim, D.-H., Okuno, T., Kim, S. K., Oh, S.-H., Nishimura, T., Hirata, Y., Futakawa, Y., Yoshikawa, H., Tsukamoto, A., Tserkovnyak, Y., *et al.* Low magnetic damping of ferrimagnetic GdFeCo alloys. *Physical Review Letters* **122,** 127203 (2019).

138. Beg, M., Lang, M. & Fangohr, H. Ubermag: Towards more effective micromagnetic workflows. *IEEE Transactions on Magnetics* **58,** 1–5 (2022).

139. Sánchez-Tejerina, L., Ruiz, D. O., Martínez, E., Díaz, L. L. & Alejos, Ó. Spin Waves in Ferrimagnets near the Angular Magnetization Compensation Temperature: A Micromagnetic Study. *arXiv preprint arXiv:2401.08235* (2024).

140. Ceballos, A., Pattabi, A., El-Ghazaly, A., Ruta, S., Simon, C. P., Evans, R. F., Ostler, T., Chantrell, R. W., Kennedy, E., Scott, M., *et al.* Role of element-specific damping in ultrafast, helicity-independent, all-optical switching dynamics in amorphous (Gd, Tb) Co thin films. *Physical Review B* **103,** 024438 (2021).

141. Joo, S., Alemayehu, R. S., Choi, J.-G., Park, B.-G. & Choi, G.-M. Magnetic anisotropy and damping constant of ferrimagnetic GdCo alloy near compensation point. *Materials* **14,** 2604 (2021).

142. Haltz, E., Sampaio, J., Krishnia, S., Berges, L., Weil, R. & Mougin, A. Measurement of the tilt of a moving domain wall shows precession-free dynamics in compensated ferrimagnets. *Scientific Reports* **10,** 16292 (2020).

143. Malinowski, G., Kuiper, K., Lavrijsen, R., Swagten, H. & Koopmans, B. Magnetization dynamics and Gilbert damping in ultrathin Co48Fe32B20 films with out-of-plane anisotropy. *Applied Physics Letters* **94** (2009).

144. Djordjević Kaufmann, M. *Magnetization dynamics in all-optical pump-probe experiments: spin-wave modes and spin-current damping* PhD thesis (Georg-August-Universität Göttingen, 2007).

145. Starke, K., Heigl, F., Vollmer, A., Weiss, M., Reichardt, G. & Kaindl, G. X-ray magneto-optics in lanthanides. *Physical Review Letters* **86,** 3415 (2001).

146. Van Kranendonk, J. & Van Vleck, J. Spin waves. *Reviews of Modern Physics* **30,** 1 (1958).

147. Blank, T. G., Hermanussen, S., Lichtenberg, T., Rasing, T., Kirilyuk, A., Koopmans, B. & Kimel, A. V. Laser-Induced Transient Anisotropy and Large Amplitude Magnetization Dynamics in a Gd/FeCo Multilayer. *Advanced Materials Interfaces* **9,** 2201283 (2022).

148. Zhang, H., Chen, R., Zhai, K., Chen, X., Caretta, L., Huang, X., Chopdekar, R. V., Cao, J., Sun, J., Yao, J., *et al.* Itinerant ferromagnetism in van der Waals Fe 5- x Ge Te 2 crystals above room temperature. *Physical Review B* **102,** 064417 (2020).

149. May, A. F., Bridges, C. A. & McGuire, M. A. Physical properties and thermal stability of Fe 5- x GeTe 2 single crystals. *Physical Review Materials* **3,** 104401 (2019).

150. Fei, Z., Huang, B., Malinowski, P., Wang, W., Song, T., Sanchez, J., Yao, W., Xiao, D., Zhu, X., May, A. F., *et al.* Two-dimensional itinerant ferromagnetism in atomically thin Fe3GeTe2. *Nature Materials* **17,** 778–782 (2018).

151. Tan, C., Lee, J., Jung, S.-G., Park, T., Albarakati, S., Partridge, J., Field, M. R., McCulloch, D. G., Wang, L. & Lee, C. Hard magnetic properties in nanoflake van der Waals Fe3GeTe2. *Nature Communications* **9,** 1554 (2018).

152. Ershadrad, S., Ghosh, S., Wang, D., Kvashnin, Y. & Sanyal, B. Unusual magnetic features in two-dimensional Fe5GeTe2 induced by structural reconstructions. *The Journal of Physical Chemistry Letters* **13,** 4877–4883 (2022).

153. Tan, C., Xie, W.-Q., Zheng, G., Aloufi, N., Albarakati, S., Algarni, M., Li, J., Partridge, J., Culcer, D., Wang, X., *et al.* Gate-controlled magnetic phase transition in a van der Waals magnet Fe5GeTe2. *Nano Letters* **21,** 5599–5605 (2021).

154. Deng, Y., Yu, Y., Song, Y., Zhang, J., Wang, N. Z., Sun, Z., Yi, Y., Wu, Y. Z., Wu, S., Zhu, J., *et al.* Gate-tunable room-temperature ferromagnetism in two-dimensional Fe3GeTe2. *Nature* **563,** 94–99 (2018).

155. Tang, M., Huang, J., Qin, F., Zhai, K., Ideue, T., Li, Z., Meng, F., Nie, A., Wu, L., Bi, X., *et al.* Continuous manipulation of magnetic anisotropy in a van der Waals ferromagnet via electrical gating. *Nature Electronics* **6,** 28–36 (2023).

156. Hu, X., Zhao, Y., Shen, X., Krasheninnikov, A. V., Chen, Z. & Sun, L. Enhanced ferromagnetism and tunable magnetism in Fe3GeTe2 monolayer by strain engineering. *American Chemical Society Applied Materials & Interfaces* **12,** 26367–26373 (2020).

157. Chen, X., Schierle, E., He, Y., Vranas, M., Freeland, J. W., McChesney, J. L., Ramesh, R., Birgeneau, R. J. & Frano, A. Antiferromagnetic order in Co-doped Fe 5 GeTe 2 probed by resonant magnetic x-ray scattering. *Physical Review Materials* **6,** 094404 (2022).

158. Zhang, J., Wang, Z., Xing, Y., Luo, X., Wang, Z., Wang, G., Shen, A., Ye, H., Dong, S. & Li, L. Enhanced magnetic and electrical properties of Co-doped Fe5GeTe2. *Applied Physics Letters* **124** (2024).

159. Huang, X., Zhang, L., Tong, L., Li, Z., Peng, Z., Lin, R., Shi, W., Xue, K.-H., Dai, H., Cheng, H., *et al.* Manipulating exchange bias in 2D magnetic heterojunction for high-performance robust memory applications. *Nature Communications* **14,** 2190 (2023).

160. Zhao, B., Karpiak, B., Hoque, A. M., Dhagat, P. & Dash, S. P. Strong perpendicular anisotropic ferromagnet Fe3GeTe2/graphene van der Waals heterostructure. *Journal of Physics D: Applied Physics* **56,** 094001 (2023).

161. Lichtenberg, T., Schippers, C. F., van Kooten, S. C., Evers, S. G., Barcones, B., Guimarães, M. H. & Koopmans, B. Anisotropic laser-pulse-induced magnetization dynamics in van der Waals magnet Fe3GeTe2. *2D Materials* **10,** 015008 (2022).

162. Alahmed, L., Nepal, B., Macy, J., Zheng, W., Casas, B., Sapkota, A., Jones, N., Mazza, A. R., Brahlek, M., Jin, W., *et al.* Magnetism and spin dynamics in room-temperature van der Waals magnet Fe5GeTe2. *2D Materials* **8,** 045030 (2021).

163. Yuan, Y., Liu, D., Yu, J., Zhang, G., Chen, X., Liu, R., Wang, S., Pei, F., Wei, L., Li, Z., *et al.* Modulating above-room-temperature magnetism in Ga-implanted Fe5GeTe2 van der Waals magnets. *Applied Physics Letters Materials* **11** (2023).

164. Gibertini, M., Koperski, M., Morpurgo, A. F. & Novoselov, K. S. Magnetic 2D materials and heterostructures. *Nature Nanotechnology* **14,** 408–419 (2019).

165. Mermin, N. D. & Wagner, H. Absence of ferromagnetism or antiferromagnetism in one-or two-dimensional isotropic Heisenberg models. *Physical Review Letters* **17,** 1133 (1966).

166. Wang, Q. H., Bedoya-Pinto, A., Blei, M., Dismukes, A. H., Hamo, A., Jenkins, S., Koperski, M., Liu, Y., Sun, Q.-C., Telford, E. J., *et al.* The magnetic genome of two-dimensional van der Waals materials. *Nano Letters* **16,** 6960–7079 (2022).

167. Liu, P., Zhang, Y., Li, K., Li, Y. & Pu, Y. Recent advances in 2D van der Waals magnets: Detection, modulation, and applications. *iScience* **26,** 107584 (2023).

168. Huang, B., Clark, G., Navarro-Moratalla, E., Klein, D. R., Cheng, R., Seyler, K. L., Zhong, D., Schmidgall, E., McGuire, M. A., Cobden, D. H., *et al.* Layer-dependent ferromagnetism in a van der Waals crystal down to the monolayer limit. *Nature* **546,** 270–273 (2017).

169. Avsar, A., Tan, J. Y., Taychatanapat, T., Balakrishnan, J., Koon, G., Yeo, Y., Lahiri, J., Carvalho, A., Rodin, A. & O'Farrell, e. a. Spin–orbit proximity effect in graphene. *Nature Communications* **5,** 4875 (2014).

170. Hu, J., Luo, J., Zheng, Y., Chen, J., Omar, G. J., Wee, A. T. S. & Ariando, A. Magnetic proximity effect at the interface of two-dimensional materials and magnetic oxide insulators. *Journal of Alloys and Compounds* **911,** 164830 (2022).

171. Chaluvadi, S. K., Chalil, S. P., Jana, A., Dagur, D., Vinai, G., Motti, F., Fujii, J., Mezhoud, M., Lüders, U., Polewczyk, V., *et al.* Uncovering the Lowest Thickness Limit for Room-Temperature Ferromagnetism of Cr1. 6Te2. *Nano Letters* **24,** 7601–7608 (2024).

172. Och, M., Martin, M.-B., Dlubak, B., Seneor, P. & Mattevi, C. Synthesis of emerging 2D layered magnetic materials. *Nanoscale* **13,** 2157–2180 (2021).

173. Ribeiro, M., Gentile, G., Marty, A., Dosenovic, D., Okuno, H., Vergnaud, C., Jacquot, J.-F., Jalabert, D., Longo, D., Ohresser, P., *et al.* Large-scale epitaxy of two-dimensional van der Waals room-temperature ferromagnet Fe5GeTe2. *Nature Partner Journals 2D Materials and Applications* **6,** 10 (2022).

174. Roemer, R., Liu, C. & Zou, K. Robust ferromagnetism in wafer-scale monolayer and multilayer Fe3GeTe2. *Nature Partner Journals 2D Materials and Applications* **4,** 33 (2020).

175. Lupi, S., Tomarchio, L., Polewczyk, V., Mosesso, L., Marty, A., Macis, S., Jamet, M. & Bonell, F. Light-driven Electrodynamics and Demagnetization in FenGeTe2 (n= 3, 5) Thin Films. *Under Review* (2024).

176. Guo, J.-j., Xia, Q.-l., Wang, X.-g., Nie, Y.-z., Xiong, R. & Guo, G.-h. Temperature and thickness dependent magnetization reversal in 2D layered ferromagnetic material Fe3GeTe2. *Journal of Magnetism and Magnetic Materials* **527,** 167719 (2021).

177. Polyanskiy, M. N. Refractiveindex.info database of optical constants. *Scientific Data* **11,** 94 (2024).

178. Hatayama, S., Ando, D. & Sutou, Y. Relation between density and optical contrasts upon crystallization in Cr2Ge2Te6 phase-change material: coexistence of a positive optical contrast and a negative density contrast. *Journal of Physics D: Applied Physics* **52,** 325111 (2019).

179. Idzuchi, H., Llacsahuanga Allcca, A. E., Haglund, A. V., Pan, X.-C., Matsuda, T., Tanigaki, K., Mandrus, D. & Chen, Y. P. On the Optical Properties of Cr2Ge2Te6 and Its Heterostructure. *Condensed Matter* **8,** 59 (2023).

180. Mondal, S., Lin, Y., Polley, D., Su, C., Zettl, A., Salahuddin, S. & Bokor, J. Accelerated Ultrafast Magnetization Dynamics at Graphene/CoGd Interfaces. *Nano Letters* **16,** 9620–9630 (2022).

181. Lattery, D. M., Zhu, J., Zhang, D., Wang, J.-P., Crowell, P. A. & Wang, X. Quantitative analysis and optimization of magnetization precession initiated by ultrafast optical pulses. *Applied Physics Letters* **113** (2018).

182. Bonda, A., Uba, L., Załeski, K. & Uba, S. Ultrafast magnetization dynamics in an epitaxial Ni54.3Mn31.9Sn13.8 Heusler-alloy film close to the Curie temperature. *Physical Review B* **99,** 184424 (2019).

183. Capua, A., Yang, S.-h., Phung, T. & Parkin, S. S. Determination of intrinsic damping of perpendicularly magnetized ultrathin films from time-resolved precessional magnetization measurements. *Physical Review B* **92,** 224402 (2015).

184. Barati, E., Cinal, M., Edwards, D. & Umerski, A. Gilbert damping in magnetic layered systems. *Physical Review B* **90,** 014420 (2014).

185. Hauser, C., Richter, T., Homonnay, N., Eisenschmidt, C., Qaid, M., Deniz, H., Hesse, D., Sawicki, M., Ebbinghaus, S. G. & Schmidt, G. Yttrium iron garnet thin films with very low damping obtained by recrystallization of amorphous material. *Scientific Reports* **6,** 20827 (2016).

186. Wu, J., Cheng, T., Lu, C., Lu, X. & Bunce, C. *Spin-dynamic measurement techniques* (Springer, 2015).

187. Bera, A., Jana, N., Agarwal, A. & Mukhopadhyay, S. Anisotropic magnetization dynamics in Fe5GeTe2: Role of critical fluctuations. *arXiv preprint arXiv:2406.13273* (2024).

188. Ma, X., Fang, F., Li, Q., Zhu, J., Yang, Y., Wu, Y., Zhao, H. & Lüpke, G. Ultrafast spin exchange-coupling torque via photo-excited charge-transfer processes. *Nature Communications* **6,** 8800 (2015).

189. Kisielewski, J., Kirilyuk, A., Stupakiewicz, A., Maziewski, A., Kimel, A., Rasing, T., Baczewski, L. & Wawro, A. Laser-induced manipulation of magnetic anisotropy and magnetization precession in an ultrathin cobalt wedge. *Physical Review B - Condensed Matter and Materials Physics* **85,** 184429 (2012).

190. Patterson, A. The Scherrer formula for X-ray particle size determination. *Physical Review* **56,** 978 (1939).

191. Parratt, L. G. Surface studies of solids by total reflection of X-rays. *Physical Review* **95,** 359 (1954).

192. Nevot, 1. & Croce, P. Caractérisation des surfaces par réflexion rasante de rayons X. Application à l'étude du polissage de quelques verres silicates. *Revue de Physique appliquée* **15,** 761–779 (1980).

193. Park, Y., Fullerton, E. E. & Bader, S. Growth-induced uniaxial in-plane magnetic anisotropy for ultrathin Fe deposited on MgO (001) by oblique-incidence molecular beam epitaxy. *Applied Physics Letters* **66,** 2140–2142 (1995).

194. `https://www.opticalsolutions.it/en/defence-ir-components-en/caf2-en/calcium-fluoride-caf2/`.

195. `https://www.azom.com/article.aspx?ArticleID=52`.

196. https://www.azom.com/article.aspx?ArticleID=2362.

197. Samia, B. & Salima, S. First principles study of the structural, elastic and thermodynamic properties of the cubic perovskite-type SrTiO3. *Modelling, Measurement and Control B* **87,** 230–235 (2018).

198. https://www.azom.com/properties.aspx?ArticleID=54.

199. https://www.azom.com/properties.aspx?ArticleID=1387.

200. https://www.azom.com/properties.aspx?ArticleID=599.

List of abbreviations

2D	Two dimensional
3D	Three dimensional
AFM	Atomic Force Microscope
APE	Advanced Photoelectric Effect experiments
APE-HE	Advanced Photoelectric Effect experiments - High Energy
BBO	Beta Barium Borate
BVW	Backward Volume Wave
CMA	Compensated Magnetic Anisotropy
CNR	Consiglio Nazionale delle Ricerche
CVD	Chemical Vapor Deposition
CW	Continuous wave
dd	Dipole-Dipole
DE	Damon-Eshback
EA	Easy axis
EM	Electromagnetic
EUV	Extreme Ultra Violet
F3GT	Fe_3GeTe_2
F4GT	Fe_4GeTe_2
F5GT	Fe_5GeTe_2

FEL	Free Electron Laser
FFT	Fast Fourier Transform
FMR	Ferromagnetic Resonance
FWHM	Full Width Half Maximum
FWM	Four Wave Mixing
GIXRD	Grazing Incidence X-Ray Diffraction
HWHM	Half Width Half Maximum
IDT	Inter-Digitated Transducer
IFE	Inverse Faraday Effect
IMM	Istituto per la Microelettronica e Microsistemi
IOM	Istituto Officina dei Materiali
IP	In Plane
IR	Infrared
LCP	Left Circularly Polarized
LF	Local Field
LLG	Landau-Lifshitz-Gilbert
MBE	Molecular Beam Epitaxy
MCA	Magneto-crystalline Anisotropy
MEC	Magneto-Elastic Coupling
ML	Monolayer
MO	Magneto Optical
MOKE	Magneto Optical Kerr Effect
NFFA	Nanoscale Foundries and Fine Analysis
OOP	Out Of Plane
OPA	Optical Parametric Amplifier
PEM	Photoelastic Modulator
PMA	Perpendicular Magnetic Anisotropy
RCP	Right Circularly Polarized

RE	Rare Earth
rf	Radio-Frequency
RHEED	Reflection High Energy Electron Diffraction
RKKY	Ruderman-Kittel-Kasuya-Yosida
RSAW	Rayleigh Surface Acoustic Wave
SAW	Surface Acoustic Wave
SAW-FMR	Surface Acoustic Wave (driven) Ferromagnetic Resonance
SOC	Spin Orbit Coupling
SPRINT	Spin Polarization Research Instrument in the Nanoscale and Time domain
SSLW	Surface Skimming Longitudinal Wave
SW	Spin Wave
TEM	Transmission Electron Microscope
TG	Transient Grating
THG	Third Harmonic Generation
TM	Transition Metal
TMD	Transition Metal Dicalchogenide
tr	Time-Resolved
UHV	Ultra-High Vacuum
vdW	Van der Waals
XRR	X-Ray Reflectivity
YIG	Yttrium Iron Garnet

List of publications

Refereed publications

P. R. Miedaner†, N. Berndt†, J. Deschamps, S. Urazhdin, N. Khatu, D. Fainozzi, **M. Brioschi**, P. Carrara, R. Cucini, G. Rossi, S. Wittrock, D. Ksenzov, R. Mincigrucci, F. Bencivenga, L. Foglia, E. Paltanin, S. Bonetti, D. Engel, D. Schick, C. Gutt, R. Comin, K. A. Nelson and A. A. Maznev, *Excitation and detection of coherent nanoscale spin waves via extreme ultraviolet transient gratings*, Science Advances, 10(36), eadp6015 (2024).
DOI: 10.1126/sciadv.adp6015.
†These authors contributed equally.

D. Fainozzi, R. Cucini, J. Vila-Comamala, F. Lima, F. Ardana-Lamas, L. Bañares, M. Bargheer, F. Bencivenga, N. Berndt, M. Beye, M. Biednov, S. Bonetti, **M. Brioschi**, A. Cannizzo, P. Carrara, M. Chergui, C. David, R. Y. Engel, E. Ferrari, T. Feurer, P. Frankenberger, W. M. Gawelda, A. Gessini, S. Heder, X. Huang, N. N. Khatu, M. Knoll, A. Madsen, T. Mamyrbayev, C. Masciovecchio, A. A. Maznev, C. Milne, R. Mincigrucci, K. A. Nelson, E. Paltanin, G. Rossi, M. Scholz, C. Serrat, U. Staub, J. Szlachetko, R. Torre, M. R. Dhanalakshmi-Veeraraj, H. Xu, P. Zalden and C. Svetina, *Protocols for x-ray transient grating pump/optical probe experiments at x-ray free electron lasers*, Journal of Physics B: Atomic, Molecular and Optical Physics (2024)
DOI: 10.1088/1361-6455/ad717f.

P. Carrara,† **M. Brioschi**,† R. Silvani, A.O. Adeyeye, G. Panaccione, G. Gubbiotti, G. Rossi and R. Cucini, *Coherent and dissipative coupling in a magneto-mechanical system*, Physical Review Letters, 132, 216701 (2024).
DOI: 10.1103/PhysRevLett.132.216701.
†These authors contributed equally.

M. Brioschi, P. Carrara, V. Polewczyk, D. Dagur, G. Vinai, P. Parisse, S. Dal Zilio, G. Panaccione, G. Rossi and R. Cucini, *Multidetection scheme for transient-grating-based spectroscopy*, Optics Letters, 48, 167-170 (2023).
DOI: 10.1364/OL.476958.

D. Dagur, V. Polewczyk, A.Y. Petrov, P. Carrara, **M. Brioschi**, S. Fiori, R. Cucini, G. Rossi, G. Panaccione, P. Torelli and G. Vinai, *Visible light effects on photostrictive-magnetostrictive PMN-PT/Ni heterostructure*, Advanced Materials Interfaces, 9, 2201337 (2022).
DOI: 10.1002/admi.202201337.

P. Carrara, **M. Brioschi**, E. Longo, D. Dagur, V. Polewczyk, G. Vinai, R. Mantovan, M. Fanciulli, G. Rossi, G. Panaccione and R. Cucini, *All-optical generation and time-resolved polarimetry of magnetoacoustic resonances via transient grating spectroscopy*, Physical Review Applied, 18, 044009 (2022).
DOI: 10.1103/PhysRevApplied.18.044009.

Manuscripts in preparation

M. Brioschi et al, "Excitation of coherent magnons in the GHz range via Transient Grating Spectroscopy"

Acknowledgments

Questa tesi rappresenta solo *la punta dell'iceberg* di un percorso intenso e significativo, non solo sul piano lavorativo. Per questo, desidero ringraziare tutti coloro che vi hanno contribuito nei modi più disparati, rendendo questi tre anni un'esperienza di crescita tutt'altro che scontata.

In primo luogo, vorrei ringraziare Prof. Giorgio Rossi, supervisore di questo lavoro. Grazie per avermi permesso, in questi tre anni, di lavorare (in laboratorio e non) in piena fiducia e libertà, dimostrando sempre interesse ed entusiasmo per ogni tipo di questione, dalla discussione di nuovi risultati alle sfide tecniche da affrontare. Le sue osservazioni, sempre precise e puntuali, sono state un solido punto di riferimento e, allo stesso tempo, uno stimolo per nuove domande che spesso ci hanno portato a esplorare direzioni altrettanto nuove. Grazie per avermi continuamente incoraggiata a crescere come scienziata, supportandomi ed offrendomi molteplici opportunità per arricchire la mia cultura scientifica oltre la mia quotidiana attività di ricerca.

Un ringraziamento speciale va a Riccardo, che mi ha seguito giorno per giorno. Grazie per la tua grande competenza, immensa pazienza e sincera disponibilità. Il tuo supporto, tanto nelle questioni scientifiche quanto in quelle tecniche, è stato a dir poco fondamentale. Mi hai insegnato come muovermi in laboratorio (*schivando i fotoni*!), lasciandomi piena libertà di sperimentare e sbagliare. Non è affatto scontato, e superate le frustrazioni iniziali, mi rendo conto di come le conoscenze acquisite in questo modo rappresentino il bagaglio più prezioso che, alla fine, rimane. Grazie, inoltre, per avermi dimostrato l'importanza di costruire relazioni autentiche nel contesto delle collaborazioni, e per il tuo impegno quotidiano nel far sì che a SPRINT si respiri sempre un clima costruttivo.

Grazie infinite al nostro *ex-direttore* Giancarlo. Con la tua saggezza mista ad ironia hai reso ogni confronto, umano o scientifico, efficace e piacevole; la tua capacità di gestire tutti noi senza mai importi è a dir

poco ammirevole. Le *"confessioni"* nel tuo ufficio, che se anche non frequenti, sono state essenziali ogni volta che iniziavo a perdermi nei miei stessi pensieri e nelle mille misure, riportandomi in carreggiata con estrema pragmaticità.

Un immenso grazie a Pietro. Dal mio primo giorno a SPRINT mi hai supportata e sopportata durante le moltissime ore passate insieme nella *ghiacciaia*. Tutto il lavoro svolto insieme - dal montaggio iniziale del setup, alle prime misure, fino alla stesura dei primi articoli e agli intensi ragionamenti sulle potenzialità del TG - non sarebbe stato possibile senza la tua serietà, il tuo entusiasmo e la tua ammirevole determinazione. Grazie per aver reso divertenti perfino i viaggi della speranza, tra disagio, borselli e guide del touring.

Un sincero grazie ad Andrea, per la pazienza, la disponibilità e la professionalità tecnica con cui hai seguito il nostro lavoro, cercando sempre di migliorare il migliorabile. In particolare, grazie per il lavoro fatto (e che stai ancora portando avanti) sulla cameretta, senza cui lo studio sul FGT non sarebbe stato possibile.

Che dire poi degli altri *sprinters*! Avete reso il clima leggero e giocoso, pur essendo sempre pronti ad affrontare insieme questioni serie e complesse. Non è per nulla scontato ritrovarsi amici tra colleghi. Grazie a Gian Marco, capace di coinvolgere tutti con il suo entusiasmo, sia dentro che fuori il lavoro; ad Alice, amica ritrovata sempre pronta per uno Spritz; a Michele, fonte di ispirazione per l'impegno e la passione che dimostri, non solo in ambito lavorativo; ad Ale, pozzo di conoscenza ed articoli truculenti, che anche da Berlino riesci a strappare una risata con la tua simpatia mai scontata; to Savita, for your positive presence in the group; a Sara, fonte di ispirazione all'inizio del mio percorso. Grazie anche ai ramanisti: ad Andrea con la sua conoscenza infinita dell'ottica ed suoi aneddoti arabici, a Claudia e Mattia per aver portato lo spirito romano nelle loro brevi visite triestine.

A big and loud thank you also to the APE-HE group, that was extremely supportive and essential, not only for the work presented in this thesis. A heartfelt thank you to Vincent for the countless samples you fabricated for us, your availability, and your consistently positive and encouraging attitude. Your support has been truly essential for both the Ni and FGT studies. Most importantly, thank you for becoming a friend along the way! Thanks to Giovanni and Deepak, for the MOKE measurements and their restless support.

Un sincero grazie ai vicini T-Rex: Manuel, Wibke, Denny, Francesco e Federico, con cui ho condiviso in questi anni la vita di laboratorio e il disagio della 51.

Grazie a tutti i collaboratori, senza i quali nulla sarebbe stato possibile. Grazie a Rudi Sergo per la prontezza, competenza e simpatia nella risoluzione di problemi elettronici. Grazie a Simone Dal Zilio, Pietro Parisse, Emanuele Longo, Roberto Mantovan e Marco Fanciulli per il prezioso supporto fornito nel lavoro sul Ni. A sincere thank you to Alexei A. Maznev for the opportunity to be part of such an exciting collaboration, showcasing the cutting-edge applications of the TG technique; many thanks to Peter, Jude, Nadia, and Nupur - working alongside you has been an absolute pleasure. Grazie a tutto lo staff di TIMER: Riccardo, Laura, Filippo, Ettore e Danny. Grazie a Stefano Bonetti per le utili discussioni e gli incoraggiamenti per finalizzare il lavoro sul CoGd.

Grazie a tutte le persone con cui ho avuto il piacere di collaborare su progetti non presentati o non strettamente legati a questa tesi. Grazie a Prof. Adekunle Adeyeye, Gianluca Gubbiotti e Raffele Silvani per il lavoro svolto sui nanowires. Grazie Cristian Svetina per avermi introdotto al mondo dei FEL e coinvolto nel LTP, e a tutte le persone che vi hanno contribuito. Grazie a Floriana Morabito, Regina Ciancio e Pasquale Orgiani per il lavoro svolto insieme nel contesto di IMPRESS.

A big thank you to all the PhD students and Postdocs from around the world whom I had the pleasure of meeting at schools and conferences, especially to the ones who became good friends. Cheers to future adventures together!

Un grande grazie a tutti coloro che hanno contribuito rendere Trieste casa. A partire da tutti i matti con cui ho vissuto in FS 102, con cui ho condiviso le gioie i dolori della quotidiana convivenza. In particolare grazie a Marta, Nicola e Leonardo, per esserci stati sempre, con una parola di conforto, delle risate sguaiate, un caffè (o tiramisù) al momento giusto. Un grazie speciale soprattutto a tutti coloro che mi hanno ricordato quanto sia importante vivere anche al di fuori del lavoro: su un campo da frisbee, con bagnetti a Barcola, poesie e spettacoli teatrali, pazze serate, due chiacchiere davanti a uno Spritz o con instancabili fusa.

Grazie ai miei amici (non più così) milanesi, compagni di avventure dai tempi del liceo. È sempre un piacere perdersi e ritrovarsi (talvolta a matrimoni!), cresciuti ma essenzialmente gli stessi.

Mala ji kaame far kathin watat hoti, ti Sam mazhya pathishi ubha rahilyamule agadi sopi zali. Ya sathi tyache manapasoon abhaar! Sam, mazhya pratyek kathin prasangi too mala dilele protchhahan ani mazhya chhotya chhotya yashanche suddha bharbharoon kelele kautuk yabaddal mannapoorvak dhanyawaad! Aapale bhavi sahajeevan romanchak asel asa mala vishwas vatato.

Infine, il mio ultimo ringraziamento va alla mia famiglia. A nonna Car-

lina, che ti preoccupavi ogni volta che partivo e ti assicuravi che ad ogni mio ritorno si festeggiasse con pasticcini; a nonno Zino, per la grande stima che dimostri nei miei confronti; agli zii Paola, Mau e Ale, e ai cuginetti Ire, Dani e Fra, per rendere sempre piacevoli i miei ritorni; ad Aaronite, per le coccole scodinzolanti e le numerose sedute di *pet therapy*; ad Elena, sempre presente nonostante la distanza; e ai miei genitori, che da sempre mi sostenete e incoraggiate, accogliendo con sincera curiosità ogni mia scelta di vita.